

Dissertation
submitted to the
Combined Faculties of the Natural Sciences and Mathematics
of the Ruperto-Carola-University of Heidelberg, Germany
for the degree of
Doctor of Natural Sciences

put forward by
Martin Völkl
born in: Filderstadt, Germany
Oral examination: 2016-10-28

Electrons from beauty-hadron decays in central
Pb–Pb collisions at $\sqrt{s_{\text{NN}}} = 2.76 \text{ TeV}$

Referees:

Prof. Dr. Johanna Stachel

Prof. Dr. Ulrich Uwer

Abstract Heavy quarks (charm and beauty) are an important probe for the characterization of the quark-gluon plasma (QGP), a state of color deconfined, hadronic matter. Experimentally, the QGP is produced in ultrarelativistic heavy-ion collisions, where heavy quarks are automatically generated and interact with the produced medium. Within this work, the properties of the beauty quarks in the medium are measured via the semileptonic decays of the associated hadrons. The measurement is based on the particle identification and tracking capabilities of the ALICE detector at the LHC. The separation of electrons from beauty-hadron decays from the abundant background electrons is achieved using fits of the impact parameter distribution based on templates from Monte Carlo simulations. This approach makes use of the comparatively large decay length of the beauty hadrons ($c\tau \approx 500 \mu\text{m}$). The large particle multiplicities in central Pb–Pb collisions at $\sqrt{s_{\text{NN}}} = 2.76 \text{ TeV}$ create a particularly challenging environment for the measurement. The determined nuclear modification factor hints at values above unity for low transverse momenta of the electrons. In this region, the beauty quarks may participate in the collective motion of the medium. The nuclear modification factor decreases towards larger p_{T} , where an energy loss of the partons in the medium is expected. The measured range of $1.3 < p_{\text{T}} < 8 \text{ GeV}/c$ also represents a region where contributions from both radiative and collisional interactions with the medium can contribute and is thus particularly interesting for the understanding of the interaction of heavy quarks with the medium.

Deutsche Zusammenfassung Schwere Quarks (Charm und Beauty) sind eine wichtige Sonde um die Eigenschaften des Quark-Gluon Plasmas (QGP), ein Zustand von 'Deconfinement' der Materie, zu charakterisieren. Experimentell wird das QGP in ultrarelativistischen Schwerionenkollisionen erzeugt, wo schwere Quarks automatisch entstehen und mit dem erzeugten Medium interagieren. In dieser Arbeit werden die Eigenschaften von Beautyquarks im Medium über die semileptonischen Zerfälle der zugehörigen Hadronen gemessen. Die Messmethode basiert auf den Spurrekonstruktions- und Teilchenidentifikationsfähigkeiten des ALICE-Detektors am LHC. Die Unterscheidung von Elektronen aus Zerfällen von Beautyhadronen von den Untergrundelektronen wird durch einen Fit auf der Basis von Stoßparameterverteilungen aus Monte Carlo-Simulationen erreicht. Diese Herangehensweise nutzt die relativ hohe Zerfallslänge der Beautyhadronen ($c\tau \approx 500 \mu\text{m}$) aus. Die hohen Teilchenzahlmultiplizitäten der zentralen Pb–Pb-Kollisionen bei $\sqrt{s_{\text{NN}}} = 2.76 \text{ TeV}$ machen die Messung zu einer Herausforderung. Der ermittelte nukleare Modifikationsfaktor deutet auf Werte oberhalb von eins bei niedrigem Transversalimpuls der Elektronen hin. In diesem Bereich könnten die Beautyquarks an der Bewegung des Mediums teilhaben. Bei höherem p_{T} , wo ein Energieverlust der Quarks an das Medium erwartet wird, sinkt der nukleare Modifikationsfaktor. Das Messintervall von $1.3 < p_{\text{T}} < 8 \text{ GeV}/c$ entspricht einem Bereich in dem sowohl radiative als auch Stoßprozesse relevant sind und ist daher besonders interessant um die Wechselwirkung schwerer Quarks mit dem Medium zu verstehen.

Contents

1	Introduction	1
2	Heavy-ion collisions and the quark–gluon plasma	3
2.1	Quantum chromodynamics	3
2.1.1	Introduction	3
2.1.2	The QCD phase diagram	5
2.1.3	Lattice QCD	5
2.1.4	Gauge/string duality	8
2.2	Heavy-ion collisions	8
2.2.1	Initial State	9
2.2.2	Equilibration	11
2.2.3	Flow	12
2.2.4	Hadronization	16
3	Heavy Quarks in heavy-ion collisions	19
3.1	Initial hard scatterings	20
3.2	Heavy flavors during equilibration	22
3.3	Interaction with the thermalized medium	22
3.3.1	Heavy-quark energy loss in AdS/CFT	23
3.3.2	Heavy-quark energy loss in pQCD calculations	24
3.4	Hadronization	26
3.5	Theoretical models	27
3.6	Measurements	28
4	ALICE	31
4.1	The V0 detectors	32
4.2	Inner Tracking System	33
4.3	TPC	34

CONTENTS

4.4	TRD	35
4.5	TOF	36
4.6	Data set and detector simulations	36
5	Analysis strategy	39
6	Track selection and particle identification	45
6.1	Introduction	45
6.2	Estimation of the efficiencies and associated uncertainties	47
6.2.1	ITS selection criteria	50
6.2.2	TPC quality requirements	51
6.2.3	TOF selection criteria	54
6.2.4	TPC PID selection	55
6.3	Hadron contamination	62
7	Signal Extraction	65
7.1	Electron sources	65
7.2	Fit method	71
7.2.1	Maximum likelihood estimation	73
7.2.2	Bins without counts from Monte Carlo simulations	76
7.2.3	Uncertainty estimation and bias correction	78
7.3	Monte Carlo description and associated uncertainties	82
7.3.1	Impact parameter resolution	82
7.3.2	Mismatched conversion electrons	87
7.3.3	Strangeness	90
7.3.4	Hadron contamination	92
7.3.5	Momentum distribution of the heavy-flavor hadrons	94
7.3.6	Baryon ratio	100
7.4	Averaging procedure for the fluctuations of the resolution correction	101
8	Unfolding	105
8.1	Solution for an idealized problem	106
8.2	Application to the analysis	111
9	Results	115
9.1	The pp reference	115
9.2	The nuclear modification factor	118
9.3	Comparison to a blast wave model	121

9.4 Comparison to the charm case	123
10 Summary and Outlook	125
A Abbreviations and terms	129
B Calculations	133
B.1 A simple model for the effect of the truncated mean	133
B.2 Geometrical factor for electrons from photon conversions	135
B.3 Radial dependence of the mean impact parameter for electrons from photon conversions	136
B.4 The Mahalanobis distance	137
C Additional material	139
C.1 Detailed description of the fit algorithm	139
C.2 Additional figures	140

CONTENTS

Chapter 1

Introduction

The measurements of ultrarelativistic heavy-ion collisions opened the door to the study of a new state of hadronic matter. Experiments at the CERN Super Proton Synchrotron (SPS) [1, 2] and later at the Relativistic Heavy Ion Collider (RHIC) and the Large Hadron Collider (LHC) give access to a state of deconfined quarks and gluons, the Quark-Gluon Plasma (QGP). The analysis of the QGP gives an insight into the emergent properties of the strong interaction. The complexity of the non-abelian QCD but also of the heavy-ion collisions themselves shows the importance of using a variety of measurements to understand the properties of the produced matter.

An important probe for this characterization are heavy-flavors, meaning charm and beauty quarks, which can give an insight into the transport properties of the medium [3, 4]. The main focus of this work is the measurement of beauty quarks via the decays of their associated hadrons to a final state containing electrons.

Chapter 2 of this thesis aims to give a general understanding of the experimental access to the properties of the quark-gluon plasma, while the connection to approaches based on heavy-flavor measurements is discussed in more depth in chapter 3. The analysis discussed in this work is based on measurements by the ALICE experiment. The particularities of the subsystems that are particularly relevant to it are described in chapter 4.

A short overview of the general principles of the analysis is given in chapter 5. In comparison to earlier analyses with ALICE in pp collisions [5, 6], the approach described in this work is based on the use of the full information contained within the distribution of the transverse impact parameter of electrons. As will be shown, the high-multiplicity environment of the central (head-on) Pb–Pb collisions requires accurate methods for the estimation of the uncertainties associated with the measurements, which take into account the peculiarities of the measurements at high multiplicities. For this reason,

the description of the analysis is split into three parts. These are arranged by logical connection rather than by the sequence they are applied in in the analysis. For this reason, the electron candidate selection in chapter 6 is discussed together with the efficiency that results from this choice and with the uncertainty of this estimation.

Accordingly, chapter 7 is concerned both with the signal extraction method as well as with the associated uncertainties. This includes both the bias of the maximum likelihood estimator as well as the uncertainty in the accuracy of the impact parameter distribution templates which come from simulations of the detector and event properties. These estimates are central to the applicability of the method. Wherever possible, the uncertainties are estimated using data-driven methods and the known biases are corrected to the extent in which they are known.

The finite resolution of the measurement of the transverse momentum influences the measured distribution. The correction of this effect leads to a different mathematical structure than the correction for biases or efficiencies and it is thus treated separately. Chapter 8 aims to describe the mathematical formulation of this correction and to explain the choice of the particular correction algorithm.

The result of the analysis described in these chapters is the first measurement of beauty-hadron decay electrons at low transverse momentum in Pb–Pb collisions with ALICE. To interpret the result, it is useful to compare it with the corresponding measurement in pp collisions. This will be the subject of chapter 9. The resulting nuclear modification factor is then compared to theoretical predictions, to the corresponding p–Pb result and to a simple phenomenological model to understand the information contained within it.

Finally, the advantages of this analysis method suggest its application to different measurements as well, in particular to gain further insights in the interpretation of the results. Additionally, the formalism of the approach allows for a generalization when additional knowledge is available. The directions for such further developments are discussed in chapter 10.

The approach to the extraction of information from the available data is based on the idea of Bayesian inference [7, 8]. While the fundamental idea of the signal extraction is a maximum likelihood approach, this point-of-view allows for the clearest understanding of the meaning of the systematic uncertainties inherent in the measurement [9].

In order to make this thesis more concise, frequent terms are often abbreviated. In these cases as well as for acronyms, the first appearance will be written in bold script. An overview of all terms with short explanations can be found in appendix A for convenience.

Chapter 2

Heavy-ion collisions and the quark–gluon plasma

2.1 Quantum chromodynamics

2.1.1 Introduction

The gauge field theory of the strong interaction is called quantum chromodynamics (QCD). It describes the interaction of quarks and gluons. It is a non-abelian gauge theory with a Lagrangian that is invariant under local $SU(3)$ symmetry transformations [10]. The $N^2 - 1 = 8$ generators correspond to the gluon fields. Gluons are the gauge bosons of the strong interaction. The field tensor can be written as [10]

$$F_{\mu\nu}^a = \partial_\mu A_\nu^a - \partial_\nu A_\mu^a + g_s f^{abc} A_\mu^b A_\nu^c \quad (2.1)$$

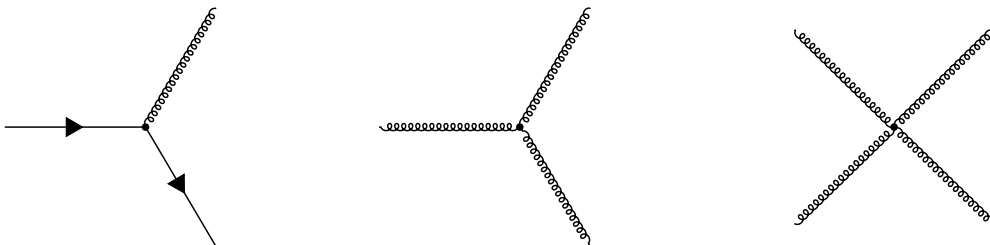
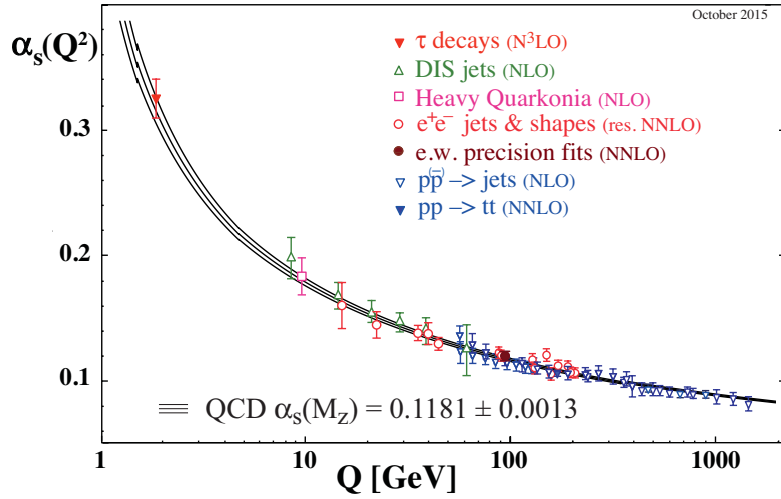


Figure 2.1: Vertices for QCD Feynman graphs. *Left*: Quark-gluon interaction. *Center*: Three-gluon vertex. *Right*: Four-gluon vertex


 Figure 2.2: The running coupling α_s in QCD [11].

with A^a the gluon fields, g_s the coupling constant and f^{abc} the so-called structure constants of the $SU(3)$ group. a , b and c are the color indices. The last term is specific to non-Abelian gauge theories and gives rise to interactions between the gauge bosons. The Lagrangian of QCD is

$$\mathcal{L} = -\frac{1}{4}(F_{\mu\nu}^a)^2 + \sum_q \bar{\psi}_{q,a}(i\gamma^\mu \partial_\mu \delta_{ab} - g_s \gamma^\mu t_{ab} A_\mu - m\delta_{ab})\psi_{q,b} \quad (2.2)$$

where repeated indices are summed over [11]. The explicit sum is over the quark flavors. The second part gives a $\bar{\psi}A\psi$ -term, which corresponds to a quark-quark-gluon vertex in the Feynman rules similar to the interaction vertex in quantum electrodynamics. In addition, now third and fourth order terms of the gluon fields appear in the first term of equation 2.2, which lead to vertices describing gluon interactions as shown in figure 2.1. This is a consequence of the fact that the gauge bosons themselves also carry (color) charge in QCD. Solving the corresponding renormalization group equation [10] leads at 1-loop to the result:

$$\alpha_s(\mu) = \frac{g_s^2}{4\pi} = \frac{2\pi}{11 - \frac{2}{3}N_f} \frac{1}{\ln \frac{\mu}{\Lambda_{\text{QCD}}}} \quad (2.3)$$

with the energy scale μ . N_f is the number of quark flavors which fulfill $4m_q^2 < \mu^2$. Λ_{QCD} is the location of the QCD Landau pole. A comparison to measurements is shown in figure 2.2. The running coupling decreases with increasing Q^2 [12, 13]. The small coupling at large momentum transfer - or equivalently, small distances - is referred to as asymptotic freedom. A direct consequence is that perturbative calculations - referred to as pQCD - only converge well for larger momentum transfers.

In the Lagrangian, left and right-handed quarks light quarks are decoupled, due to their small mass compared to the relevant scale Λ_{QCD} . However, the lowest-energy states of the vacuum do not have this symmetry. As a result, e.g. $\langle u\bar{u} \rangle$ has a nonzero expectation value even in the QCD vacuum. This phenomenon is called chiral symmetry breaking.

The lightest hadrons are bound quark-antiquark states (mesons) and triple-quark states (baryons) with zero combined color charge. So far, no objects with nonzero net color charge were found in the vacuum [11]. This property is called confinement. It has not been derived from first principles but is expected to follow from QCD.

2.1.2 The QCD phase diagram

From the principles of the previous section it follows that all quarks are hidden within the individual hadrons. Within the hadron, the strong interaction affects them comparatively little, but strongly confines them within a small volume. If the temperature of baryonic matter (or the QCD vacuum) is increased to sufficiently large values, pions can be produced thermally. If the number of baryons or the density of the thermal pions increases sufficiently, the volume of the hadrons fills up the vacuum. In this case, a single quark cannot be associated with a specific hadron [14]. This means, that at large temperatures and/or baryon densities, QCD matter can exhibit a phase transition to a state with deconfined quarks. From the above argument, this should happen at temperatures of the order of 1–2 times the pion mass or the QCD scale $\Lambda_{\text{QCD}} \sim 200 \text{ MeV}$ (a more thorough calculation may be found in [15]). The resulting state of deconfined matter is called the quark-gluon plasma [16].

Figure 2.3 shows a sketch of the phase diagram of QCD. The phase transition can only occur under extreme conditions like the high temperatures of matter shortly after the big bang. It is at present unclear whether the conditions inside some compact stars can also produce deconfined matter [18].

In the quark-gluon plasma, the chiral symmetry is restored. As a result, the masses of the quarks are their bare values. The thermodynamic degrees of freedom are gluons and quarks, while in the confined phase the degrees of freedom are the hadrons.

2.1.3 Lattice QCD

The running coupling allows for perturbative calculations at large momentum transfer. The regime of the QCD phase transition however is not easily accessible due to the large coupling. In such a regime, large successes have been made using discretized QCD

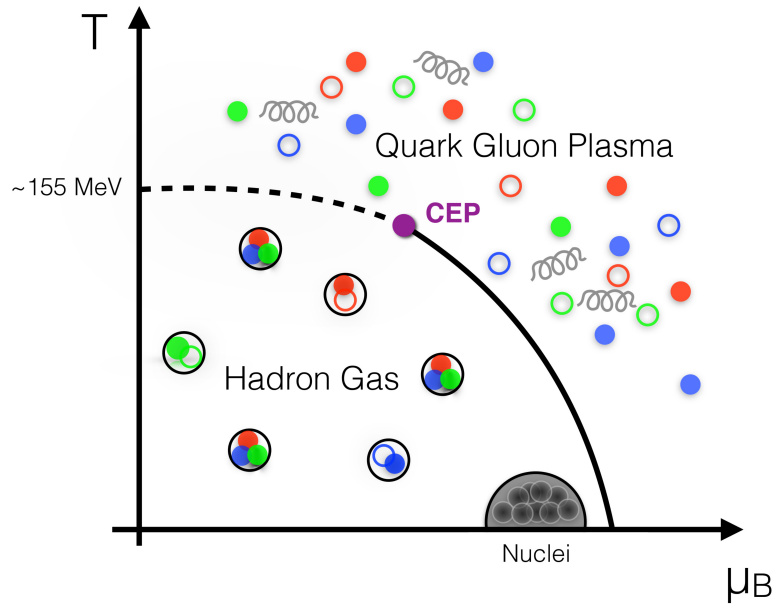


Figure 2.3: Phase diagram of QCD. (figure taken from [17])

calculations. This approach is called lattice QCD. Approaching a lattice spacing of zero and infinite lattice size should then recover QCD. The calculations are usually done using in Euclidean time $-i\tau = t$ which simplifies the calculation of the path integrals [19]. As a result it is difficult to access time-dependent dynamics and the calculations typically concern time-independent properties.

Calculations of the chiral susceptibility at different temperatures suggest a rapid crossover from hadronic matter to matter with restored chiral symmetry and deconfinement. This is shown in figure 2.4. The calculations were performed at vanishing baryon density. The transition temperature for the chiral symmetry restoration was estimated as [20, 21]

$$T_c = 154 \pm 9 \text{ MeV} . \quad (2.4)$$

Due to the smooth transition, the transition temperature is not defined precisely and depends on the observable [21, 22].

The lattice calculations [22, 23] can also make predictions about the equation of state of the deconfined matter. Figure 2.5 shows the results for pressure, energy density and entropy density. These can be used as input for the hydrodynamic calculations needed to describe heavy ion collisions.

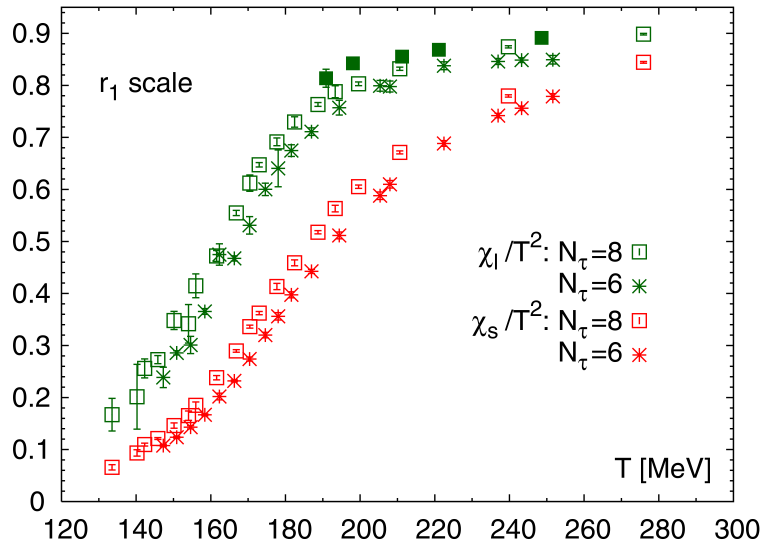


Figure 2.4: Chiral susceptibilities for light flavors and strangeness in a lattice QCD calculation. The rise suggests a rapid crossover for the chiral phase transition. (figure taken from [20])

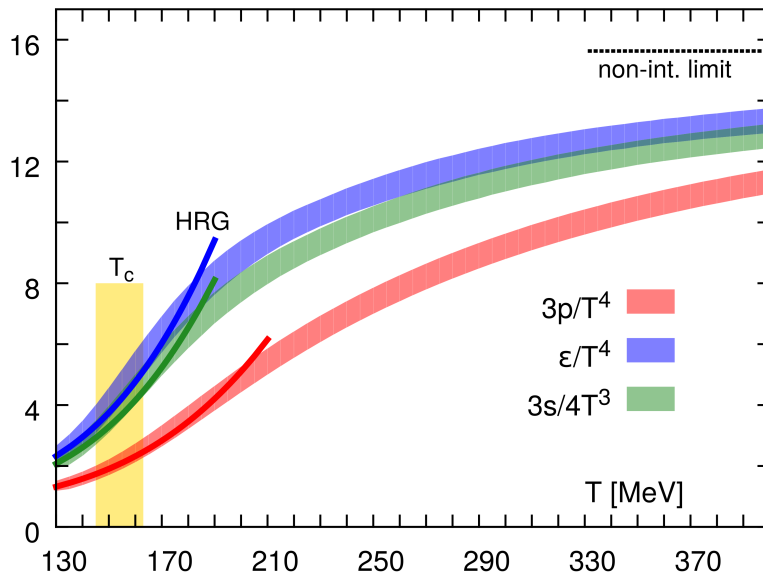


Figure 2.5: Lattice calculations for the thermodynamic quantities of the QCD matter. (figure taken from [23])

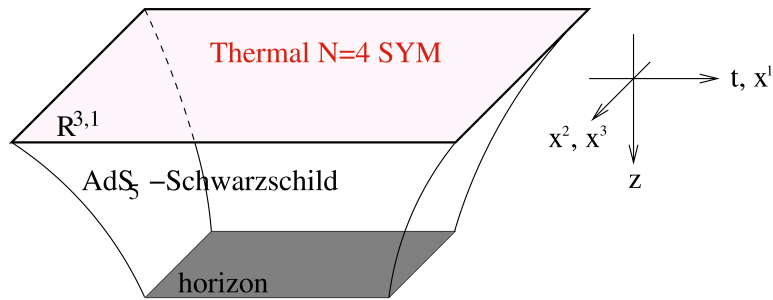


Figure 2.6: Visualization of the anti-de Sitter spacetime with black hole. The corresponding field theory can be understood to live on the boundary. (figure taken from [24])

2.1.4 Gauge/string duality

While many practical calculations in QCD make use of a weak-coupling approach, the so-called holographic principle has given analytical insights into the opposite, the strong coupling limit. The fundamental idea is the AdS/CFT correspondence [25]: A four dimensional $N = 4$ supersymmetric Yang-Mills theory in a flat space-time corresponds to a string theory in ten-dimensional anti-de Sitter space ($AdS_5 \times S^5$). The temperature in the field theory corresponds to the radius of a black hole (or black brane) in the string theory [26] as illustrated in figure 2.6. This breaks the conformal symmetry, by introducing a scale.

A very useful property of the correspondence is that a strong coupling in the field theory corresponds to weak gravity. In the limit of the coupling strength and the number of colors N_c going to infinity, the string theory reduces to a classical supergravity. In this case, the strings can either be approximated as point particles or as classical strings where the action can be calculated by a classical integral over the string world sheet. While the conformal field theory is not equal to QCD, the AdS/CFT correspondence can be used to gain a more thorough understanding of the properties of a field theory with strong coupling.

2.2 Heavy-ion collisions

Given the difficulty of accessing the time shortly after the big bang and the interior of compact stars, the only way to study the quark-gluon plasma is to create it experimentally. This can be achieved via ultrarelativistic heavy-ion collisions. Compared with -

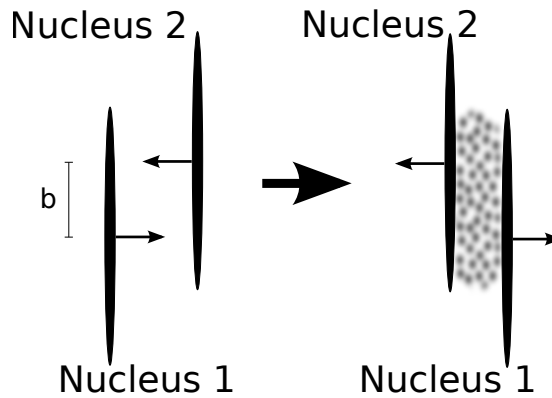


Figure 2.7: Sketch of a nucleus-nucleus collision shortly before (*left*) and after (*right*) the initial interactions.

for example - the periodic boundary conditions of the lattice calculations, this system is much more complex. Most observables thus make use of the fact that the hadronic matter equilibrates to some extent, which greatly simplifies theoretical calculations of that part of the process and allows for phenomenological models to be applied. Given that the collision itself is not accessible to detectors, all information about the processes must be deduced from the final state particles that are created. The following paragraphs will give a brief overview of the different phases of the collision.

2.2.1 Initial State

In the laboratory frame, the two colliding nuclei are highly Lorentz-contracted. As sketched in figure 2.7, the collisions will not usually be head-on. The nuclei are complex systems consisting of interacting nucleons whose configuration differs from one collision to the next. To access the initial moments of the collision, it is useful to connect the complex state of the nuclei with initial nucleon-nucleon collisions such as those measured in the proton-proton collisions at the LHC. In particular, it is useful to understand the typical numbers of nucleon-nucleon collisions and the number of participating nucleons in the nuclei.

A fundamental value to describe the collision geometry is the impact parameter of the two nuclei b . For a larger impact parameter, typically fewer nucleons interact and fewer particles are produced in the collision. The connection of the collision geometry and the distribution of nucleon-nucleon interactions can be estimated using Glauber-modeling [27]. This approach starts with measured or modeled density distributions of the nucleons in the nucleus. The fundamental assumption is the independent distribution of all nucleons according to this common probability density $\rho_A(x, y, z)$ and that this

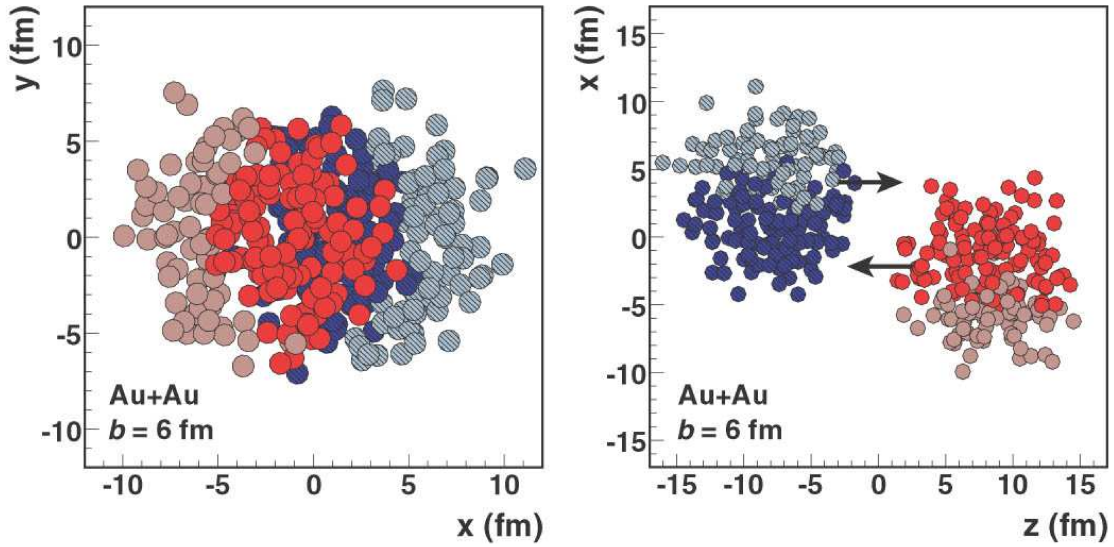


Figure 2.8: Example of a Glauber Monte Carlo calculation for Au–Au collisions. (figure taken from [27])

distribution is not changed by individual collisions. In this case, it is useful to integrate out the beam-direction and define: $T_A(x,y) = \int \rho_A(x,y,z) dz$. The expectation value for two nucleons to interact is then proportional to the nuclear overlap function:

$$T_{AB}(b) = \int T_A(\vec{x}) T_B(\vec{x} - \vec{b}) d^2A . \quad (2.5)$$

In practice, it is useful to solve this using numerical approaches. The Glauber Monte Carlo approach randomly distributes the nucleons of each nucleus according to the density distribution. The nuclei are overlaid according to the impact parameter. In the simplest approach, the nucleons are modeled as solid disks: if they overlap, an interaction takes place. By repeating this sufficiently often, it is simple to extract the expected number of binary (nucleon-nucleon) collisions N_{coll} and the expected number of participating nucleons in a collision N_{part} . In this way, it is also possible to define classes of the collision centrality. For the present analysis only the 20% most central collisions were considered in the Pb–Pb collisions. In practice, the centrality class definition is based on detector signals as explained in chapter 4. The Glauber model can then be used associate this class with an impact parameter and make estimates about the nuclear overlap function and the number of binary collisions as shown in table 2.1. The number of produced particles scales approximately with N_{part} , while hard processes (like the creation of heavy quarks) scale with N_{coll} .

Centrality	b	$\langle N_{\text{coll}} \rangle$	$\langle N_{\text{part}} \rangle$	$\langle T_{\text{AA}} \rangle$
0–20%	0–7 fm	1211	308	18.915

Table 2.1: Glauber model estimates for the centrality range used in the analysis based on [28].

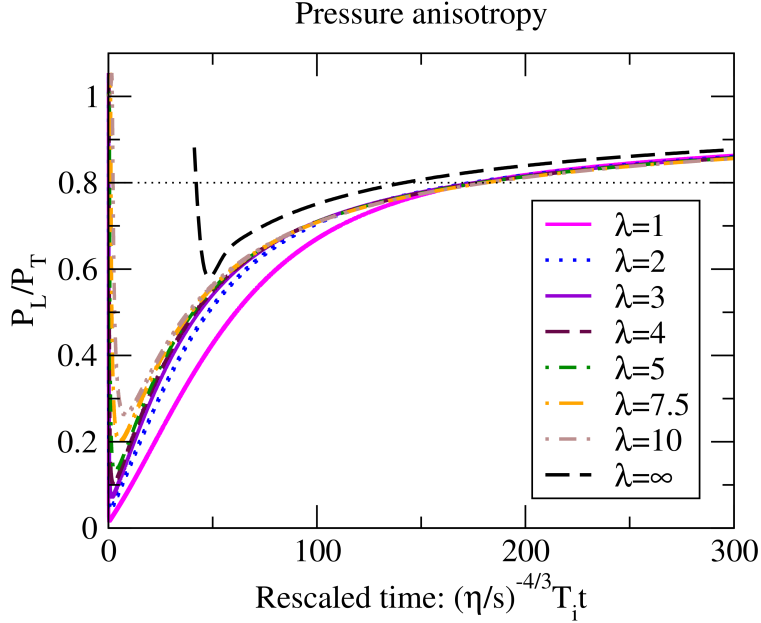


Figure 2.9: Comparison of equilibration with a weak-coupling approach and in AdS/CFT. (figure taken from [29])

2.2.2 Equilibration

The equilibration process is associated with an intermediate strength coupling. It can be approached by a strong-coupling approach based on holography [29]. Alternatively, a weak-coupling approach can be used. In this case, the high occupation numbers in the early phases allow for real-time lattice calculations [30, 31]. For the later times, a kinetic theory can be applied [32]. Remarkably, both approaches give similar predictions for a rapid equilibration as shown in figure 2.9. Comparison to measurements suggests an early onset of the applicability of hydrodynamics of the order of $1 \text{ fm}/c$, although this might already appear far from equilibration of the longitudinal and transverse pressure [32].

Experimentally, an interesting question about these processes appeared in the form of the direct photon puzzle: Photons can traverse the QCD medium easily, because they do not participate in the strong interaction. Thermal photons are produced with a strong

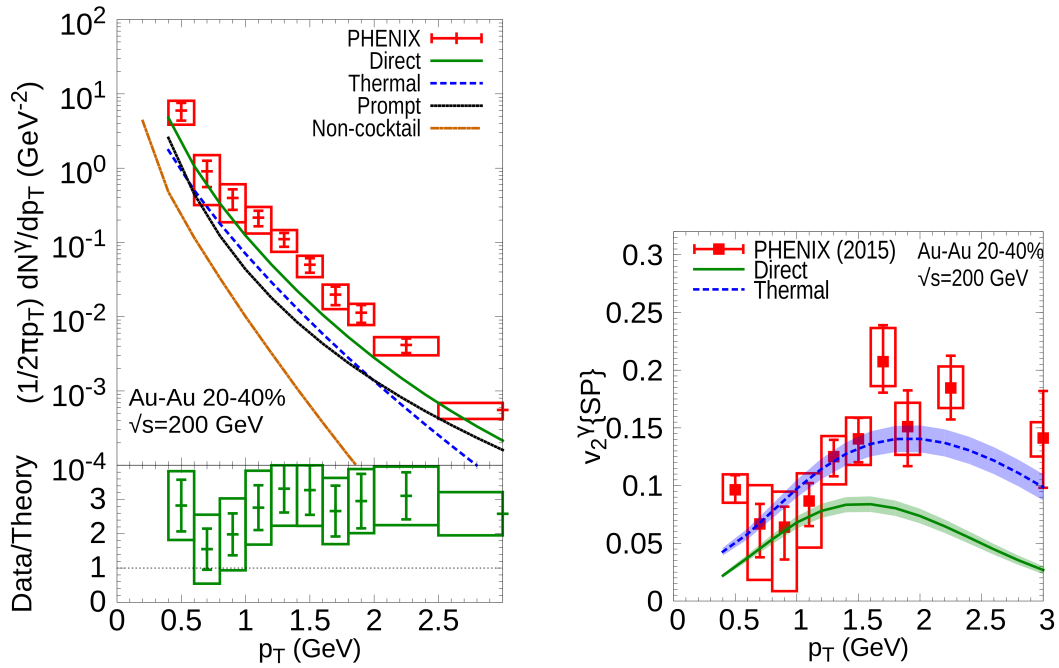


Figure 2.10: *Left:* p_T -distribution and *Right:* anisotropy of direct photons in Au–Au collisions. (figure taken from [33])

dependence on the temperature and comparison of theoretical predictions with measurements suggest a production in the early phases of the collision. On the other hand, measurements of the azimuthal anisotropy (as discussed in the next subsection) suggest production after a significant hydrodynamic flow has developed - which is associated with equilibration. This is shown in figure 2.10.

2.2.3 Flow

The local thermodynamic equilibrium simplifies the description of the bulk of the matter. To estimate general parameters like the system size and the lifetime, it is possible to make use of the correlations between identical bosons in phase space in a similar way as the Hanbury Brown-Twiss approach of using photons to deduce stellar radii. The interpretation of the resulting volume and time is complex but the results from ALICE as shown in figure 2.11 suggest a significantly larger volume of the fireball at the LHC compared to the lower-energy experiments. The results point to a lifetime of the system of the order of 10 fm/ c .

Qualitatively, the collective expansion of the medium can be identified from the p_T -distributions of charged particles. Figure 2.12 shows the resulting distributions for charged pions, kaons and protons. Comparison between the pp and Pb–Pb results and

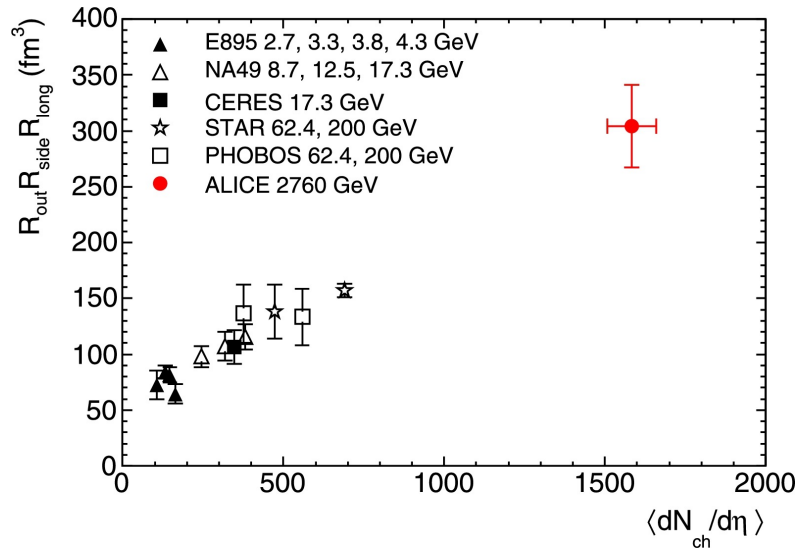


Figure 2.11: Product of the three HBT radii, which gives an estimate for the volume of the region of homogeneity. (figure taken from [34])

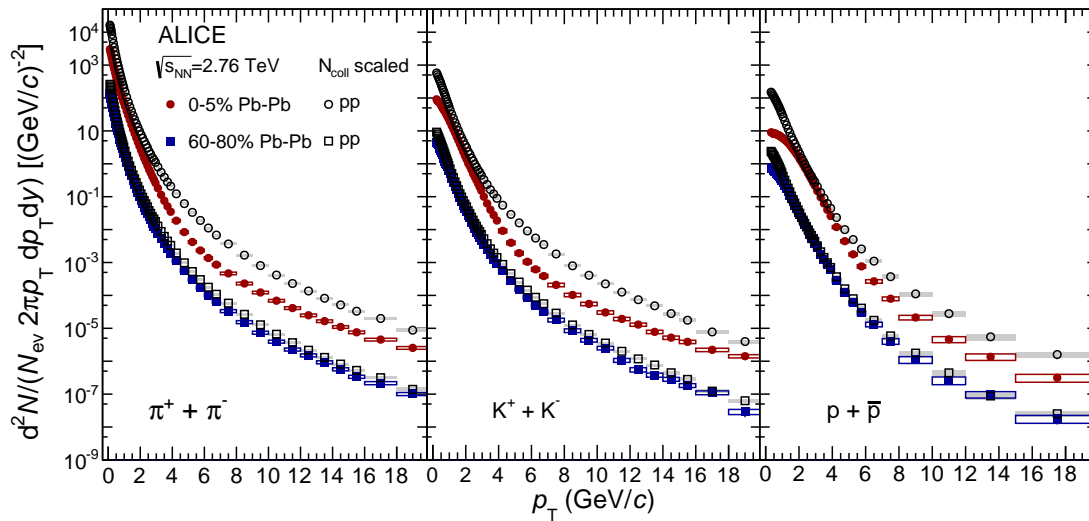


Figure 2.12: p_T -distributions of identified charged particles in Pb–Pb collisions measured with ALICE. (figure taken from [35])

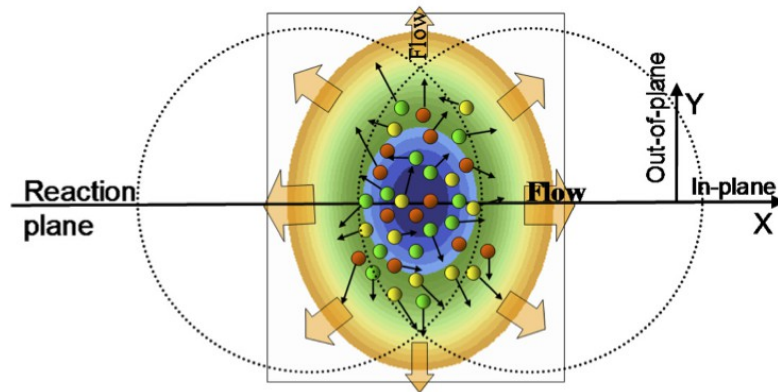


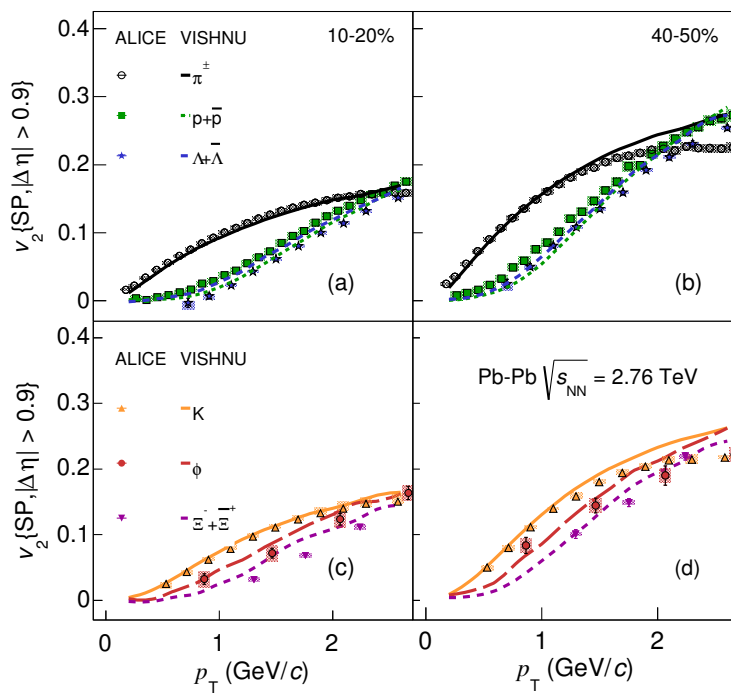
Figure 2.13: Example of an event plane of a collision.

the central and peripheral Pb–Pb results shows that the particles are pushed towards larger transverse momenta. The effect is stronger for the heavier particles, which is consistent with the expectation that the particles move at the same velocity.

To quantify the collective motion of particles within the medium, it is useful to consider the effects of the initial anisotropy of the system. Figure 2.13 shows the collision geometry in the transverse plane. In non-central collisions, the overlap region of the nuclei is almond-shaped (in the transverse plane). The two centers of the nuclei define the so-called reaction plane. The extent of the interaction region is smaller in this direction. Fluctuations in the initial state cause additional anisotropy. The effect of the initial anisotropy on the final state yields information about the properties of the quark-gluon plasma.

For this purpose, the anisotropy of the final state can be compared to predictions from hydrodynamic simulations. Ideal hydrodynamics is based on a set of conservation equations for the energy-momentum tensor and the baryon number as well as an equation of state. In viscous hydrodynamics, additional dissipative terms appear. The first-order Navier-Stokes equation gives rise to superluminal signals [36], so a higher-order analogue is needed, such as the Israel-Stewart equation [37]. The equation of state is often based on lattice calculations. For very high temperatures, the running coupling becomes smaller. In this limit, the QCD medium should behave as an ideal gas. Since $\alpha(T_c)$ is still sizeable and the typical energy of particles should be of order T , this ideal behavior does not necessarily appear at temperatures close to T_c .

The initial spatial anisotropy (figure 2.13) is converted into a momentum anisotropy of the final state, which is used to access the fluid dynamic properties of the medium experimentally. For an ideal gas-like expansion, the momentum distribution should be



ALI-DER-85768

Figure 2.14: Elliptic flow v_2 of different hadron species together with the results of a simulation using viscous hydrodynamics. (figure taken from [38])

isotropic. In the case of interactions, there is a pressure gradient from the center of the overlap region to the vacuum outside. This leads to an acceleration of the medium along the gradient. Thus, more particles can be expected in-plane and with larger momenta. One approach to quantify this is via the Fourier-coefficients of the azimuthal particle distribution [38]:

$$v_n = \langle \cos[n(\varphi - \Psi_n)] \rangle . \quad (2.6)$$

For v_2 , the angle Ψ_n can be the reaction plane. As the higher harmonics are the result of fluctuations, they would cancel out for this choice. Thus for these, Ψ_n is calculated from the azimuthal particle distributions themselves for each event[39].

Measurements like the one shown in figure 2.14 show the dependence of the v_2 on the particle mass that is expected due to the fact that all particles come from the same medium. Comparisons to theoretical calculations point to a medium that is close to an ideal liquid. This suggests strong interactions within the medium [36]. Calculations using the AdS/CFT correspondence in the infinite coupling limit yield a shear viscosity of $\eta/s = \frac{1}{4\pi}$ for a large class of theories with a gravity dual [26], which is interpreted as a lower bound [40]. Measurements suggest that the QGP created in heavy-ion collisions comes close to this bound.

2.2.4 Hadronization

As the fireball from the collision expands, the temperature decreases until it drops below the transition temperature. After sufficient expansion, the matter again consists of individual hadrons (and a few leptons) that cease to interact. This freeze-out process is complex, but broadly defined by two relevant temperature scales: The first is the chemical freeze-out after which the particle composition of the matter ceases to change. The second is the kinetic freeze-out, after which the particles do not significantly interact any more.

The relative abundances of different hadron species can be well described by assuming a hadron gas in chemical equilibrium including the relevant resonances [42]. This approach is based on a grand-canonical formalism, which requires a baryon chemical potential and a temperature for the chemical freeze-out as input. Inverting this approach, temperature and baryon chemical potential can be deduced from the hadron abundance ratios. For central Pb–Pb collisions at LHC energies this yields a temperature of 156 MeV with vanishing baryon chemical potential μ_b as shown in figure 2.15.

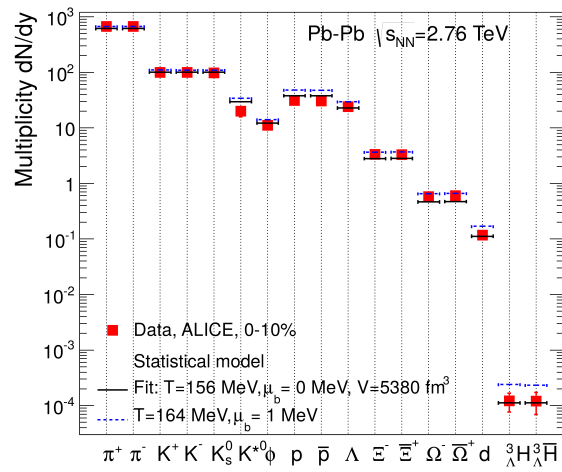


Figure 2.15: Results of the statistical hadronization model compared to measurements with ALICE. (figure taken from [41])

Chapter 3

Heavy Quarks in heavy-ion collisions

In addition to the light hadrons and photons discussed in the previous chapter, heavy quarks are a useful probe of the quark-gluon plasma. The heavy quarks - meaning charm and beauty - are generated in the initial interactions of the collision itself and then traverse the produced medium. A study of the charm and beauty hadrons produced after the hadronization gives insight into the transport properties of the medium. The complex processes involved in the production, interaction with the medium and hadronization require thorough theoretical methods as well as a diverse set of measurements to disentangle the different effects. This chapter will present a short overview of the current understanding of heavy quarks in the QGP to motivate the measurement of electrons from beauty-hadron decays – the main subject of this work.

The nuclear modification factor R_{AA} has proven to be a useful tool to quantify the interaction with the medium. It relates measurements in pp and Pb–Pb (or p–Pb) collisions by comparing a nuclear collision to a superposition of an equivalent number of independent nucleon-nucleon collisions. Given known p_T -differential cross-sections in pp and Pb–Pb, the total cross section should scale as $d\sigma_{AA}/dp_T = A^2 d\sigma_{pp}/dp_T$ if the individual collisions do not affect each other and assuming only hadronic interactions. A is the mass number of the colliding nuclei. The nuclear modification factor shows the change from this hypothesis:

$$R_{AA} = \frac{d\sigma_{AA}/dp_T}{A^2 d\sigma_{pp}/dp_T}, \quad (3.1)$$

An example is shown in figure 3.1. The Z^0 bosons and in particular the leptons produced in its decay do not participate in the strong interaction and should therefore not be affected by the medium. Accordingly, the R_{AA} is consistent with unity within the uncertainties. To make R_{AA} -measurements in different centrality classes, it is useful to

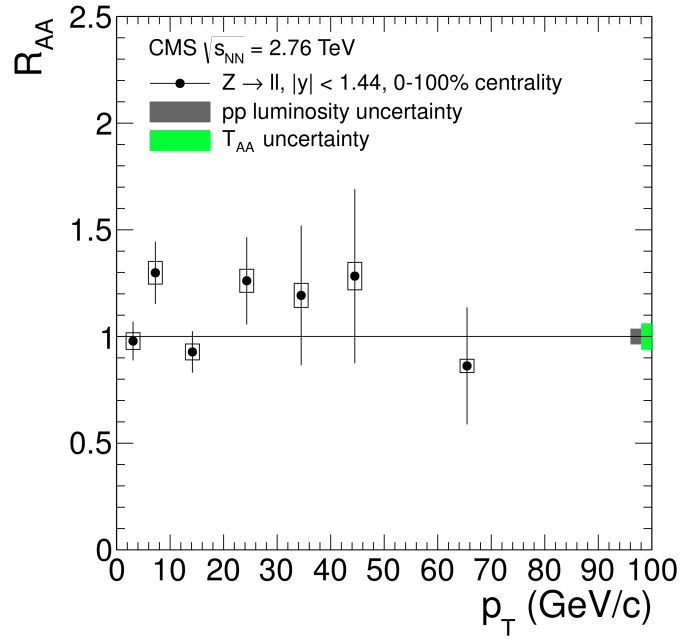


Figure 3.1: Nuclear modification factor of Z^0 bosons measured by the CMS collaboration. (figure taken from [43])

generalize equation 3.1. Given, that the hard processes scale with the number of binary collisions, the equation can be expressed as

$$R_{AA} = \frac{dN_{AA}/dp_T}{\langle N_{coll} \rangle dn_{pp}/dp_T} = \frac{dN_{AA}/dp_T}{\langle T_{AA} \rangle d\sigma_{pp}/dp_T}, \quad (3.2)$$

with T_{AA} the nuclear overlap function introduced in section 2.2.1 and dN/dp_T the p_T -differential particle yield per collision. This definition can be used for selections in centrality. Thus, the R_{AA} compares the p_T -distribution of particles from one proton-proton collision with one binary collision of two nucleons in Pb-Pb.

3.1 Initial hard scatterings

Due to the large mass of the heavy quarks compared to the temperature of the medium at LHC energies essentially all charm and beauty quarks are produced in the initial nucleon-nucleon collisions. This clearly defined moment of creation makes them well-calibrated probes of the QGP. The mass is not only large compared to the expected QGP temperatures but also compared to Λ_{QCD} allowing for perturbative methods to calculate the production cross sections (as discussed in section 2.1.1). The calculations typically make use of factorization: The assumption that the production processes can be split

up into terms representing the (hard) interactions of the partons and the nuclear parton distribution functions (nPDFs). It is typically assumed that the medium interactions and fragmentation processes are also independent and thus factorize as well.

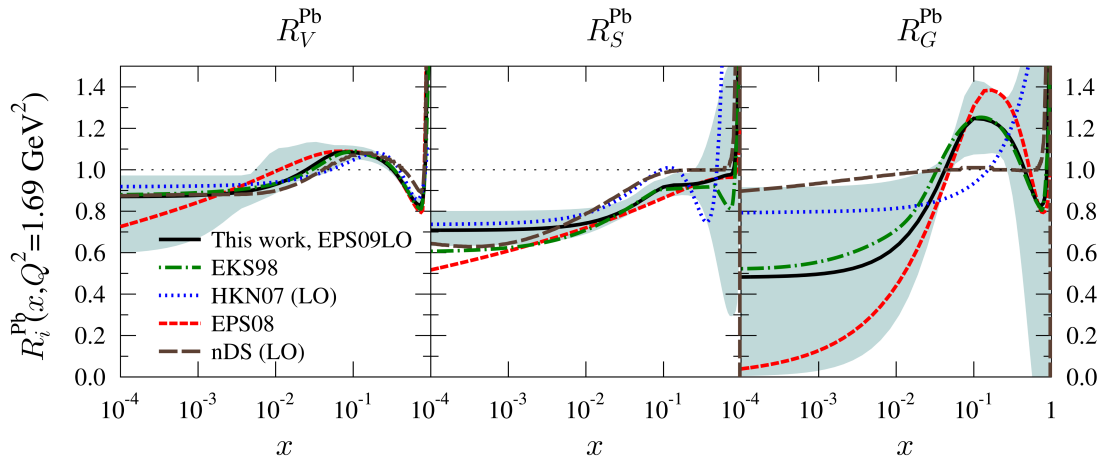


Figure 3.2: Ratio of PDFs for nucleons in Pb and protons from different calculations. Shown are the modifications for valence quarks (*left*), sea quarks (*center*) and gluons (*right*). (figure taken from [44])

In this approach, the nPDFs are universal objects [10], meaning that they can be applied in all collision systems. The nPDFs generally differ from the PDFs in the proton-proton collisions. By combining a variety of measurements and theoretical calculations, the change can be estimated. Many calculations make use of the EPS09 set of nPDFs [44]. The resulting modifications to the PDFs of protons are shown in figure 3.2.

The pQCD processes to create heavy quarks are at leading order quark-antiquark annihilation $q + \bar{q} \rightarrow Q + \bar{Q}$ and gluon-gluon fusion $g + g \rightarrow Q + \bar{Q}$. Higher order processes contain the virtual corrections to these processes as well as the processes $q + \bar{q} \rightarrow Q + \bar{Q} + g$, $g + g \rightarrow Q + \bar{Q} + g$ and $g + q(\bar{q}) \rightarrow Q + \bar{Q} + q(\bar{q})$ [47]. The measurements in pp collisions provide experimental verification of these calculations. Figure 3.3 (left) shows the comparison of the measured beauty cross section and calculation using a fixed-order plus next-to-leading logarithms (FONLL) approach, which resums some of the logarithmic term that appear in the calculations. Even though, the R_{AA} is used to quantify the effects of the medium, its value also depends on the slope of the initial p_T -distribution. If the p_T -distribution drops off more quickly with p_T , the R_{AA} will have lower values for the same energy loss. For this reason, models of the interaction of heavy quarks with the medium need sufficiently accurate p_T -distributions as input.

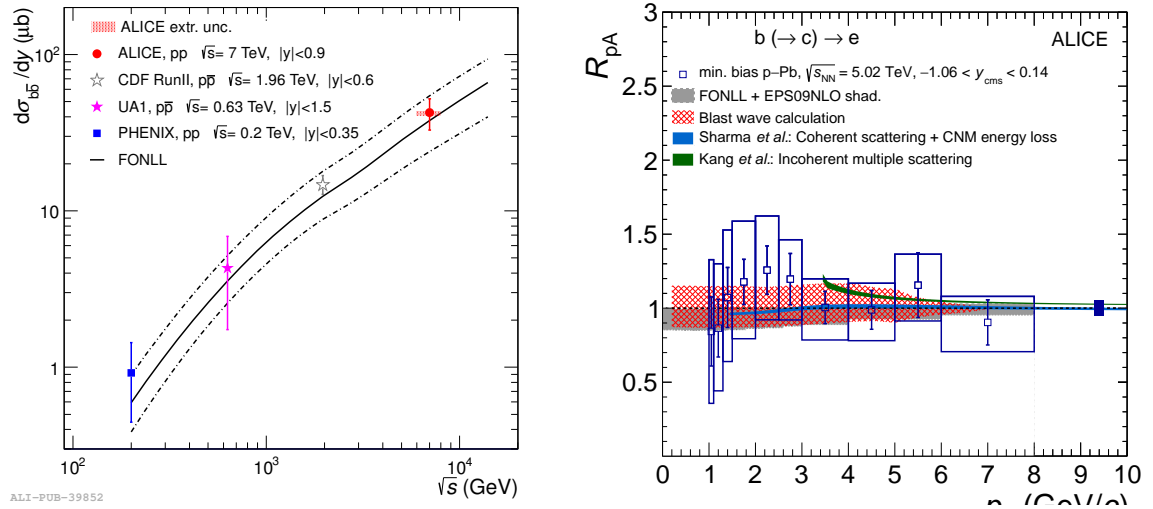


Figure 3.3: *Left*: Comparison of beauty cross sections in proton-proton collisions at different energies with FONLL calculation. (figure from [5], update in preparation [45]) *Right*: R_{pA} of electrons from beauty-hadron decays in p-Pb collisions in comparison with models. (Publication in preparation [46])

3.2 Heavy flavors during equilibration

To disentangle the interaction of heavy quarks with the quark-gluon plasma from those that would also be present without it, it is useful to consider proton-nuclei collisions, such as the p-Pb collisions at the LHC. These are not only sensitive to changes in the parton distribution functions, but also to additional effects specific to colliding nuclei. They can include multiple scatterings of the partons [48] or energy loss of the heavy quarks in the nuclei. Figure 3.3 shows a measurement of beauty-hadron decay electrons in p-Pb collisions with no significant deviation from the correspondingly scaled pp result, suggesting that these effects are most likely small.

Theoretical calculations for the interaction with the medium usually assume thermalization of the medium. Given the short timescale (≈ 0.3 fm/ c [49]) of the thermalization compared to the lifetime of the medium (≈ 10 fm/ c) this appears justified. More detailed analysis suggests only a small influence of the precise description of the energy loss in the non-thermalized medium [50, 51].

3.3 Interaction with the thermalized medium

The interaction of heavy quarks with the QGP can provide useful information about the deconfined matter. Fast quarks lose energy in the interactions. Given that the heavy

quarks are produced early in the collision at a fairly well known rate and that there is hardly any pair annihilation due to the small number density, the heavy quark measurements serve as a type of tomography of the medium. The description of the energy loss can broadly be separated into two categories: Weak and strong coupling approaches. In the weak-coupling approaches, the interaction with the medium is interpreted as interactions of the heavy quarks with the constituents of the medium, which are then included in a transport equation. In the strong coupling approach, the heavy quark and the medium are interpreted according to the AdS/CFT correspondence. In the following, the general principles of the strong coupling approaches based on AdS/CFT as well as weak-coupling approaches using pQCD will be discussed as the extreme cases followed by a brief overview over some currently used models. In general, all energy loss formalisms need to be combined with the background of an expanding medium to describe measurements at low transverse momenta.

3.3.1 Heavy-quark energy loss in AdS/CFT

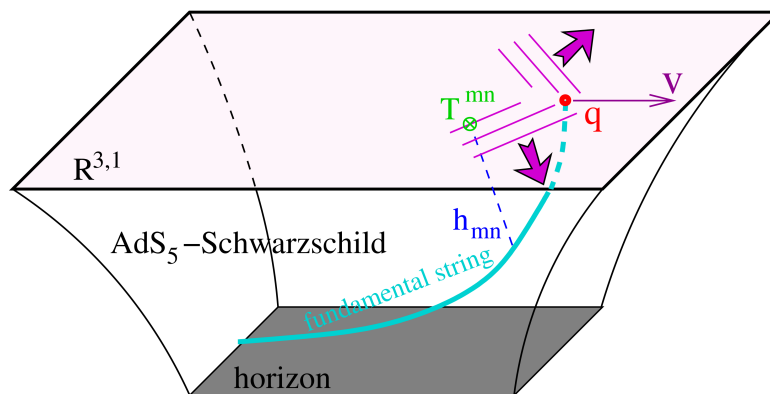


Figure 3.4: Sketch of the interaction of heavy quarks with the medium in AdS₅/CFT. (figure taken from [52])

The calculation using the holographic principle is done assuming that the typical momenta in the medium are much smaller than the quark mass and that the change in momentum is small over the time scales considered. This results in a quark that moves at a constant velocity for the purpose of calculation. Associated with the world line of the quark is the so-called Wilson line. It is an important quantity for the effect of the medium on heavy quarks and describes the rotation of the parton's color due to the field [26]. The dual description of the Wilson line is a (macroscopic) string hanging down into the AdS₅-space as sketched in figure 3.4. The equation of motion can be obtained

by extremizing the Nambu-Goto action obtained by integrating over the world-sheet of the string. The result from the corresponding calculations is

$$\frac{dp}{dt} = -\frac{\pi\sqrt{\lambda}T^2}{2m_{\text{quark}}}p, \quad (3.3)$$

which is a mass-dependent drag force [24, 26]. The result also shows a clear dependence of the drag on the mass of the heavy quark.

3.3.2 Heavy-quark energy loss in pQCD calculations

In the weak-coupling approaches, the interaction of the heavy quark is interpreted as interactions with individual quarks and gluons in the QGP. To connect knowledge about the scattering processes with the change in the phase-space distribution of the heavy quark f_Q , a transport equation is used. The Boltzmann equation describes how this evolution occurs with a known collision integral $C[f_Q]$ and an external force F :

$$\left[\frac{\partial}{\partial t} + \frac{\vec{p}}{E_p} \frac{\partial}{\partial \vec{x}} + \vec{F} \frac{\partial}{\partial \vec{p}} \right] f_Q(t, \vec{x}, \vec{p}) = C[f_Q] \quad (3.4)$$

The collision integral contains contributions from all processes considered in the calculation. Given that the momentum exchange per collision typically is small compared to the heavy quark momentum, the scattering rate can be expanded in powers of the momentum transfer, yielding the Fokker-Planck equation. In this case, the interaction is represented by the first and second moments of the scattering amplitude, which appear in transport parameters for momentum friction and diffusion [4]. The Fokker-Planck equation is often implemented using a Langevin process [3]:

$$\frac{d\vec{p}}{dt} = -\eta_D(p)\vec{p} + \vec{\xi}(t) \quad (3.5)$$

$$\frac{d\vec{x}}{dt} = \frac{\vec{p}}{E}, \quad (3.6)$$

which allows position updates and includes a drag in the first term and a stochastic diffusion part in the second.

The interactions can broadly be categorized into elastic and radiative processes. In analogy to electromagnetic Bremsstrahlung, which is suppressed with the fourth power of the mass, elastic processes are expected to dominate at lower temperatures and heavy quark momenta, while radiative processes should become more important at higher energies. A prediction of the separate contributions is shown in figure 3.5. Figure 3.6 shows Feynman diagrams associated with elastic $2 \rightarrow 2$ processes. For the exchange

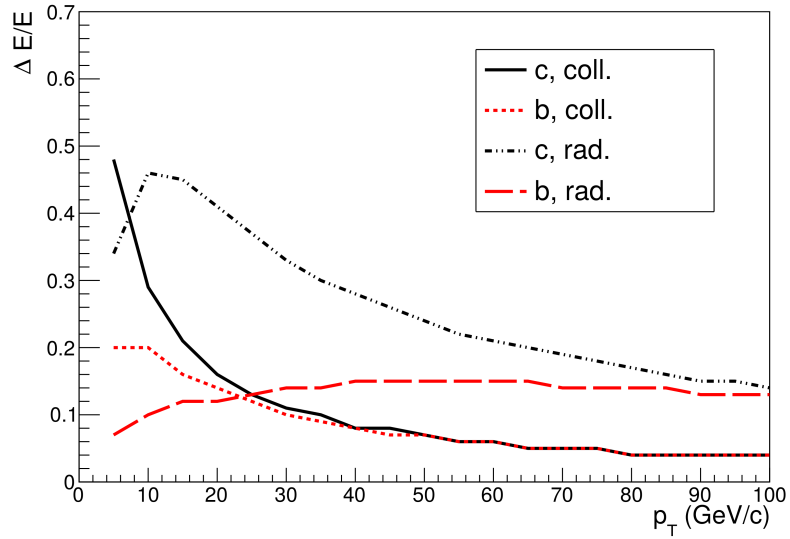


Figure 3.5: Fractional energy loss due to radiative and collisional processes separately based on the framework described in [53–55]. (figure taken [56])

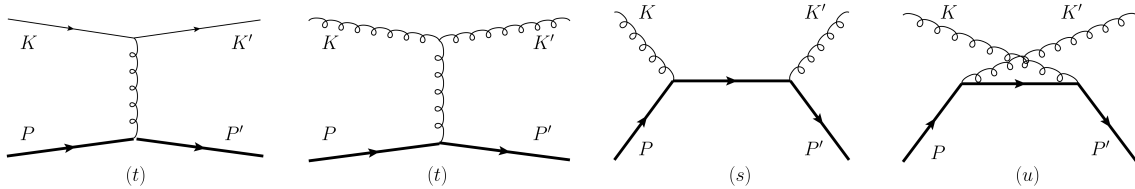


Figure 3.6: Leading order Feynman diagrams associated with elastic interactions of heavy quarks with the medium. (figure taken [57])

of soft gluons, a screening mass can be introduced as an infrared regulator [4]. This incorporates the Debye screening of the medium at large distances.

The radiative ($2 \rightarrow 3$) processes with an additional gluon in the final state are expected to be suppressed for small emission angles of the gluon relative to the momentum of the heavy quark [58]. This so-called "dead cone" effect leads to the expectation of a larger energy loss by light quarks compared to heavy quarks and of charm quarks compared to beauty quarks. In addition, soft gluons produced in separate interactions may interfere. This happens if the wavelengths of the gluons are large compared to the distance between two scattering centers. Since the interference is destructive, this Landau-Pomeranchuk-Migdal effect leads to a suppression of the radiation [59, 60]. Some care has to be applied with this effect, given that the Boltzmann equation assumes independence of the scatterings. It can for example be included by an effective description in the collision integral [61]. The description of the interaction gives rise to medium parameters for the Debye mass of the gluons or the mean free path between interactions which do not directly appear for example in the framework of the AdS/CFT description.

3.4 Hadronization

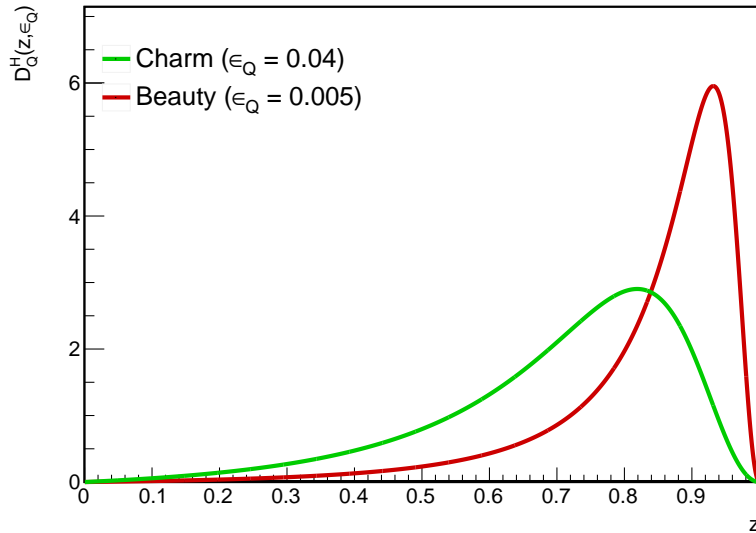


Figure 3.7: Petersen fragmentation functions for typical [4] choices of ϵ_Q

An advantage of the use of heavy quarks as probes of the quark-gluon plasma is that there is a clear association of the heavy quark in the medium with the heavy

valence quark in a resulting hadron. To gain access to the kinematics of the heavy quark, it is important to understand how the momentum of the quark in the medium relates to the momentum of the resulting hadron. At large momenta in the vacuum, the approach is usually to assume a universal (i.e. independent of the collision system) function describing the probability distribution for the hadron possessing a particular fraction of the quark momentum $z = p_h/p_Q$. This fragmentation function can then be fixed in one collision system (e.g. e^+e^-) and applied to others [4]. A frequently used form for the fragmentation function is the Peterson fragmentation function [62]

$$D_Q^H(z, \varepsilon_Q) \sim \frac{1}{z[1 - 1/z - \varepsilon_Q/(1-z)]^2}, \quad (3.7)$$

where ε_Q is a parameter that controls the shape of the distribution, which has a maximum at $z \approx 1 - 2\varepsilon_Q$ and a width of $\approx \varepsilon_Q$. The parameters for different quark flavors with masses m_Q are connected by the relation $\varepsilon_Q \sim 1/m_Q^2$ [62]. Examples for charm and beauty are drawn in figure 3.7.

In heavy-ion collisions, in particular for quarks at lower momenta, this approach is no longer valid. Collective effects like the flow of the surrounding medium become important. An important mechanism for the hadronization is the idea of recombination of heavy-quarks with thermal light quarks from the surrounding medium. Several different descriptions are used for this effect, giving different predictions also for the relative yield of different charm and beauty hadron species. A central point from the fragmentation in vacuum does typically still apply: The correlation of the quark momentum and the hadron momentum is stronger for beauty quarks than for charm quarks.

3.5 Theoretical models

In the following a few different theoretical models will be compared.

The **BAMPS**, or Boltzmann Approach to MultiParton Scatterings model makes use of the Boltzmann equation both to model the medium expansion and the propagation of the heavy quarks in the medium [63]. The individual interactions are calculated based on pQCD. These calculations include $2 \rightarrow 2$ elastic scatterings and $2 \rightarrow 3$ radiative [61] processes and feature a running coupling. Similar pQCD approaches like the **MC@sHQ**[64] use a hydrodynamic simulation for the background, while others consider only the initial (Glauber modelled) fluctuations like the **WHDG**[65].

The **TAMU** model makes use of results from lattice QCD to extract information about the QCD potentials as an input for the elastic scatterings [66]. **POWLANG**

makes the comparison more directly via a force-force correlator in lattice QCD [67] or by using hard thermal loop calculations [57].

For AdS/CFT calculations it is difficult to make quantitative predictions due to the fact that no exact gravity dual for QCD is known. In the approach of *Horowitz*, data from RHIC is used to constrain the parameters of the drag energy loss within reasonable limits, which can then be scaled to the LHC energies [65].

3.6 Measurements

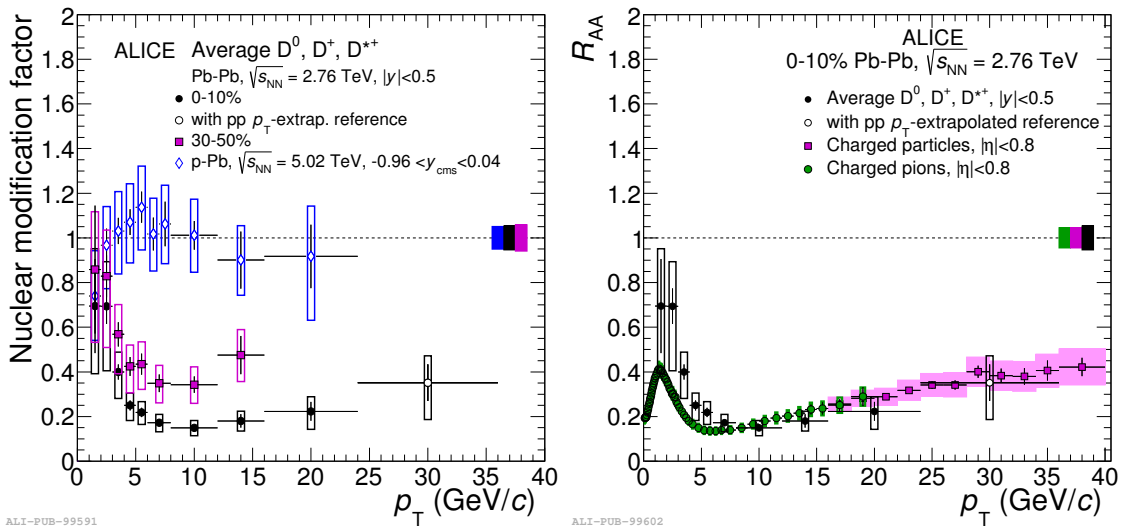


Figure 3.8: *Left:* R_{AA} and R_{pA} of D mesons in Pb–Pb collisions at LHC energies with ALICE. *Right:* Comparison to pions and charged hadrons.(figure taken [68])

To clearly separate medium effects from those present without a QGP, it is often useful to compare the nuclear modification factors of central and peripheral nuclear collisions with those in p–Pb. Figure 3.8 (left) shows the resulting nuclear modification factors for D mesons measured by ALICE [68]. The measurement in p–Pb does not show any effects that are significant with respect to the uncertainties. For the Pb–Pb collisions, there is a clearly visible effect.

The total number of heavy quarks is mostly independent of the formation of a QGP. The reason for this is the low density of heavy quarks in the medium which makes quark-antiquark annihilation unlikely. The R_{AA} thus describes mostly a migration in phase space, where the typical momenta of the heavy-flavor hadrons decrease. Nevertheless, an R_{AA} lower than one is typically referred to a suppression. For a total conservation of the D mesons, the R_{AA} must necessarily be above one at some point. The reason that this

is not the case for the measured range is the cold nuclear effects at low momentum [69], which are difficult to discern in the p–Pb result. As expected, the suppression is weaker for the more peripheral collisions due to the smaller volume of the medium. Surprisingly, the suppression is of a similar order as that of the light hadrons (figure 3.8, right).

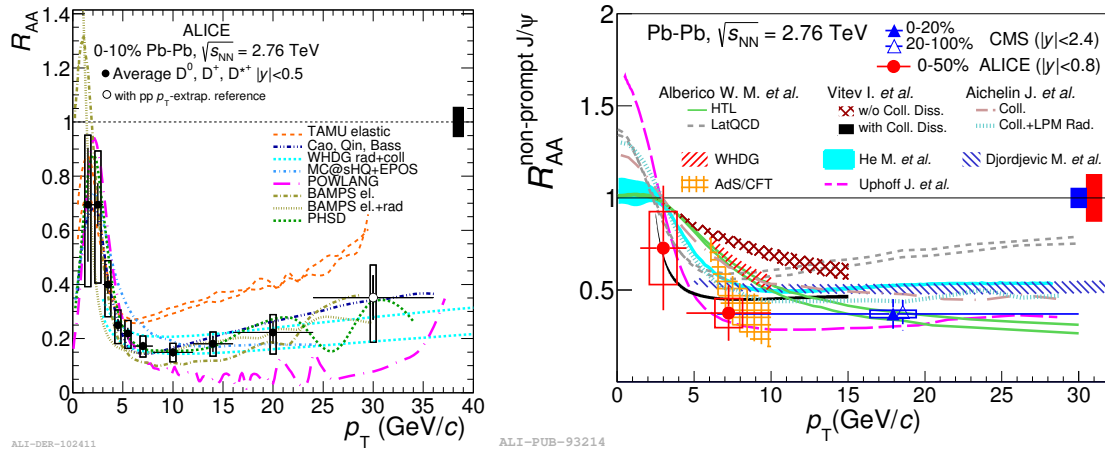


Figure 3.9: R_{AA} of D mesons (left) and non-prompt J/ψ (right) compared with theoretical models. (figures taken [68, 70])

One approach to the measurement of beauty quarks is the measurement of non-prompt J/ψ mesons. These can result from the decay of beauty hadrons. A comparison to theoretical models is shown in figure 3.9 together with the calculations for D mesons. The measurements for the non-prompt J/ψ are currently integrated over wider ranges of the transverse momentum and centrality compared to the D mesons. Given the similar R_{AA} for light hadrons and charm mesons, it is still an interesting question how the expected mass dependence of the energy loss is realized in nature.

A complementary approach to the measurement of hadrons is the measurement of b-jets. The jet energy also contains contribution from the particles associated with the hadronization process and thus can give a close approximation of the energy of the quark after the interaction with the medium. The experimentally reconstructed jet can also contain particles produced in the interaction with the medium which gives some sensitivity to the understanding of the energy loss processes. Figure 3.10 (left) shows the nuclear modification factor for beauty jets measured at LHC energies [71]. A clear suppression is visible with the measurement starting at $p_T = 80$ GeV/c.

To access the lower momenta, an indirect measurement based on the electrons from beauty-hadron decays is useful. The measurement in Au–Au collisions at $\sqrt{s_{NN}} = 0.2$ TeV given in figure 3.10 (right) shows the different nuclear modification factors for charm and

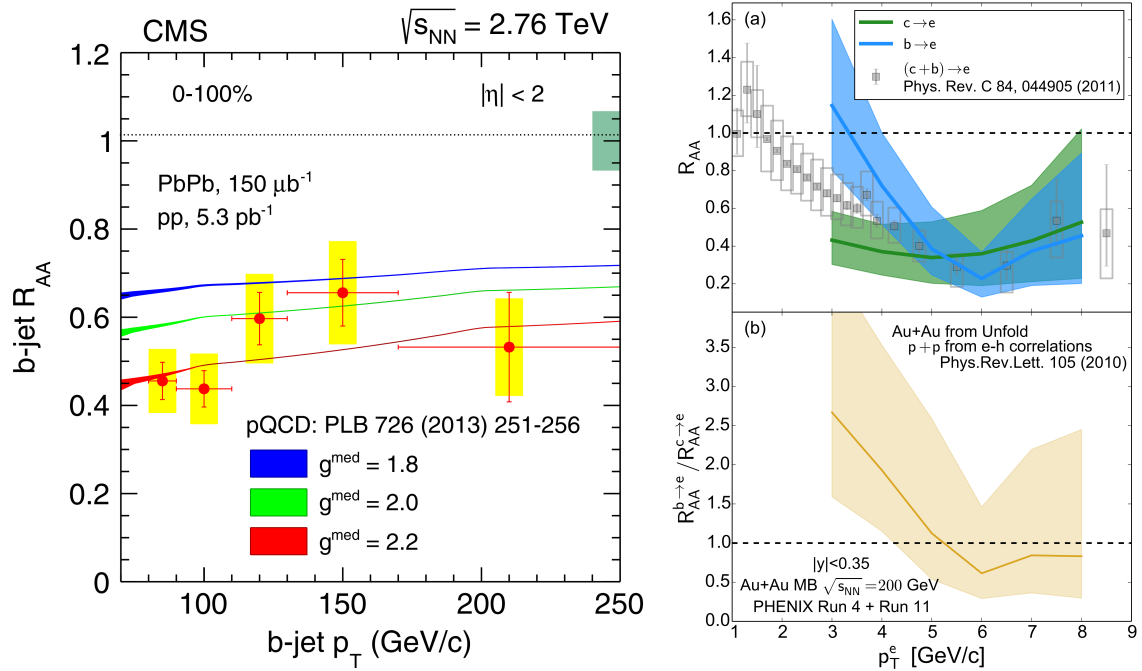


Figure 3.10: *Left:* Measurement of beauty-jets in Pb–Pb collisions at $\sqrt{s_{NN}} = 2.76$ TeV [71]. *Right:* Nuclear modification factor for electrons from beauty-hadron decays for Au–Au collisions at $\sqrt{s_{NN}} = 0.2$ TeV [72].

beauty [72]. The nuclear modification factor for the beauty case increases towards lower transverse momenta, reaching unity for the central value at 3 GeV/c, while showing a significant suppression for higher p_T . The measurement is based on a similar approach as the analysis presented in this work, using template fits of the impact parameter distribution. Chapter 10 contains a brief discussion of the differences in the methods and the implications for future measurements.

The influence of the mass difference of the quarks decreases with the energy of the quarks. For measurements at high p_T , beauty quarks can be expected to qualitatively behave more similar to charm quarks and even to the light flavors at very high p_T . The low p_T -region is particularly useful for the understanding of the mass dependence of the energy loss and the disentanglement of the mechanisms of interaction with the medium. An interesting question is whether beauty quarks at low momenta may thermalize. This suggests the measurement of beauty hadrons at low transverse momenta in central Pb–Pb collisions. The first such measurement is presented in this work.

Chapter 4

ALICE

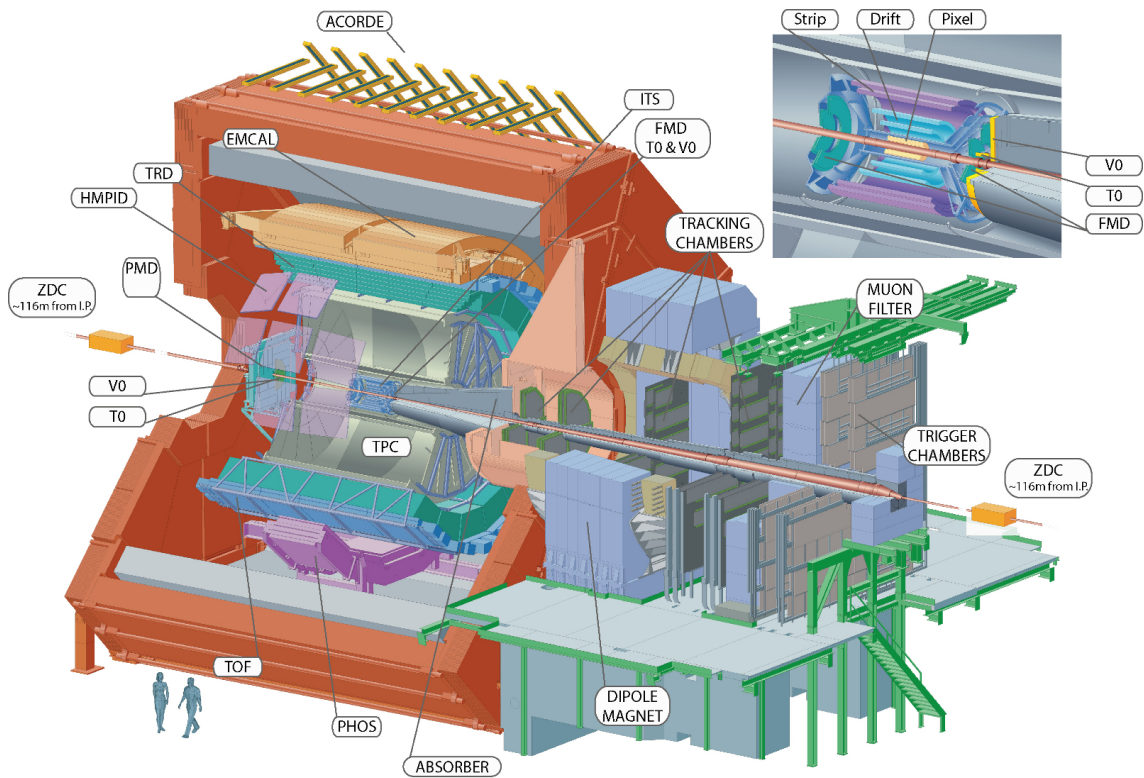


Figure 4.1: Schematic of the ALICE detector setup.

Among the different experiments built at the interaction points of the LHC, ALICE was designed to be particularly well suited for the measurement of heavy-ion collisions. This purpose requires the ability to deal with large particle multiplicities in individual collisions, measurements at low transverse momenta in the central rapidity region and strong particle identification capabilities.

Figure 4.1 shows a schematic overview of ALICE. It broadly consists of three parts: A central barrel region for the measurement at mid-rapidity, forward detectors for triggering,

centrality and event plane determination and background rejection and a muon arm. The latter is used to detect muons, which make up most of the particles that survive interaction with the large amount of absorber material ($\approx 10\lambda_{\text{int}}$) separating it from the interaction point. It covers the pseudorapidity range $-4 < \eta < -2.5$. Given the mid-rapidity measurement that is the central theme of this work, the focus of this chapter will be on detectors particularly relevant to this analysis. A more thorough overview of the systems may be found in [73].

The so-called central-barrel detectors are placed within the solenoidal L3 magnet. It provides a magnetic field of 0.5 T parallel to the beam axis, which is used to determine the transverse momentum of charged particles. The track reconstruction algorithm is based on the Kalman filter technique [74], combining signals from the different detectors. In the following the properties of detectors particularly important for this analysis will be discussed broadly moving from the beam-pipe radially outward.

4.1 The V0 detectors

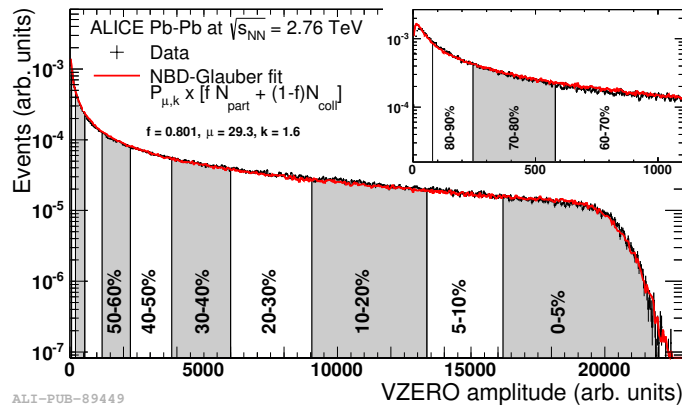


Figure 4.2: Centrality determination with the V0 detector [28].

The V0 detector consists of two subsystems called V0A and V0C [75]. They are scintillator arrays on either side of the interaction point at the pseudorapidities $-3.7 < \eta < -1.7$ and $2.8 < \eta < -5.1$. These detectors are used in the centrality determination [28]. For this purpose, the assumption is made that the particle production in the collision has both a contribution from the number of nucleon participants N_{part} and from the number of binary collisions N_{coll} . The ratio of the contributions is then fitted by applying the Glauber model discussed in chapter 2.2.1. The resulting model can be used to define the different centrality classes.

4.2 Inner Tracking System

The Inner Tracking System (ITS) [76] is responsible for the tracking of charged particles at mid-rapidity close to the interaction vertex. This ability is particularly useful for the determination of the interaction vertex as well as the vertices of secondary decays. For the analysis presented here, this is relevant for two main reasons: The signal electrons typically do not originate from the interaction vertex itself and thus have to be distinguished. Additionally, many background sources are produced some length away from the interaction vertex and this needs to be measured. This requires a detector that is placed close to the interaction vertex but which also has sufficient granularity to distinguish the large number of charged particles produced in central Pb–Pb collisions.

The detector consists of six cylindrical layers of silicon-based detectors with a pseudorapidity coverage of $|\eta| < 0.9$ for the full detector. Since this coverage is reached only for particles from an origin within 10.6 cm of the interaction vertex along the beam axis (about the extent of the 'interaction diamond' in the beam pipe), a requirement of a primary interaction vertex within 10 cm of the nominal detector center is usually applied on the analyzed events.

Three different technologies for the design of the detector layers have been used to address the specific challenges at the different distances to the primary vertex. The innermost two layers are made of Silicon Pixel Detectors (SPD), which achieve the high granularity required due to the large track density. The SPD consists of 10 sectors which are mounted around the beam-pipe and overlap at the edges. The inner layer of the detector has a distance of about 4 cm to the beam-axis, while it is about 7 cm for the outer one. The individual pixels measure $50 \mu\text{m}$ in the $r\phi$ -direction and $300 \mu\text{m}$ in the z -direction, which gives both the required spatial resolution and a good signal-to-noise ratio [76].

The technology of the Silicon Drift Detectors (SDD) uses time information to reconstruct the full 2D spatial information. After electron-hole pairs are created in by a charged particle, the electrons drift through the detector and the peak of their distribution in time allows for reconstruction of the origin. While the inner four layers have a true two-dimensional resolution, this is achieved indirectly for the two layers of Silicon Strip Detectors (SSD) connecting the ITS to the TPC. Each of these consists of two layers of silicon strips, overlapping at an angle of 35 mrad. A comparison of these allows for the two-dimensional reconstruction of the signal induced by charged particles.

In the following, the different layers will always be referred to as ITS layers. The importance for the analysis in particular of the two innermost layers necessitates a thor-

ough understanding of the detector and in particular of its description in the simulations. The low radiation length of about 7.2% [77] (for tracks perpendicular to the beam-axis) nevertheless needs to be taken into account as it produces background electrons from the conversions of photons in the detector material in addition to the material from the beam-pipe. This will be further explored in chapters 6 and 7. The ITS also provides some particle identification. Due to the low separation of the electrons from pions, which make up the main background of the analysis, this was not used in the analysis described here.

4.3 TPC

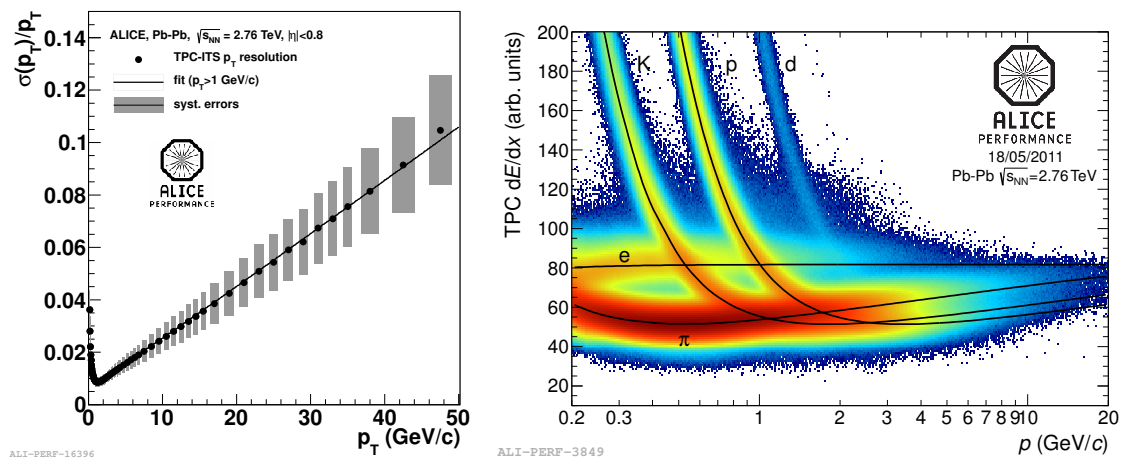


Figure 4.3: *Left:* Transverse momentum resolution of the central barrel tracking. *Right:* Particle identification signal of the TPC in Pb–Pb collisions.

Together with the ITS, the Time Projection Chamber (TPC) [78] is the main tracking device for charged particles in the central barrel. In addition it also provides strong particle identification information. The TPC is a cylindrical gas detector with length and diameter of about 5 m. The principle of operation is based on the ionization of the gas by charged particles. A homogeneous electric field parallel to the beam-axis lets the produced electrons drift towards the read-out modules on the end-plates of the detector. For this purpose, the detector is divided by a central electrode. Additionally, it is divided into an inner and outer part, containing three different sizes of readout pads [78]. Within the readout pads of the same radius, signals that are nearby in space and time are combined into clusters. The requirements for clusters used for tracking and particle identification are slightly different [79]. For this reason, they will be distinguished by using the terms **tracking clusters** and **PID clusters** respectively in this work. The

combined signals of the ITS and TPC lead to a relative momentum resolution of a few percent in the measured region as shown in figure 4.3 (left).

For each reconstructed track the PID clusters represent estimates of the track energy loss along the associated track length. To combine these signals into a single signal value, the simple use of the arithmetic mean discards all spacial information. The resulting signal distribution resembles a Landau distribution [80, 81], which does not provide a good separation of the different particle species. Instead, a truncated mean is used. For this purpose, the mean is taken of the 60% of clusters with the lowest deposited charge only. As a result the large tail of the Landau distribution is strongly reduced and for a fixed transverse momentum resembles a Gaussian distribution. The distribution of this straggling function will be discussed in more detail in section 6.2.4. The TPC signal (often abbreviated as dE/dx) after the application of the truncated mean may be found in figure 4.3 (right).

To simplify the selection or rejection of a particular signal, it has proven useful to calculate how significantly the signal deviates from a particular particle identity hypothesis:

$$n_{\sigma, \text{TPC}} = \frac{(dE/dx)_{\text{measured}} - (dE/dx)_{\text{expected}}}{\sigma_{(dE/dx)}}, \quad (4.1)$$

where the expected signal and the expected resolution are calculated individually for each track. The same definition also applies for other detectors. Within this work, the $n_{\sigma, \text{TPC}}$ will always be used with an electron (or positron) hypothesis unless explicitly stated otherwise.

4.4 TRD

The Transition Radiation Detector (TRD) can provide additional particle identification. The signal combines the ionization of the detector gas by charged particles with additional ionization from transition radiation produced in the radiator before the gas volumes. It consists of 6 layers of detectors in radial distribution. Due to the limited acceptance of the detector in the data taking period used for this work (10/18 sectors available), it was used only for supplemental analysis estimating the hadron contamination as discussed in section 6.3.

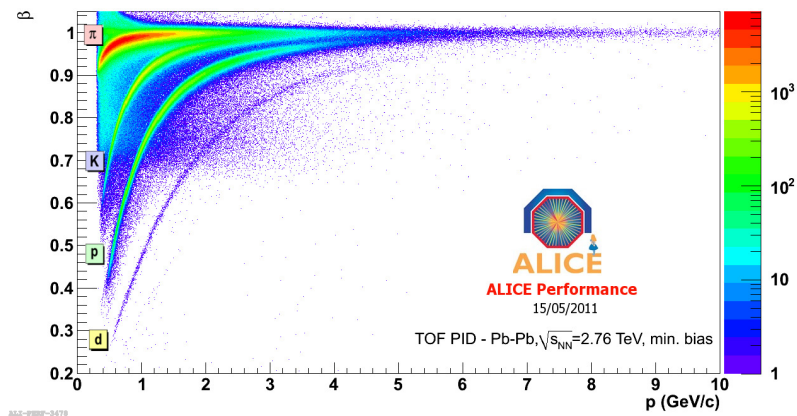


Figure 4.4: Velocity measurement of particles based on the time-of-flight information. The electrons are hidden within the signal distribution of the pions.

4.5 TOF

The Time-of-Flight detector (TOF) is an array of multigap resistive plate chambers [75, 82]. It compares the arrival times of particles with an estimated time for the event calculated by comparing different mass hypotheses for the particles of the event [73]. Thus, it can particularly distinguish particles with large mass differences as shown in figure 4.4. In this way, it provides complementary information to the gas detectors, in particular where the signal distributions of deuterons and protons cross that of the electrons as shown in figure 4.3 (right).

4.6 Data set and detector simulations

The data set on which this analysis is based was recorded in 2010 at the LHC with a center of mass energy per nucleon of $\sqrt{s_{NN}} = 2.76$ TeV. Due to the large number of produced particles, the minimum bias trigger based on coincident signals in the V0 and SPD [73] detectors was fully efficient for the 0-20% centrality range discussed here. Within the 2010 Pb-Pb data taking period, two configurations of the magnetic field (0.5 T) were used, which will be referred to as the positive and negative field configuration and associated with the numbers +1 and -1. This determines the direction of the bending of charged particle tracks in the field which will be relevant for the estimation of the background due to electrons from photon conversions in the detector material as described in section 7.1. The data set contains about 3.3M events in the 0-20% centrality range.

A central technique of the analysis is the use of simulated data in conjunction with

measurements to understand the response of the detectors to different inputs. The combination of event and detector simulations used for this purpose will be referred to as **Monte Carlo simulations**. All sets of simulated data used in this work are based on the GEANT3 detector simulation package [83]. The simulations are anchored to the conditions of the different data taking periods to represent the time dependence of the detector response. Two different setups for the event generation were used: The HIJING v1.36 event generator [84] creates events which represent the minimum bias collisions. This set of simulated events will be referred to as the **minimum bias Monte Carlo sample**. Due to the rarity of the beauty and charm hadrons the information from it about these particles has large statistical uncertainties. For this reason, a second sample was used, which adds heavy flavour signals to the sample. In addition to the HIJING event, a signal is added randomly based on the PYTHIA v6.4.21 event generator [85] with the PERUGIA-0 tune [86]. The additional signals are randomly selected from a list of heavy flavor signals, containing hadronic and semielectronic decays of charm or beauty particles as well as J/ψ particles decaying to electrons. This set of simulated events with added heavy flavor signals will be referred to as the **signal-enhanced Monte Carlo sample**. In order not to be influenced by the additional J/ψ particles, these are discarded for the analysis. Due to the large particle multiplicities in central events, their general properties do not change strongly with the addition of one heavy-flavor signal.

Chapter 5

Analysis strategy

The beauty quarks cannot be directly measured due to confinement. At high transverse momenta, jet measurements can give some insight into the quark kinematics, but at low p_T the connection has to be made indirectly via the resulting beauty hadrons. The connection to the quarks is then made via theoretical calculations as discussed in chapter 3. The large statistics required prevent direct reconstruction of the beauty hadrons via their purely hadronic decays (e.g. $B^+ \rightarrow \bar{D}^0 \pi^+$, $\bar{D}^0 \rightarrow K^+ \pi^-$), although this will become possible for some hadron species after the planned upgrade of the ALICE detector [87]. The approach of this work is based on the measurements of electrons from semileptonic decays of the beauty hadrons.

The measurement of electrons has the advantage that it can make use of the excellent particle identification capabilities of the ALICE detector (as described in the previous chapter). The electrons can either stem directly from the decay of the hadron (denoted by $b \rightarrow e$) or from the decay to a charm hadron which decays semileptonically. Both processes have a branching ratio of about 10% [11], giving a total of about 0.205 with little dependence on the hadron species. For both cases, the electrons will be referred to as **beauty-hadron decay electrons**. As a result, electrons above a few GeV/c mostly come from the decay of charm or beauty hadrons [88].

To connect the kinematic properties of the beauty hadrons to those of their decay electrons it is necessary to consider their decays. These are included in the Monte Carlo simulations [85]. Figure 5.1 (left) shows the probability distribution of the $p_{T,e}$ of the electrons for a given $p_{T,mother}$ of the mother beauty hadron. Most electrons are produced below 1-2 GeV/c, independent of the transverse momentum of the mother particle. The distribution $P(p_{T,e}|p_{T,mother})$ widens towards larger $p_{T,mother}$. While it seems like the connection between the electron and hadron momenta is weak, this is actually not the case. This becomes obvious when asking for the distribution of momenta

Hadron	Decay mode	B.R./Multiplicity	Mass (GeV/ c^2)	$c\tau$ (μm)
B^\pm	$l^+ \nu_l$ anything	0.11	5.28	491.1
	$c/\bar{c} X$	1.19		
B^0	$l^+ \nu_l$ anything	0.10	5.28	455.7
	$c/\bar{c} X$	1.19		
Λ_b^0	$\Lambda_c^+ l^- \nu_l$ anything	0.11	5.62	439.5
D^\pm	e^+ semileptonic	0.16	1.87	311.8
D^0	e^+ anything	0.065	1.86	122.9
Λ_c^+	e^+ anything	0.045	2.29	59.9

Table 5.1: Properties of selected open heavy flavor hadrons [11].

of the mother beauty hadrons for a given electron $P(p_{T,\text{mother}}|p_{T,e})$, which is shown on the right side of figure 5.1. While $P(p_{T,e}|p_{T,\text{mother}})$ depends mainly on the decay characteristics, the distribution of $P(p_{T,\text{mother}}|p_{T,e})$ also has some dependence on the hadron spectrum in the simulation, which can be made explicit using Bayes' theorem ($P(p_{T,\text{mother}}|p_{T,e}) \sim P(p_{T,e}|p_{T,\text{mother}}) P(p_{T,\text{mother}})$). Nevertheless, the distribution from the signal-enhanced Monte Carlo simulations, which are similar to the measured pp case, can give some general insight. The result shows, that for a fixed electron p_T , the mother particle typically comes from a p_T -range near the lower edge of allowed values.

Knowing that a measurement of the p_T -differential yield of the electrons provides substantial information about the beauty hadrons raises the question whether it is possible to directly calculate the p_T -distribution of the beauty hadrons. The tools for such a calculation will be discussed in chapter 8. Two results are important: The distribution $P(p_{T,e}|p_{T,\text{mother}})$ in figure 5.1 (left) propagates the p_T -distribution of the hadrons to that of the electrons, thus its inverse can be used for the other direction. If the correlation between the two variables is not strong, this will typically introduce strong correlations between the different regions in p_T -space, which result in large uncertainties for the individual points. If only a finite p_T -range is measured, this introduces additional uncertainties in the final result. The application of ad-hoc additional information like regularization terms can smooth the result but leads to a bias of the measurement that is difficult to estimate. Instead, propagating the theoretical predictions for the beauty hadrons to those of the beauty-hadron decay electrons can be done in a straightforward

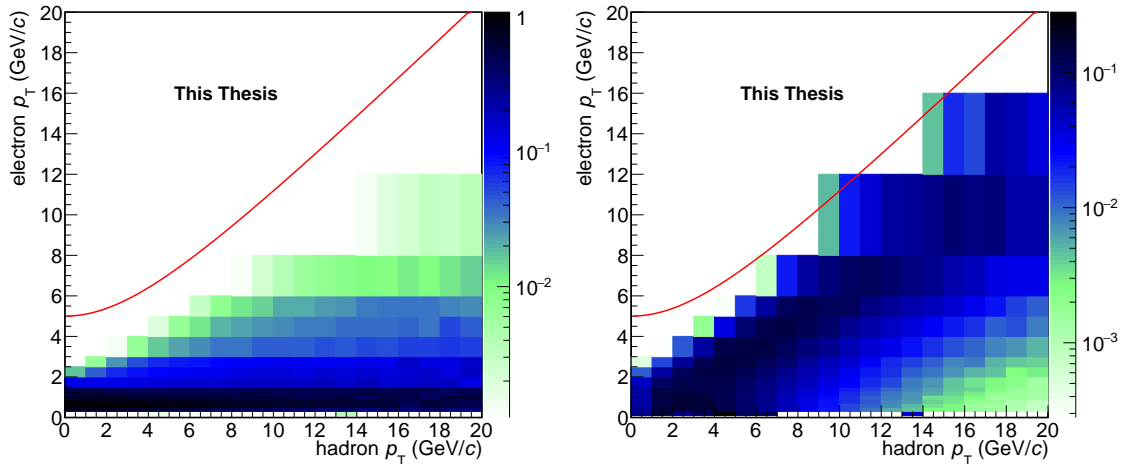


Figure 5.1: p_T -distributions of beauty hadrons and the daughter electrons in Monte Carlo Simulations. *Left*: For a given hadron p_T . *Right*: For a given electron p_T . The line shows the electron p_T assuming it receives all energy of the mother particle.

manner via $P(p_{T,e}|p_{T,mother})$. For this reason, it is prudent to make the comparison between theory and measurement on the level of the electrons. This will be the approach for the work presented here.

To get an insight into the dependence of the yield on the transverse momentum, the measurement was performed within distinct regions of p_T . For the remainder of this thesis, they will usually be referred to as p_T -bins. The transverse momentum is measured based on the bending of the tracks in the magnetic field of the L3 magnet. Due to the uncertainty of this measurement, it is important to clarify the use of p_T in this context. The p_T -bins used for the most part will be bins of the measured p_T , while the result should finally be presented in a distribution of the true p_T . The connection between the two will be described in chapter 8. Until then, ' p_T ' will always refer to the measured value as given from a reconstruction of the detector signals.

The estimation of the yield of beauty electrons in a particular p_T -bin can be split into two parts. In a first step electrons are selected by choosing suitable quality criteria for the tracks and by using the PID capabilities of the detectors. This yields a sample of electron candidates with some remaining contamination by other particles. With a knowledge of the efficiency of the selection $\epsilon_{\text{selection}}$, the central values for the p_T -differential yield can be calculated as

$$\frac{dN_{\text{corrected}}^{b \rightarrow e}(p_T)}{dp_T} = \frac{1}{\epsilon_{\text{selection}}(p_T)} \frac{dN_{\text{raw}}^{b \rightarrow e}(p_T)}{dp_T}. \quad (5.1)$$

This efficiency correction has an associated uncertainty due to the estimation of the

efficiency. The selection itself was applied using a set of independent requirements for the different detectors. An advantage of this approach is the clear separation of the contributions from the different detectors, which allows for a more thorough estimate of the associated uncertainties.

The second step is the estimation of the fraction of beauty-hadron decay electrons in the sample. Two properties of beauty hadrons seem particularly useful: They have a high mass (typically $5\text{-}6 \text{ GeV}/c^2$) and they decay weakly, which gives them a sizeable decay length (typically $400\text{-}500 \mu\text{m}$). Both properties do not seem easily applicable to the single electron measurement as single particles allow neither for the measurement of an invariant mass nor that of the decay length of a secondary vertex. Nevertheless, it is possible to make use of both. In the low-background environment of pp collisions it is possible to make use of the large mass of beauty hadrons by measuring the angular correlations of electrons. The typical angles between the decay products are wider for beauty hadrons than for those from charm, which gives some information for the separation of their contributions [6]. For the large background in Pb–Pb collisions, the large decay length was used to separate the different electron contributions, albeit indirectly.

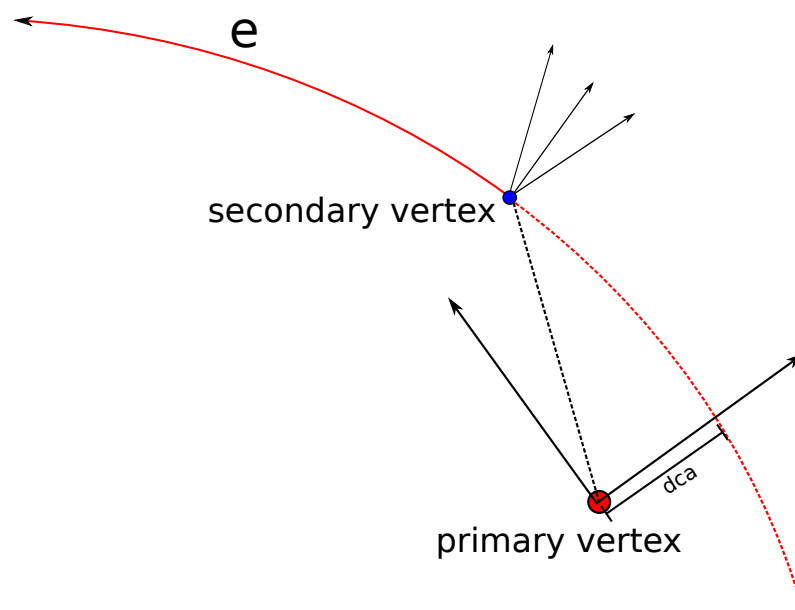


Figure 5.2: Impact parameter definition

When a beauty hadron decays some distance away from the primary vertex, the daughter electron will typically be emitted at an angle relative to the mother particle's momentum vector. If the electron track is measured precisely and compared to the measurement of the position of the primary vertex, they will typically be incompatible.

This is the fundamental idea for the separation of the fraction of electrons from beauty-hadrons decays. It can be made more precise, by considering the plane perpendicular to the beam axis which contains the primary vertex of a collision. An example of the projection of an electron track on this plane is shown in figure 5.2. A measure for how incompatible a track is with the hypothesis that it comes from the primary vertex is the distance of closest approach (dca) or impact parameter. To measure it, the track is propagated back from the measured points in the detectors towards the primary vertex. The smallest distance of the track depends strongly on the decay length of the mother particle.

It has proven useful to assign a sign to the value of the dca. Often, it is assigned as positive or negative depending on whether the track passes the primary vertex on its left or right side. For the analysis in this work, a different definition was more suited: The original (signed) value was additionally multiplied by the field configuration (+1 for positive, -1 for negative field) and the sign of the charge of the particle (positron or electron). This increases the separation power of the variable as will be shown in section 7. The resulting variable will be referred to simply as the **impact parameter** in the following.

The measured value of the impact parameter depends on the decay radius (and thus the decay length of the mother particle), the angle of the daughter particle with respect to the momentum vector of the mother, the magnetic field (which bends the track towards or away from the primary vertex), the resolution of the tracking close to the primary vertex and the resolution of the primary vertex itself. In the high multiplicity Pb–Pb collisions, the primary vertex resolution is very high compared to the proton-proton case [73].

The analysis thus consists of three steps: Identification of a sample of electrons for different p_T -ranges, estimation of the fraction of electrons from the decay of beauty hadrons and a correction for the measurement uncertainty of the transverse momentum. The electron identification consists of separate requirements of detector signal ranges, while the signal extraction is performed using the impact parameter.

Chapter 6

Track selection and particle identification

6.1 Introduction

Tracks measured by the detector show variations in the associated signals due to both statistical fluctuations of the signal and dependencies of the detector signal on the position of the track in the detector setup. The analysis is simplified by the choice of a sample of particles with requirements for the track quality, leading to a more uniform detector response. Additionally, the detector signals are required to be consistent with the hypothesis that the particles are electrons. The choice for these track quality and particle identification requirements has a certain efficiency, which was estimated mostly based on the Monte Carlo simulations of the events and detectors. This efficiency also has an associated uncertainty. Given the close connection between the selection criteria, their efficiencies and the associated uncertainties, they will be discussed together in this chapter. The selection criteria should provide a good impact parameter resolution, a low remaining hadronic background and a high efficiency while also allowing for an accurate estimate of the associated uncertainties. The implications for the individual detectors will be discussed in the following.

The ITS is particularly important for the measurement of the impact parameter because it is closest to the interaction point. Each track can have a reconstructed signal in each of the six layers. To ensure a good resolution of the impact parameter, the track was required to have an associated signal in the two innermost layers (the SPD) and at least four layers in total. Apart from the impact parameter resolution, this also reduces the background of electrons from photon conversions in the detector material,

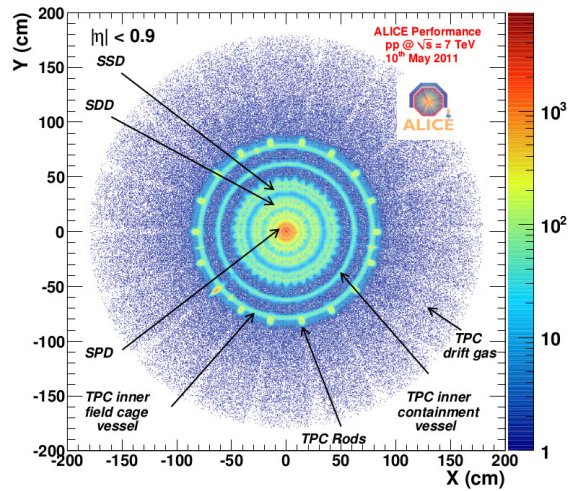


Figure 6.1: Reconstructed vertices of photon conversions in the detector.

which is important for the signal extraction. Figure 6.1 shows the production vertices of electron-positron pairs in the inner part of the detector. The requirement of a signal in the innermost two layers of the ITS removes most of the conversion electrons that are produced outside of the innermost layer, which has two advantages: The total number of such background electrons is reduced. Additionally, the remaining electrons are produced close to the primary vertex. This results in an impact parameter distribution that is more favorable for the signal extraction. It will be discussed in more detail in sections 7.1 and 7.3.2.

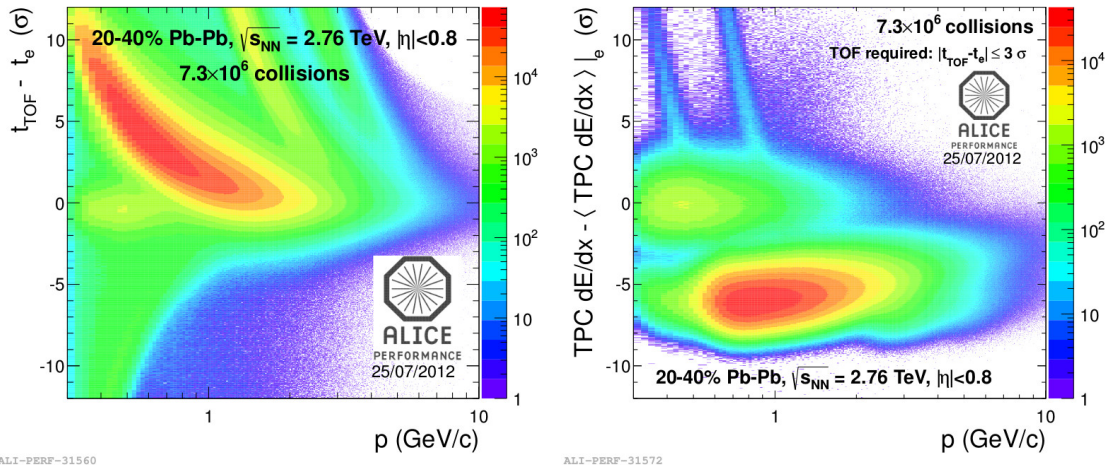


Figure 6.2: $n_{\sigma,TOF}$ -distribution (left) and $n_{\sigma,TPC}$ -distribution after application the TOF signal requirements (right).

For the TPC, the number of clusters is strongly correlated with the quality of the

energy loss measurement. Due to the typically larger energy deposit, the number of clusters is larger for electrons than for most hadrons. Requiring a large number of clusters improves both the resolution of the detector as well as making the modeling of the signal easier. As a result, the hadron contamination is lower and the estimate of the efficiency is better, leading to a lower uncertainty. For this purpose, 110 tracking clusters and 80 PID clusters were required in addition to a tracking χ^2 below 4, resulting in an efficiency of 90 – 95%. The distribution of the PID signal (plotted as $n_{\sigma, \text{TPC}}$ in figure 6.2, right) shows that the main background has a lower value, motivating an asymmetric selection. The PID selection criterion was chosen to be $-0.5 < n_{\sigma, \text{TPC}} < 3$. The efficiency of about 70% does not vary quickly with (transverse) momentum. As a result, the efficiency within a p_T -bin is less dependent on the slope of the spectrum, which increases the accuracy of the efficiency determination and its uncertainty.

For the TOF, no additional track quality requirements were added besides the existence of a PID signal. A selection on the particles time-of-flight does not reduce the primary background from the pions very well due to the pions' small mass. It serves mainly to decrease the contamination from protons and deuterons, which have a peak that is well separated in the places where they cross the electrons in the TPC signal as shown in figure 6.2. For this reason, a loose requirement of $-3 < n_{\sigma, \text{TOF}} < 3$ is sufficient.

6.2 Estimation of the efficiencies and associated uncertainties

The track selection criteria remove a significant amount of measured tracks from the pool of electron candidates. To take this into account, it is important to estimate both the efficiency of this selection as well as its associated uncertainty. An estimate of the efficiency can be obtained from Monte Carlo simulations, which was done for all steps except the TPC PID selection. Given the large statistics of the simulations with regard to this task, the uncertainty associated with this correction comes from the accuracy of the representation of the efficiency in the simulation, which mostly means the representation of the detector responses. The simulations can give little information about their own accuracy, which means that it has to be determined by comparison to data as far as this is possible. In this regard, it is useful to divide the total efficiency into contributions from the individual track selection requirements. The efficiency for a particular track selection criterion depends mostly on the representation of the relevant detector but also to some extent on the interplay between the different detectors.

To define the electron candidate sample, the order in which the individual criteria are applied is arbitrary and does not influence the total efficiency. It also should not affect its uncertainty. However, to define the efficiency of one particular selection criterion (or a set of such) it does make a difference. In general, the choice of the particle sample on which a selection criterion is applied changes its efficiency. Typically, having some previous requirements applied (even for other detectors), biases the sample towards higher quality tracks and yields a higher efficiency for a subsequent one than if this one had been applied first. Let c_i represent the selection criterion i and $\varepsilon(c_i|c_j)$ be the efficiency of the requirement of a criterion c_i on a sample where c_j has already been applied. The total efficiency can then be written as

$$\varepsilon(c_1, c_2, \dots, c_n) = \varepsilon(c_n|c_1, \dots, c_{n-1})\varepsilon(c_{n-1}|c_1, \dots, c_{n-2}) \dots \varepsilon(c_2|c_1)\varepsilon(c_1) . \quad (6.1)$$

While this is true for any permutation of the c_n , the individual factors can change significantly. This means, that to estimate the systematic uncertainty of a track selection criterion it is important to also specify the sample it is applied on. For example, the efficiency of the TPC PID signal requirement of $-0.5 < n_{\sigma, \text{TPC}} < 3$ is only meaningful if it is known whether the PID cluster requirement is already in effect as this changes the shape of the straggling function.

The order of the different criteria being arbitrary, it can be used to simplify the estimation of the systematic uncertainties. The choice is given here, while its justification will become apparent later, in the discussion of the individual efficiencies.

1. A requirement for a reconstructed track in the ITS and TPC: Signal in at least two layers of the ITS and at least 30 tracking clusters in the TPC (ε_{rec})
2. Signal in the first two layers of the ITS, and in least 4 layers total (ε_{ITS})
3. At least 110 tracking clusters in the TPC, at least 80 PID clusters and $\chi_{\text{TPC}}^2 < 4$ ($\varepsilon_{\text{TPC-Quality}}$)
4. A reconstructed track in TOF with $|n_{\sigma, \text{TOF}}| < 3$ (ε_{TOF})
5. A TPC PID signal with $-0.5 < n_{\sigma, \text{TPC}} < 3$ ($\varepsilon_{\text{TPC-PID}}$)

Figure 6.3 shows the cumulative efficiencies up to a given step. The efficiency is estimated by comparing the number electrons in the range $|\eta| < 0.8$ before and after the selection in the signal-enhanced Monte Carlo simulations. To make the sample more representative of the properties of electrons from beauty-hadron decays, only electrons produced within 0.5 cm of the reconstructed interaction vertex were chosen for the

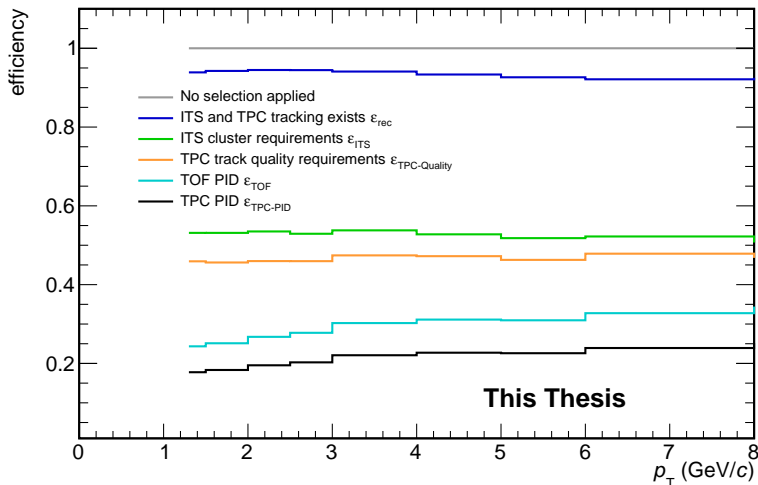


Figure 6.3: Cumulative efficiencies of the different selection steps.

determination of the efficiency. The determination of the TPC PID selection efficiency was fully data-based and will be discussed in detail in section 6.2.4. Due to the large samples, statistical fluctuations are small.

The accuracy of this estimate is given by the difference of the efficiency between data and Monte Carlo simulations. However, the efficiency in data is difficult to ascertain. For this reason, an indirect approach is necessary to estimate a possible difference between the true efficiency and the one given by the simulations. The approach used in this analysis may be summarized as follows: The first step is to identify the physical processes that determine the efficiency. With this knowledge, a sample of particles can then be chosen that is affected similarly, but which can also be selected in data. For such a **proxy sample** of particles, the efficiency is determined in data and in the simulations. A difference in the efficiency of the proxy sample points to a similar difference in efficiency also for the beauty-hadron decay electrons and is thus used to estimate the systematic uncertainty. In the following sections, this process will be described for the different categories of selection criteria.

For the purpose of comparing data and simulations, the V0 samples are of central importance. These are samples of particles, that are produced in the decay of neutral mother particles and which can be selected using their decay topology. The selection process is described in more detail in [89]. In particular, the decays $\Lambda \rightarrow p^- \pi^+$, $K_S^0 \rightarrow \pi^+ \pi^-$ and $\gamma \rightarrow e^+ e^-$ (in the detector material) are considered as well as the processes with the respective antiparticles. This results in samples of protons, pions and electrons

of which the latter two are of interest for this analysis. In the following, the sample of electrons (and positrons) selected in this manner will be referred to as the **V0 electrons**, while the sample of charged pions will be referred to as the **V0 pions** for brevity.

It is not possible to perform such an analysis without at least basic tracking information. The starting point for the analysis were the requirements of a signal in at least two of the ITS layers and at least 30 tracking clusters in the TPC, which leads to an efficiency of about 94%. The uncertainty should be similar to the 3% estimated in e.g. [90] by comparing all reconstructed tracks with those reconstructed in the TPC.

6.2.1 ITS selection criteria

The efficiency of the requirement of the ITS hits depends mainly on dead areas in the detector. A charged particle with a given production vertex, direction and momentum will usually produce a signal in all active detector elements it traverses. If however, one or several dead detector areas are traversed, the selection criteria might not be met. This is mostly independent of the particle species, meaning that the efficiency is for the most part determined by geometric effects. Therefore unidentified charged particles can be used as the proxy sample for the estimation of the systematic uncertainties. The efficiency of the ITS selection criteria should be similar for charged particles and for electrons. A possible difference between the two samples might be the hadronic interaction of charged hadrons with the detector material, which does not occur for electrons. For this reason, the comparison is based on a geometric approach, alleviating such difficulties.

Figure 6.4 shows the distribution of primary charged particles that fulfill the ITS signal requirements in $\eta - \phi$ -space. The generated distribution can be expected to be flat in the polar angle ϕ when averaging over many collisions and particles. There is no such symmetry in the η -direction. Accordingly, the distribution was corrected for this by normalizing with the η -distribution of tracks without the ITS requirements. This omits some effects such as the creation of secondary particles, but still gives a representative sample for the purpose of an estimation of the systematic uncertainty. It is apparent from the figure that the $\eta - \phi$ -distribution mostly contains regions of high efficiency and regions of very low efficiency. If these regions are normalized to represent full efficiency, then the diagrams of figure 6.4 would represent the local efficiency in the $\eta - \phi$ -space. To achieve this, a region of high efficiency is chosen (represented by the red box) and used for normalization. A proxy for the efficiency is now the average over the whole $\eta - \phi$ -space. The result of 60.2% for the Monte Carlo simulations is very close to the

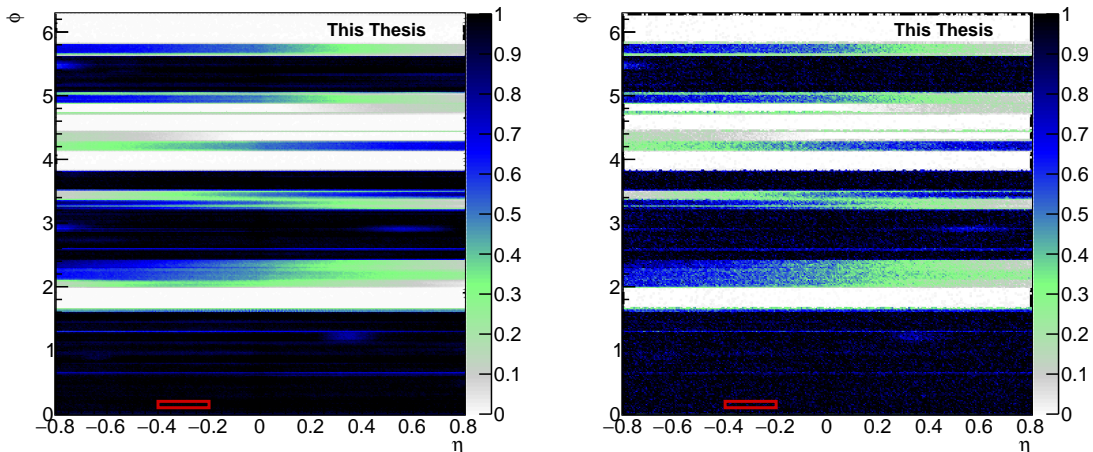


Figure 6.4: Distribution of primary charged particles in η and ϕ for the p_T -range 1.5–2 GeV/c for data (*left*) and in Monte Carlo simulations (*right*), corrected for the η -distribution of charged particles. One set of normalization regions is shown.

efficiency of 57% used for the correction. This supports the basic assumption that the proxy sample is representative.

The proxy efficiency defined in this way differs slightly between data and the simulations (59.2% vs. 60.2%). To make sure this result is not dependent on the exact point of the normalization region, the procedure was repeated for different regions and in different (transverse) momentum bins. The result was qualitatively similar. This means, that the efficiency of the ITS track quality requirements is represented within 2% by the Monte Carlo simulations for this case.

6.2.2 TPC quality requirements

The second set of selection criteria concerns the tracking quality in the TPC. It mainly concerns the number of clusters associated with a track. The ionization of the gas depends significantly on the $\beta\gamma$ of the particle. Additionally, the track length in the detector depends on the transverse momentum due to the bending of the track in the magnetic field. Both influence the number of clusters. Consequently, charged hadrons are not a representative proxy sample in this case. It is not easily possible to obtain a clean, representative sample of pure electrons while applying only the ITS requirements but it can be approximated. For this purpose, the V0 electron sample described above was used. Figure 6.5 shows the $n_{\sigma,e}^{\text{TPC}}$ -distribution of electrons selected in this way. The blue distribution shows a large peak for pions. This means, that this electron sample is

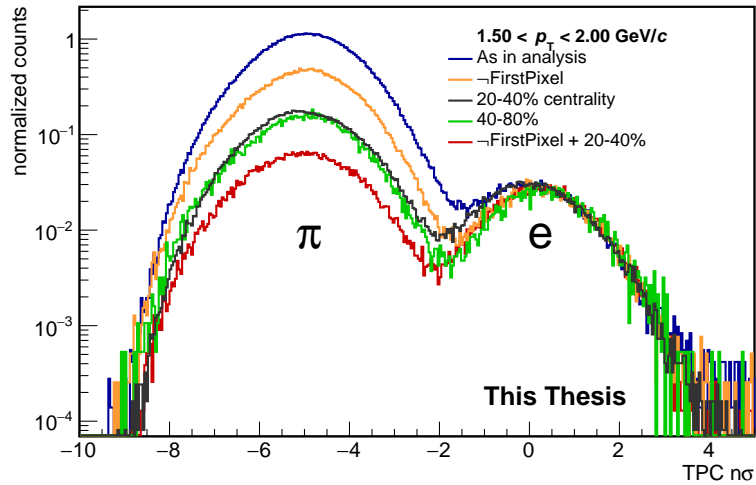


Figure 6.5: TPC signal of V0 sample. All samples were normalized to have the same area on the right side of the electron peak.

strongly contaminated by hadrons and cannot be used directly.

Due to the large contamination of the V0 sample, it is necessary to apply additional selection criteria. To ensure that the sample still represents the properties of the electrons from beauty-hadron decays, it is important to understand the reasons for this contamination as well as its properties. Selecting a similar sample in a proton-proton collision results in a much smaller contamination suggesting combinatorics as a cause: The large multiplicity of pions produces sufficient combinatorial pairs that have properties consistent with a photon conversion production process. Additionally, the requirement of a signal in the innermost layer of the ITS preferentially selects particles produced close to the interaction vertex, while most photons conversions happen at larger radii.

To generate a clean sample of electrons, TPC PID would be useful. Unfortunately, the TPC PID signal depends quite strongly on the TPC quality selection criteria: If, for example, the truncated mean of the TPC signal is calculated with fewer clusters, then the signal $n_{\sigma,e}^{\text{TPC}}$ will be more asymmetric (as discussed in chapter 4), changing the efficiency. Conversely, this means, that the sample will not be representative if the TPC PID requirement is applied. The correlation effect decreases as the efficiency of the PID requirement increases. This suggests using a weaker TPC requirement to select the sample. Additionally, also the contamination changes significantly with the application of the TPC quality requirements. The tracks with few PID clusters have a worse resolution, resulting in a $n_{\sigma,e}^{\text{TPC}}$ closer to the electron line. This effect means that contamination of

the electron sample is particularly problematic for this approach and that the TPC PID requirement should be stronger. To solve this dilemma, some additional conditions were applied to the sample.

As explained before, the reasons for the hadron contamination of the V0 sample are the large particle multiplicity and the requirement of a signal in the innermost layer of the ITS. One radical way of reducing the amount of hadron contamination is to require that all particles in the sample explicitly do *not* have a signal in the innermost layer. Due to the requirement of a hit in the second layer, this preferentially selects particles produced in the material between the first and second layer, reducing the contribution of primary particles. In turn, this can also bias the result in two ways: The change in the ITS cluster requirement changes the $\eta - \phi$ distribution of the accepted particles (as explained before), while the TPC cluster reconstruction depends to some extent on these qualities. Additionally, a track produced outside the innermost layer may in a high multiplicity environment be wrongly associated with the signal of another track in the innermost layer. This effect depends on the local track density in the $\eta - \phi$ region. Consequently, this requirement would slightly bias the tracks in the sample towards coming from regions of a lower local track density. The local track density also influences the number of PID clusters because clusters from overlapping tracks are not used for PID. Another way of decreasing the background is to directly use a sample from more peripheral collisions for this purpose. The lower track number gives fewer combinations of hadron pairs that resemble electrons from photon conversions. This approach also changes the local track multiplicity although in a different manner.

To estimate the uncertainty without being influenced too much by the biases, several different samples were created and the resulting differences in the efficiencies were compared. Figure 6.5 shows how different choices of centrality and ITS cluster requirements influence the remaining hadron contamination. For the weaker TPC signal cut, a range of $-1.5 < n_{\sigma,e}^{\text{TPC}} < 4$ was chosen. For comparison also $-0.5 < n_{\sigma,e}^{\text{TPC}} < 4$ was used for a cleaner sample with a larger bias. The comparison for the efficiency of the TPC track quality requirements between data and Monte Carlo simulations is shown in figure 6.6. Due to the quickly falling momentum distribution of the photons (e.g. figure 7.1), the statistical uncertainties quickly increase with p_T . Between one and two GeV/c, the difference in efficiency is of the order of a few percent. At higher transverse momentum, the different samples give different estimates. In particular, the sample with 0–20% centrality without the first pixel deviates. The deviation changes strongly with the TPC PID requirement, pointing to an influence of the hadron contamination. This interpretation is further supported by the fact, that the sample with the strongest additional selection

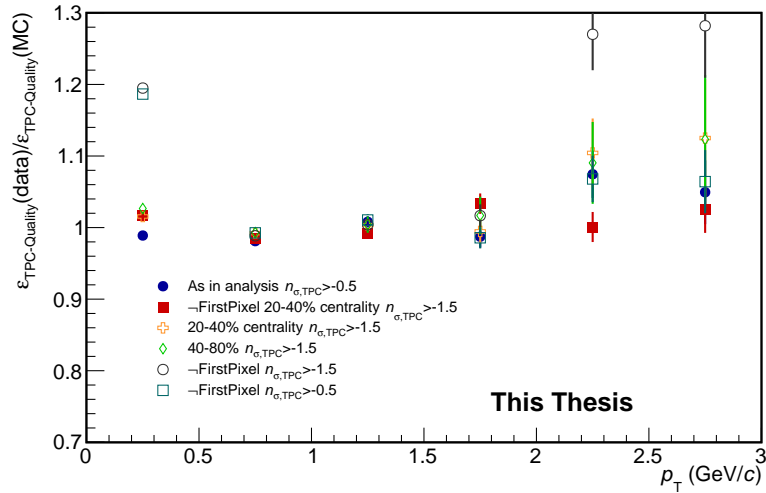


Figure 6.6: Comparison of the TPC track quality requirement efficiencies of the proxy samples in data and Monte Carlo.

criteria shows the least deviation. For this reason, only the p_T -interval $1 - 2 \text{ GeV}/c$ was used for the estimation of a systematic bias. In this region, the deviation is typically less than 3%. Thus, this number was chosen to represent the uncertainty in the determination of the efficiency of the TPC quality criteria. The large deviation below $1 \text{ GeV}/c$ is due to proton contamination. It is worth noting here, that a 3% uncertainty on an efficiency of 90% is rather large in itself. However, in this particular analysis it is not significant for the final uncertainty. Due to the small change in energy loss and track length in the TPC for electrons above $2 \text{ GeV}/c$, this uncertainty was assumed to be a reasonable estimate for the larger transverse momenta as well.

6.2.3 TOF selection criteria

For the TOF requirement, a similar approach was used. Again, it is important to use electrons for a representative signal. The efficiency of this selection is about 60%. This is dominated by the requirement of having a TOF signal associated with the track segment. The efficiency of the signal being within 3σ of the electron hypothesis ($|n_{\sigma, \text{TOF}}| < 3$) is about 95%. For simplicity, the samples were selected in the same manner as before. The additional TPC selection criteria improve the purity of the samples as shown in figure 6.7, where the improvement is most apparent in the deeper minimum between the peaks. As a consequence, this allows for a comparison at higher p_T due to the reduction of the pion contamination. On the other hand, any remaining contamination

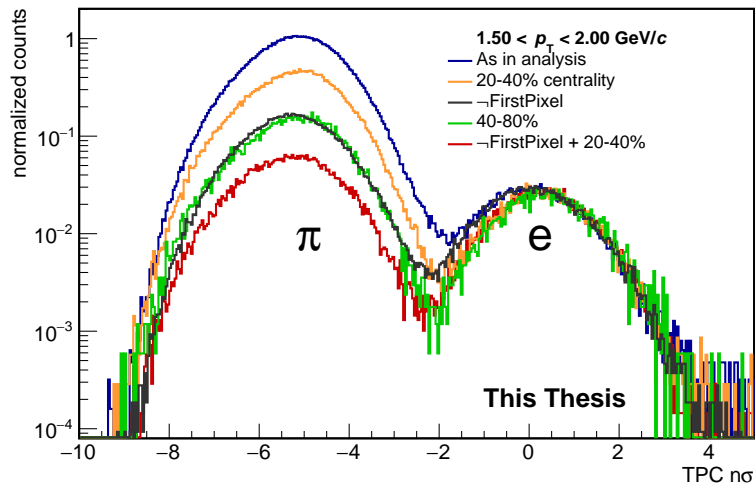


Figure 6.7: TPC signal of V0 sample after application of the TPC quality selection. All samples were normalized to have the same area on the right side of the electron peak.

by heavier hadrons will have an efficiency that is small because the velocity β and thus the TOF signal changes more strongly from electrons to e.g. protons than the TPC cluster distributions do. This results in a greater effect due to contaminating protons than in the previous section.

This effect can be seen in figure 6.8. Around $1 \text{ GeV}/c$ the protons have a similar TPC signal as the electrons (this is also shown in figure 6.2) giving rise to a large discrepancy in the efficiency estimate of the samples. On the other hand, the comparison is much easier for the higher momenta, above $1.5 \text{ GeV}/c$. There, the differences are of the order of 10% with the deviations between the samples being of the order of the expected statistical fluctuations, which are interpreted as the systematic uncertainty of the efficiency. Further analysis shows, that there is a contribution both from the tracking requirement (the existence of a TOF signal) and the PID requirement ($|n_{\sigma, \text{TOF}}| < 3$). Both contribute at a similar order and partially cancel.

6.2.4 TPC PID selection

The efforts of the previous paragraphs concern the estimate of the systematic uncertainty of the efficiencies. The values themselves originate from the Monte Carlo simulations. For the TPC PID selection, the approach was to go a step further and also estimate the efficiency of the selection criterion directly using a data-driven method. This means that where it was previously sufficient to find a representative sample giving a proxy for the

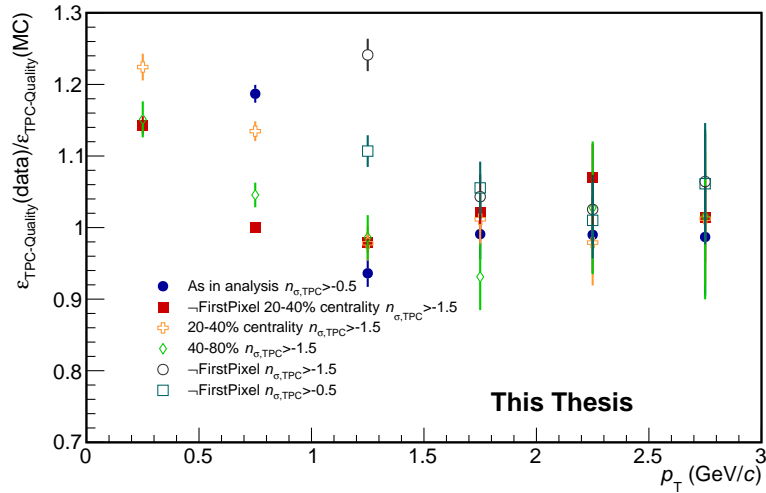


Figure 6.8: Comparison of the TOF selection efficiencies of the proxy samples in data and Monte Carlo.

efficiency it is now essential to estimate precisely how well it reproduces the efficiency. The difficulty is alleviated by the application of the previous selection steps. Once more, the V0 sample of electrons from photon conversions was used. In this case, all track selection criteria were the ones from the analysis to avoid introducing a bias to the estimation. On the other hand, the use of the V0 sample itself already introduces a bias which has to be corrected for.

Figure 6.9 shows the $n_{\sigma,e}^{\text{TPC}}$ -distribution for electrons from the V0 sample in black. The sample is dominated by hadrons (mostly charged pions). In contrast to the previous estimates, it is obviously not possible to apply TPC PID to estimate the efficiency of the TPC PID. For an estimate of the efficiency, it is necessary to add significant additional information. This in turn requires a thorough understanding of the TPC signal itself. The purpose of the discussion here will be to motivate the simple models used for the present analysis. A more in-depth overview of the physics can be found in [81]. Three main effects have to be considered: The probability distribution of the charge in individual clusters, the truncated mean, and additional detector effects.

For each cluster, there is an associated length of track traversing the pad-row. The ionization of the gas due to the charged particle along this track approximately (excluding some edge-effects) corresponds to the signal found at the pads after amplification. The signal for a single cluster is the sum of the energy loss for several individual interactions of the charged particle with the gas. While the exact details of the individual interactions depend on the gas composition [81], the sum over a finite track length can

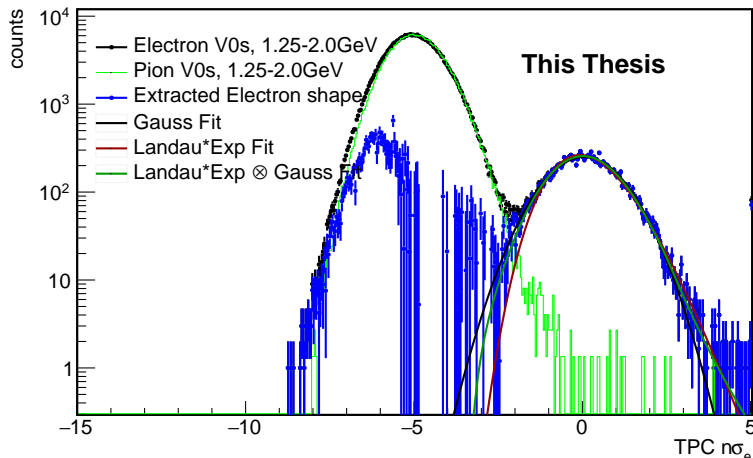


Figure 6.9: TPC Signal distribution from the V0 sample. Several functions were used for the extrapolation towards lower signal.

be approximated by a Landau distribution [80].

As discussed in section 4.3, the signals of the different clusters are combined using a truncated mean: Out of all PID clusters of one track, only the 60% with the lowest signal are considered for the average. As a result, the tail of the distribution towards higher values is reduced. It can be shown that with some assumptions the effect of the truncated mean can be approximated with a function of the form [91]:

$$f(\Delta) \sim L(\Delta) \cdot \exp(-\lambda\Delta) \quad (6.2)$$

Where Δ is the energy loss, $L(\Delta)$ is the Landau distribution and λ is a positive, real constant. A brief motivation for this form may be found in appendix B.1.

The full shape of the TPC signal distribution depends also on additional effects. There is a dependence on the track length: A track at a larger pseudorapidity has a larger track length associated with individual clusters, meaning a larger number of individual interactions and thus a different shape of the resulting TPC signal. Additionally, there are dependencies on the number of clusters, the event multiplicity, electronics noise etc.. As a significantly simplified model, these can be interpreted as different independent probability distributions that are sampled and added to the signal. If there are sufficiently many effects of similar size, the total effect should resemble a Gaussian noise that is added onto the signal. If they dominate, the resulting distribution should resemble a Gaussian.

The sum of the effects of the Gaussian noise and the truncated mean results in a

convolution of the distributions, giving a simple model to describe the TPC signal:

$$f(\Delta) \sim L(\Delta) \cdot \exp(-\lambda\Delta) \otimes G(\Delta) , \quad (6.3)$$

where $G(\Delta)$ is a Gaussian distribution. This model has four free parameters: The mode and width of the Landau distribution, the parameter in the exponential function and the width of the Gaussian. There are two important limiting cases: If the Landau-Exponential is much wider than the Gaussian, the distribution is dominated by the effect of the truncated mean. If the Gaussian is much wider, the distribution is dominated by noise effects. This motivates two simpler models to represent the extreme cases: The model of equation 6.2, which will be called the Landau-Exp-model and a pure Gaussian model. The limiting cases are useful to estimate the uncertainty inherent in the strong model assumptions.

An important additional effect was shown in [92]: The TPC signal distributions (as well as $n_{\sigma,e}^{\text{TPC}}$) have a significant tail towards higher values in central Pb–Pb collisions as shown in figure 6.13. This was shown by selecting a pure sample of pions with the TRD. The effect was attributed to shared clusters in the TPC. The high multiplicity in central Pb–Pb collisions can occasionally lead to tracks being very close through much of the TPC volume. In this case some of the clusters may contain charge from the ionization by both particles, while the tracking algorithm is unable to distinguish them. This leads to tracks with an associated signal that is of a factor of order two higher than the pion signal. The effect can be seen in figure 6.2, where a "cloud" is visible above the electron line. As a consequence, the effect is very important for the estimation of the remaining contamination of the electron sample. For the V0 sample the effect is reduced due to the additional selection criteria. This difference will be considered later, to extract the true TPC PID selection efficiency. The effect is not included in the models described above.

To assess the accuracy of the models, they were tested using the V0 pions. Due to the large abundance of such pions, the contamination of the sample is significantly lower than for the electrons. The resulting fits are shown in figure 6.10. As expected, the full model of equation 6.3 fits best. The reasons for this are both that it describes more effects and the fact that it contains an additional free fit parameter. The extreme models Landau-Exp and the pure Gaussian under- or overestimate the measured distribution typically where the other deviates to the other direction. This gives further credence to the interpretation that they present limiting cases. Some contamination may be present in the tails of the distribution, but the result does not depend strongly on the fit range. This suggests, that any remaining contamination does not have a strong influence on

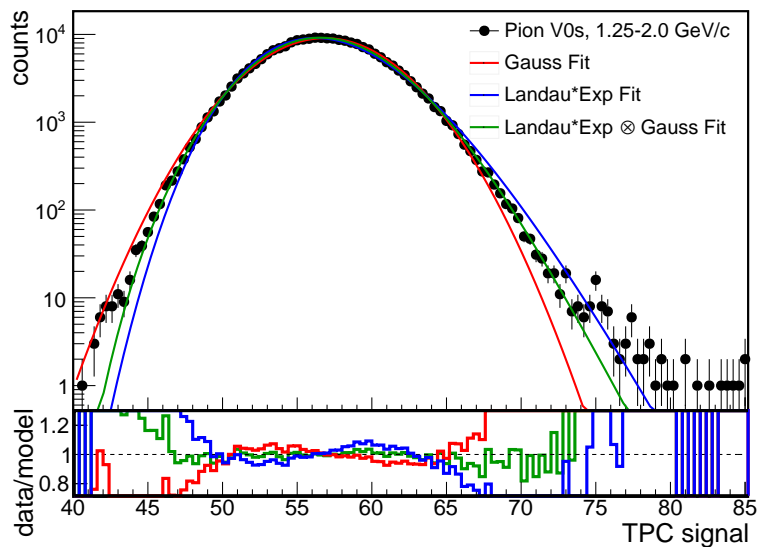


Figure 6.10: TPC Signal distribution for pions from the decays of kaons with fits of the models. The pure Gaussian and Landau-Exp models deviate in opposite directions.

Model	p_T -range	
	1.25 – 2 GeV/c	2 – 3 GeV/c
Gauss	0.696	0.745
Landau-Exponential	0.724	0.768
Landau-Exponential \otimes Gauss	0.707	0.745

Table 6.1: Estimates of the TPC PID selection efficiencies estimated with the three models.

the efficiency estimation.

The models could now be applied to the electron V0 distribution. However, the remaining hadron contamination limits the fit range somewhat, as it is not clear at which point on the left of the peak in figure 6.9 the deviation from the pure electron signal distribution becomes significant. The pion V0 sample can be used to slightly improve upon this. It is important to note that it cannot be directly subtracted because the different selection criteria of the pion V0 sample and the electron V0 sample gives a slight bias to the distribution. The slope of the right flank however is approximately reproduced. By fixing the amplitude there, the contamination in the region of the electron peak is reduced. The fit was performed in the region $-1.5 < n_{\sigma,e}^{\text{TPC}} < 5$ with the results shown in figure 6.9.

The fits result in an estimate of the TPC efficiency for each of the models. The

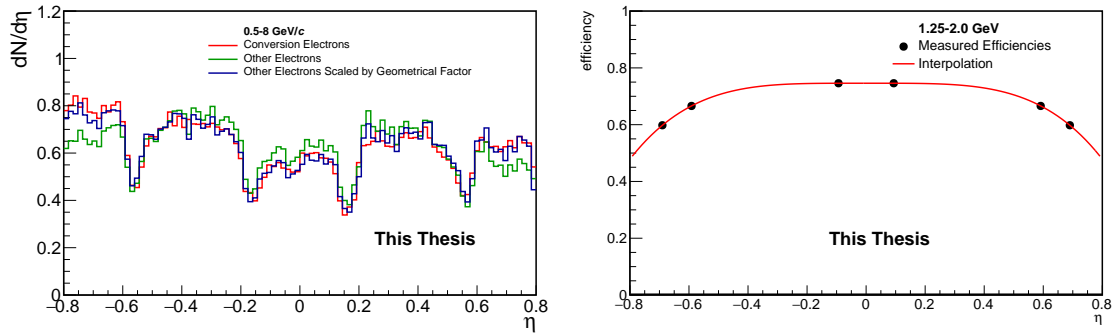


Figure 6.11: *Left*: Normalized pseudorapidity distributions of electrons from photon conversions and from other processes in Monte Carlo simulations. The large p_T -range was chosen to decrease statistical fluctuations. *Right*: Pseudorapidity dependence of the TPC signal selection efficiency. The estimate was performed in ranges of $|\eta|$, with mirrored points plotted.

most complex model given by equation 6.3 was considered to be the central estimate, with the two limiting cases being used for the estimation of the modeling uncertainty. The fits were performed in two different p_T -ranges. The ranges were chosen to be fairly large in order to have sufficient statistics. Figure 6.9 shows the resulting fits, while the resulting efficiency estimates are given in table 6.1. The difference between the central model and the limiting cases is of the order of 2%. This value was chosen to represent the uncertainty due to the modeling in the extrapolation of the electron signal.

The estimated efficiencies in the two p_T -ranges show a difference of about 5% in the central values where no effect of this size is expected. This was incorporated by using a constant efficiency estimate of 0.73 and including an additional 3% uncertainty due to the possible momentum dependence.

It is important to consider any biases of the V0 electron sample with respect to the signal electrons. An important effect is the pseudorapidity dependence of the signal. Figure 6.11 (left) shows the difference of the pseudorapidity distributions of electrons from photon conversions in comparison to those from other processes. In comparison, more conversion electrons (red line) are produced at larger values of the absolute pseudorapidity than other electrons (green line). The difference can be explained by the difference in the material budget for photons at different pseudorapidities. For a cylindrical geometry, the material budget yields changes with pseudorapidity by a factor of $\cosh(\eta)$ (calculation in appendix B.2). Multiplying this factor to the η -distribution the other electrons yields a distribution (blue) very similar to that of electrons from photon conversions, suggesting

that this is the main effect for the changed distribution. In order for this pseudorapidity dependence to play a role, the efficiency must depend on the pseudorapidity.

To estimate the η -dependence of the efficiency of the TPC PID requirement, the fits mentioned above were performed separately for different intervals of $|\eta|$: $|\eta| \in [0, 0.2]$, $[0.4, 0.8]$, $[0.6, 0.8]$. The resulting estimate of the η -dependence of the efficiency shown in figure 6.11 (right) was then interpolated using a function of the form $p_0 + p_1\eta^4$ with two free parameters. Applying the different pseudorapidity distributions shown in figure 6.11 (right) to this result, yields an effect that is smaller than 2%.

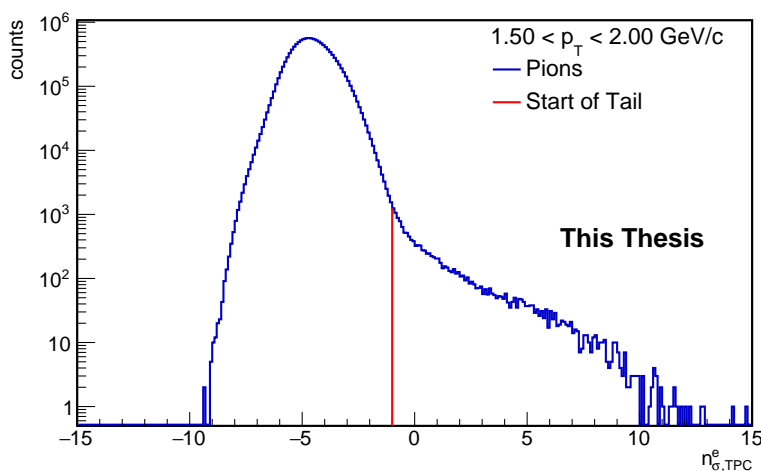


Figure 6.12: $n_{\sigma,TPC}$ -distribution for pions selected with the TRD [93]

The second important bias to the efficiency estimated with the V0 sample is the tail of the true distribution towards larger signal values. It is estimated by studying the corresponding effect for pions. This cannot be achieved using the V0 pion sample shown in figure 6.10 because the selection of the decay geometry should decrease the tail in a similar way as for the V0 electrons. For this reason, pions were selected using the TRD. The resulting distribution is shown in figure 6.12. As discussed in [92], two types of biases can occur: The TRD PID requirement might itself bias the distribution towards higher quality tracks and thus decrease the influence of the tail. On the other hand some remaining electron contamination might increase the estimate of the pion tail. It is not obvious from figure 6.12, where the roughly exponential fall of the main peak ends and the tail starts. The assumption of reasonable starting points for the tail (as indicated in figure 6.12) suggest that significantly less than 1% of particles end up in the tail. This ratio decreases quickly with p_T due to the combinatorial nature of the effect. The effect

Criteria	approx. efficiency	uncertainty estimate
2 ITS + 30 TPC clusters	0.94	3%
ITS	0.57	2%
TPC track quality	0.9	3%
TOF	0.6	10%
TPC PID	0.73	5%
total	0.2	12.1%

Table 6.2: Systematic uncertainties of the track selection and PID steps.

on the efficiency should thus be smaller than 2%.

For the TPC PID requirement, the uncertainty of the efficiency has contributions from the TPC signal model (2%), the possible p_T -dependence (3%), the η dependence (2%) and the tail of the distribution (2%) yielding a total of about 5%. The uncertainties for all efficiencies were assumed to be independent and were thus summed in quadrature. An overview may be found in table 6.2.

6.3 Hadron contamination

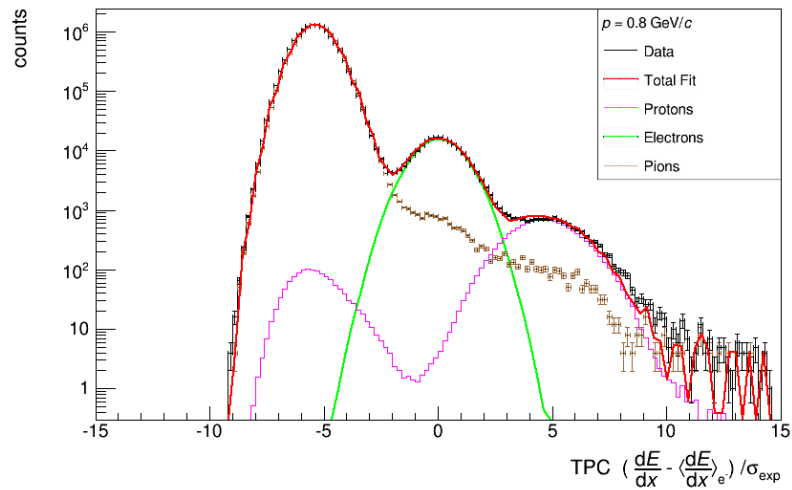


Figure 6.13: Template fit used for the estimation of the hadron contamination (from [92])

The remaining hadron contamination after all track selection criteria are applied is treated implicitly by the signal extraction method (discussed in chapter 7). An estimate for the impurity can be found in [92], where the hadron contamination was estimated

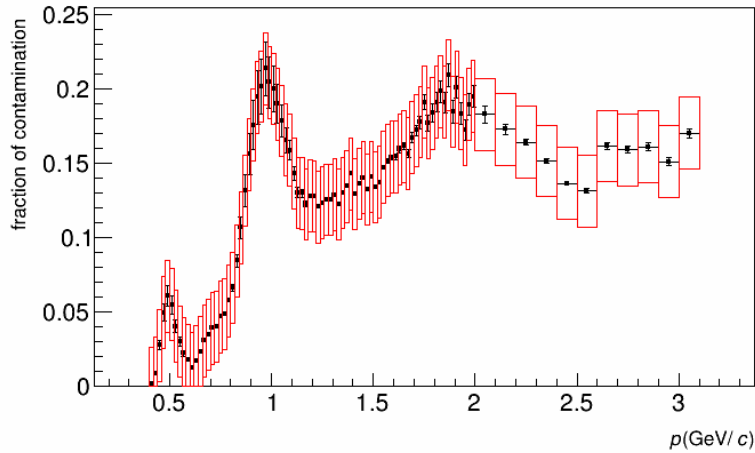


Figure 6.14: Estimated contamination using a TPC PID selection of $0 < n_{\sigma_{\text{TPC}}} < 3$ (from [92]).

for a requirement of $0 < n_{\sigma,e}^{\text{TPC}} < 3$. This was done by fitting the TPC signal of the background with signal templates selected with the TOF and TRD as shown in figure 6.13. The electron signal distribution was approximated by a Gaussian. The resulting estimate of the contamination is shown in figure 6.14. This shows a typical hadron contamination of about 15% even at low p_T . Towards higher p_T , the influence of the tail decreases, but the peak of the pion signal distribution moves closer to that of the electrons. The looser cut of $-0.5 < n_{\sigma,e}^{\text{TPC}} < 3$ in the analysis discussed in this work should increase the contamination further. Thus, a sizeable hadron contamination consisting mostly of charged pions can be expected throughout the measured range. Its effect on the measurement is quantified in section 7.3.4.

Chapter 7

Signal Extraction

After preparing the sample of electron candidates, the next step is to extract the fraction of electrons from the decays of beauty hadrons. This can be achieved by using the impact parameter of the electrons as additional information. The first part of this chapter is concerned with the different sources of electrons and how they can be grouped for the signal extraction. The second part explains the mathematical foundation of the signal extraction method. The associated sources of uncertainty are discussed in the third part.

7.1 Electron sources

The electrons in the sample have many different sources. Their relative importance for the analysis varies strongly with p_T . Figure 7.1 shows an estimate for the non-heavy flavor background electrons in pp collisions at $\sqrt{s} = 7$ TeV [88]. This background is dominated by the decays of light mesons, e.g. the three-body Dalitz decay of the neutral pion: $\pi^0 \rightarrow e^+e^-\gamma$. The light mesons typically also have large branching ratios to photons (e.g. $\pi^0 \rightarrow \gamma\gamma$ with about 99% [11]). In relation, the contribution from direct photons is very small [94]. Photons can convert to electron-positron pairs in the detector material.

Strange particles contribute additionally to the background. Their fractional contribution is small due to the fact that they have a long decay length and thus often decay outside of the innermost layer of the ITS, excluding them from the measurement. The long decay length however results in a very wide impact parameter distribution for the remaining electrons. There is also a small contribution from the decays of J/ψ particles, which are not considered part of the charm contribution for the background classification.

Another background contribution are the electrons from the decays of charm hadrons.

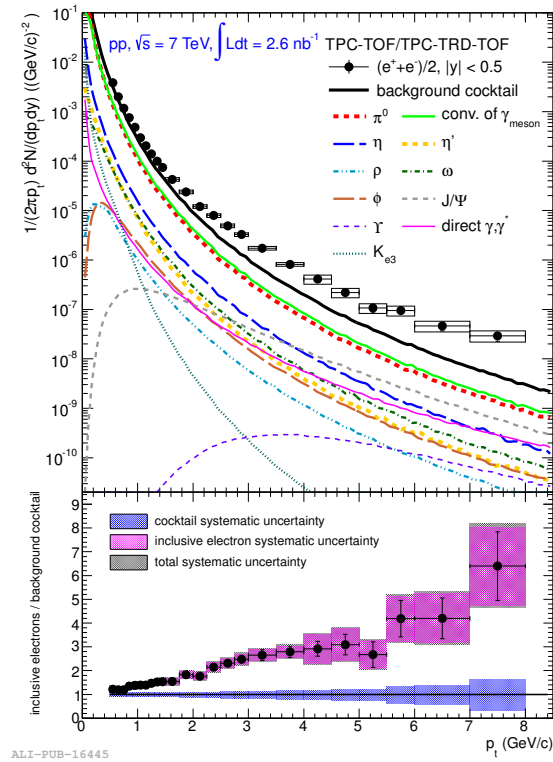


Figure 7.1: Non-heavy flavor electron sources in pp collisions at $\sqrt{s} = 7$ TeV compared with the measured cross section of electrons. The ratio of the measured (inclusive) electrons to the background shows that the heavy flavor contribution dominates towards higher transverse momenta [88].

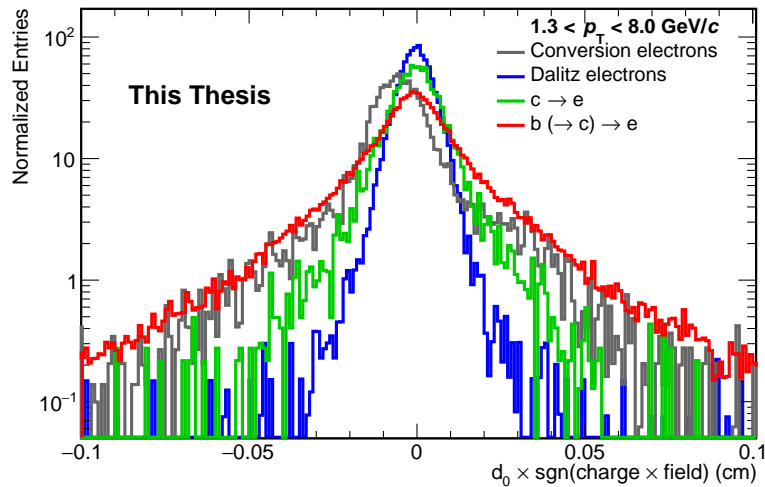


Figure 7.2: p_T -integrated and normalized impact parameter distributions for the four groups of electron sources discussed in the text. The distributions for Dalitz and conversion electrons are from minimum bias Monte Carlo simulations, while those for charm and beauty hadron decays come from the enhanced Monte Carlo sample.

These originate mainly from the decays of D^0 , D^+ and D_s mesons and Λ_c baryons (as well as their antiparticles). Finally, the hadron contamination should be considered. It consists mostly of charged pions produced close to the primary vertex.

For the purpose of a study based on the impact parameter, it is more reasonable to group the background contributions in terms of their impact parameter distributions instead of the source. Four groups were created for the purpose of this analysis. Their p_T -integrated impact parameter distributions are shown in figure 7.2.

The first group is the signal: *Electrons from beauty-hadron decays*. The beauty hadrons typically have decay lengths of the order of $500 \mu\text{m}$. Additionally, they often decay to charm hadrons, which can also decay to electrons and thereby add a significant decay length (table 5.1). This results in an impact parameter distribution that is wider than the impact parameter distributions for most background contributions in the measured p_T -range. The distribution is also significantly wider than the impact parameter resolution and approximately symmetric around zero. The connection to the decay length is illustrated in figure 5.2.

Similar considerations also apply to the *electrons from charm-hadron decays*. The main difference is the shorter decay length. As a result, their impact parameter distribution is slimmer than that of the beauty-hadron decay electrons. Additionally the decay

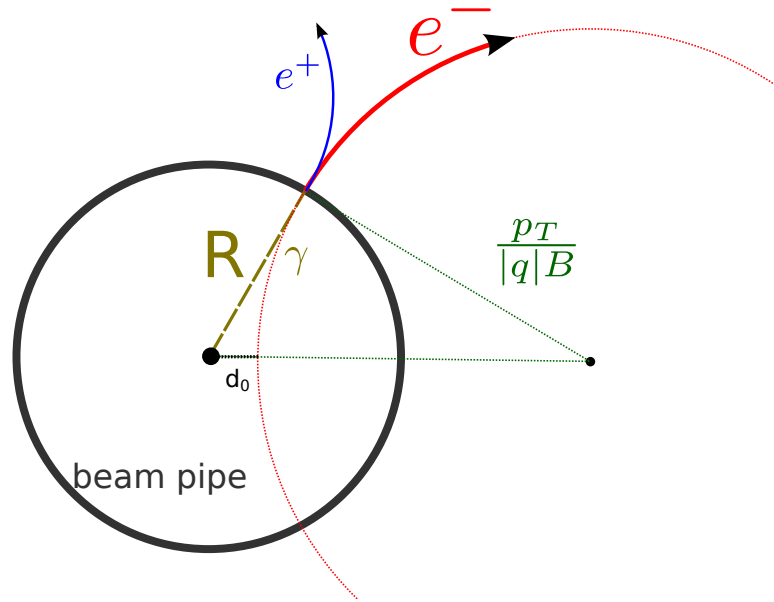


Figure 7.3: Sketch of the production of conversion electrons in the detector material (e.g. the beam-pipe).

length also varies significantly between the different charm-hadron species. This results in a peak width that is of the order of the impact parameter resolution while the tails of the distribution extend further outward. Thus, the impact parameter distribution of charm-hadron decay electrons is composed of several contributions with different impact parameter distribution, giving some uncertainty of its shape. This uncertainty has to be taken into account in particular with respect to its effect on the estimate of the beauty contribution.

The third group contains *electrons from photon conversions in the detector material*, which will be referred to as **conversion electrons** in the following. The photons are produced mostly from the decay of light mesons. In the transverse plane, the tracks of the electron and positron are circles due to the constant magnetic field. With the added information that the angle of the momentum of the produced electron (or positron) to the photon is of the order $m_e c^2 / E_e$ [95] and thus very small, a typical value of the impact parameter is

$$|\langle d_0 \rangle| \approx \frac{R^2 |q| B}{2 p_T} . \quad (7.1)$$

The process is sketched in figure 7.3. A short derivation may be found in appendix

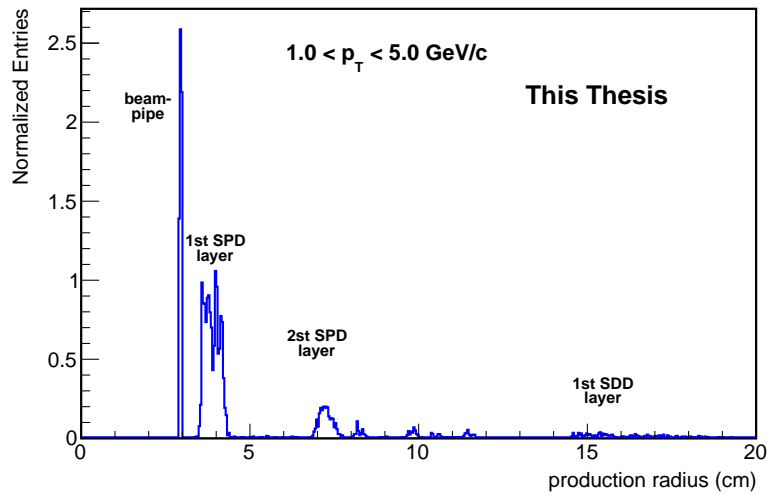


Figure 7.4: Distribution of the production radii of conversion electrons in the Monte Carlo minimum bias sample after application of the track selection criteria.

B.3. While the decay typically happens quite far from the primary vertex (the radius of the beam pipe is 3 cm compared to $c\tau \approx 500 \mu\text{m}$ for the beauty hadrons) the small angle to the photon means that the impact parameter appears only due to the magnetic field. As mentioned in chapter 5, within the ALICE computing framework, the sign of the impact parameter depends on whether the track passes the primary vertex on the left or right (with respect to the momentum vector). As a result, the average impact parameter for conversion electrons and positrons would have an opposite sign. This would yield impact parameter distributions that are mirrored versions of each other. A switch of the magnetic field would have the same effect. For this reason, it is useful to multiply the sign of the charge and field configuration with the impact parameter value. In this case, the sign of the impact parameter indicates whether the primary vertex is inside or outside of the circle of the track in the transverse plane. The other distributions are affected very little, because they are nearly symmetric. As a result, the impact parameter distribution of the conversion electrons (shown in figure 7.2) is the only one with significant asymmetry, making it easier to distinguish with the signal extraction method explained in the next chapter.

An important property of the conversion electrons, is the quadratic dependence of their typical impact parameter on the production radius as given in equation 7.1. As a result, conversion electrons with a large production radius are less distinguishable from the signal. Conversely, suppressing conversion electrons with large production radii

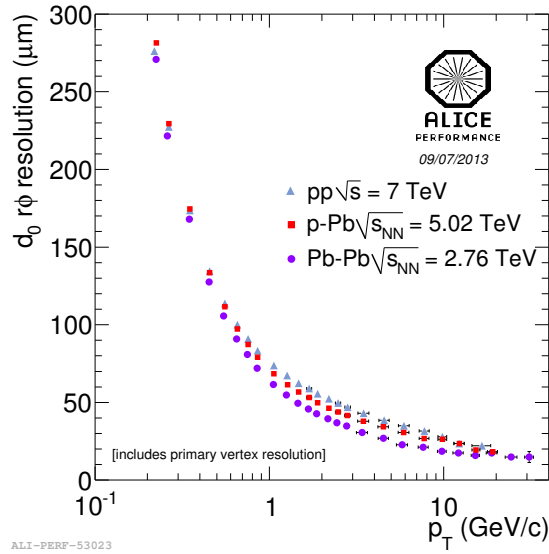


Figure 7.5: Transverse impact parameter resolution in pp, p–Pb and Pb–Pb collisions with ALICE

increases the accuracy of the beauty-hadron decay electron measurement. As described in chapter 6, the requirement of signals in both of the innermost layers of the ITS serves this purpose. For the smaller radii, the distribution is narrow compared to the resolution of the impact parameter. The same is true of the higher p_T -bins due to the p_T^{-1} -dependence. This means, that the impact parameter distribution of conversion electrons depends on the resolution of the impact parameter as well.

The ITS signal requirements strongly decrease the number of conversion electrons produced at larger radii, but some contribution still remains. The distribution of the production radii in central Pb–Pb collisions is shown in figure 7.4. The conversion electrons with large production radii pass the ITS signal requirements due to a stochastic misassociation of other signals in the ITS. It is a result of the large multiplicities of the central Pb–Pb collisions. It is important to study this effect well because it contributes to the signal at large impact parameters. A second such contribution comes from photons produced in the decays of strange particles (e.g. $K_s^0 \rightarrow \pi^0 \pi^0$, $\pi^0 \rightarrow \gamma \gamma$). The fundamental difference is, that in this case the photon itself originates in a displaced vertex and as a result, the impact parameter is not a result of the magnetic field only. Similar to the misassociated conversion electrons described previously, the total number of such electrons is low, but due to the fact that their impact parameter distribution itself is wide, it is important to understand how well it is reproduced in the simulations.

The last group contains all *remaining electron contributions*. By far the largest contribution in the measured p_T -range is the contribution from the decays of light mesons.

For the purpose of brevity, these electrons will be referred to as **Dalitz electrons** in the following. The impact parameter distribution of particles produced at or very close to the primary vertex is for the most part determined by the impact parameter resolution. Figure 7.5 shows the impact parameter resolution for charged particles in different collision systems. The resolution improves with the multiplicity of the collision because the primary vertex can be determined with greater accuracy if more tracks contribute. As a result, the separation of the Dalitz electrons is slightly easier for central Pb–Pb collisions than in pp collisions due to the sharper peak.

Similar as for the photons, some of the electrons originate from the decays of strange hadrons. They often have an impact parameter that is large compared to the resolution. To make sure that the impact parameter distributions for the different groups are well represented by the Monte Carlo simulations, many possible deviations have to be checked and any uncertainties propagated to the final result. In the next section an accurate representation will be assumed to explain the method of the signal extraction.

7.2 Fit method

The purpose of this section is to describe how to use the different impact parameter distributions discussed in section 7.1 to estimate the fraction of electrons from beauty hadron decays. The different impact parameter distributions do not have a simple analytical form due to the complexity of the processes that are involved. Instead, information about them is gained using the Monte Carlo simulations, which include information about the decay properties as well as detector effects and the reconstruction algorithm. The discussion in this section will concern the measurement in an individual p_T -bin. It is useful to also discretize the impact parameter (as shown in figure 7.2). The distributions of the impact parameter as given by the Monte Carlo simulations will be referred to as impact parameter **templates** in the following.

The data d consists of an integer number (counts) d_i for each impact parameter bin i . Similarly, the Monte Carlo templates consist of an integer number a_{ji} for each source j and impact parameter bin i similar to what is shown in figure 7.2. There is also an unknown true distribution of the impact parameter, f , with a positive, real number f_i for each impact parameter bin. Similarly, there are distributions of the expectation values of the bin contents for the templates from the Monte Carlo simulations: A , where A_{ji} is the expectation value of the counts of impact parameter bin i for source j . For each electron, there is a small and independent probability to lie in bin i . Thus, the associated

probability distribution is the Poisson distribution. This means:

$$p(d_i|f_i) = \frac{f_i^{d_i} e^{-f_i}}{d_i!} \quad (7.2)$$

for the data and similarly

$$p(a_{ji}|A_{ji}) = \frac{A_{ji}^{a_{ji}} e^{-A_{ji}}}{a_{ji}!} \quad (7.3)$$

for the Monte Carlo templates.

The assumption that the templates reproduce the data means, that a weighted sum of the expectation values of the individual sources A_{ji} should yield the true distribution of the data given the correct weights. In other words, there exist amplitude factors p_j such that

$$f_i = \sum_j p_j A_{ji} \quad \forall i. \quad (7.4)$$

There is one such unknown parameter for each source. From the knowledge of p_{beauty} it would be easy to estimate the fraction of electrons from beauty-hadron decays. Thus, this is the parameter to estimate. From Bayes' theorem, it is now simple to calculate the full probability for all unknown parameters:

$$p(\mathbf{p}, \mathbf{A} | \mathbf{d}, \mathbf{a}) \sim \left(\prod_i f_i^{d_i} e^{-f_i} \right) \left(\prod_{i,j} A_{ji}^{a_{ji}} e^{-A_{ji}} \right) p(\mathbf{p}, \mathbf{A}), \quad (7.5)$$

with $p(\mathbf{p}, \mathbf{A})$ the prior, which will for now be considered to be constant in the parameters. Some prior information is available from the knowledge of the physical processes leading to the distributions. It was included indirectly as will be shown later.

Equation 7.5 gives the full solution to the discretized problem. The probability distribution for p_{beauty} can be obtained by integrating over the free parameters of the fit (marginalization). The free parameters for this case are the other p_j and the A_{ji} . For 200 impact parameter bins and four different sources, there are 804 free parameters in total. As a result, the integration becomes quite complex. A fairly direct approach to achieve this numerical integration is the use of Markov-Chain Monte Carlo methods [96]. However, at present it is difficult to fully ensure convergence within a reasonable time. Figure 7.6 shows the autocorrelation [97] of the parameters in a toy-measurement (an example built from the Monte Carlo templates with known true values). *Lag* signifies the offset between the steps. Even for a separation of 100000 steps there is a significant autocorrelation. This means that a very large number of steps is necessary to approximate the true distribution.

To estimate the mean of $\langle p_{\text{beauty}} \rangle$, the mode of the posterior distribution (Eq. 7.5) was used instead. For a flat prior distribution, this is equivalent to a maximum likelihood

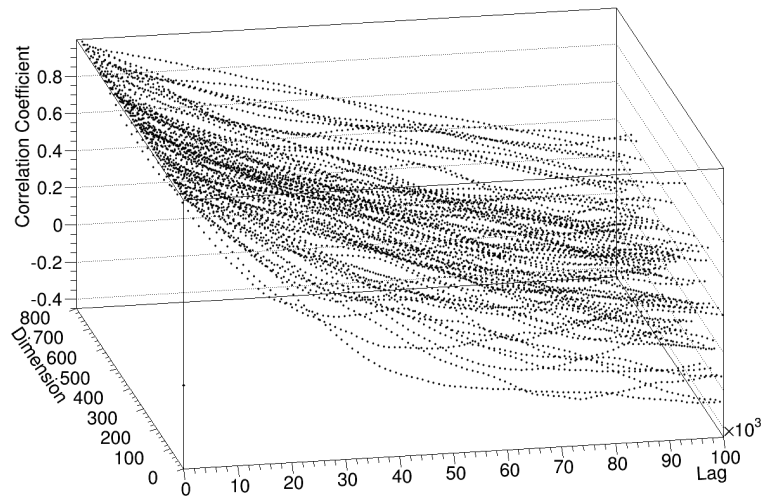


Figure 7.6: Autocorrelation plot for an example measurement built from the Monte Carlo simulation templates. The plot shows that points with many intermediate iterations still show significant correlation. ‘Dimension’ signifies the number of the parameter of the model. (figure taken from [96])

approach. This approximation may contain a bias with respect to the expectation value, which must be estimated as well. The logarithm of the likelihood is [98]

$$\log \mathcal{L} = \sum_i d_i \log f_i - f_i + \sum_i \sum_j a_{ji} \log A_{ji} - A_{ji} . \quad (7.6)$$

7.2.1 Maximum likelihood estimation

The likelihood given in equation 7.6 has 804 free parameters making the search for the maximum challenging. While it is possible to look for the maximum directly using e.g. an implementation of the Minuit package [99], an iterative approach is suggested in [98]. To find the maximum, the differentials with respect to the free parameters are set to zero. From the requirement of $d\mathcal{L}/dA_{ji} = 0$ follows:

$$\frac{d_i p_j}{f_i} - p_j + \frac{a_{ji}}{A_{ji}} - 1 = 0 \quad \forall j, i . \quad (7.7)$$

For fixed p_j these are separate sets of equations for each impact parameter bin. They can be rearranged as [98]

$$A_{ji} = \frac{a_{ji}}{1 + p_j \left(1 - \frac{d_i}{f_i}\right)} . \quad (7.8)$$

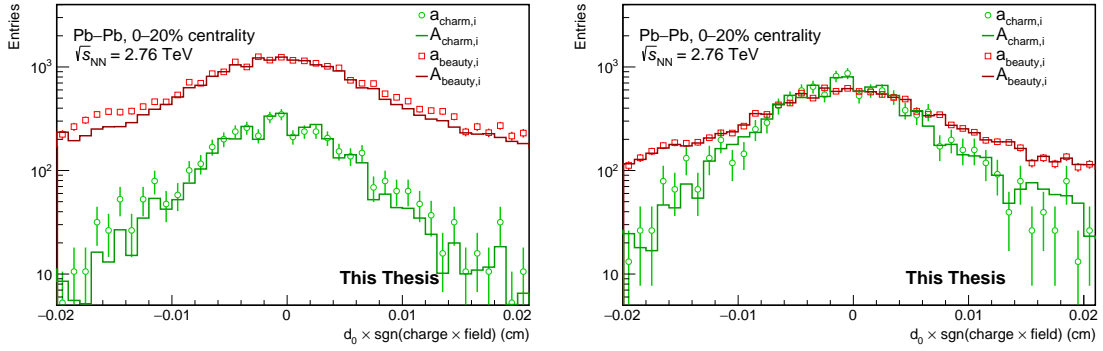


Figure 7.7: The A_{ji} and a_{ji} for beauty- and charm-hadron decay electrons scaled with their amplitudes. *Left*: For the iteration procedure of equation 7.8. *Right*: For the iteration procedure given in equation 7.10.

For every proposal of the p_j , these equations can be solved iteratively by inserting the current A_{ji} on the right side and updating them with the result. This leaves only the four p_j as free parameters. The minimization can then easily be done numerically. The left side of figure 7.7 shows the $p_j A_{ji}$ resulting from the full procedure in comparison with the $p_j a_{ji}$. The likelihood contains information about the A_{ji} that comes both from the Monte Carlo templates and from the data. Without the data, the maximum likelihood would always lead to $A_{ji} = a_{ji}$. The information from the data should push the values towards the true distribution and thereby slightly smooth them. It is obvious from the plot that this is not the case as there is a bias towards lower values towards the edges. Another possibility is to solve equation 7.7 for A_{ji} . With the definition

$$f_{i \setminus j} = \sum_{k \neq j} p_k A_{ki} \quad (7.9)$$

this yields

$$A_{ji} = -\frac{1}{2} \frac{d_i p_j - f_{i \setminus j}(p_j + 1) + a_{ji} p_j}{p_j(p_j + 1)} + \sqrt{\frac{1}{4} \left(\frac{d_i p_j - f_{i \setminus j}(p_j + 1) + a_{ji} p_j}{p_j(p_j + 1)} \right)^2 + \frac{a_{ji} f_{i \setminus j}}{p_j(p_j + 1)}} \quad (7.10)$$

The result is shown on the right side of figure 7.7. It is different from the left plot and in line with the expectation. Apparently the convergence of the iteration with equation 7.8 is not as stable – at least for this particular task. The square root in equation 7.10 requires additional computation time, but the calculation gives a more stable result.

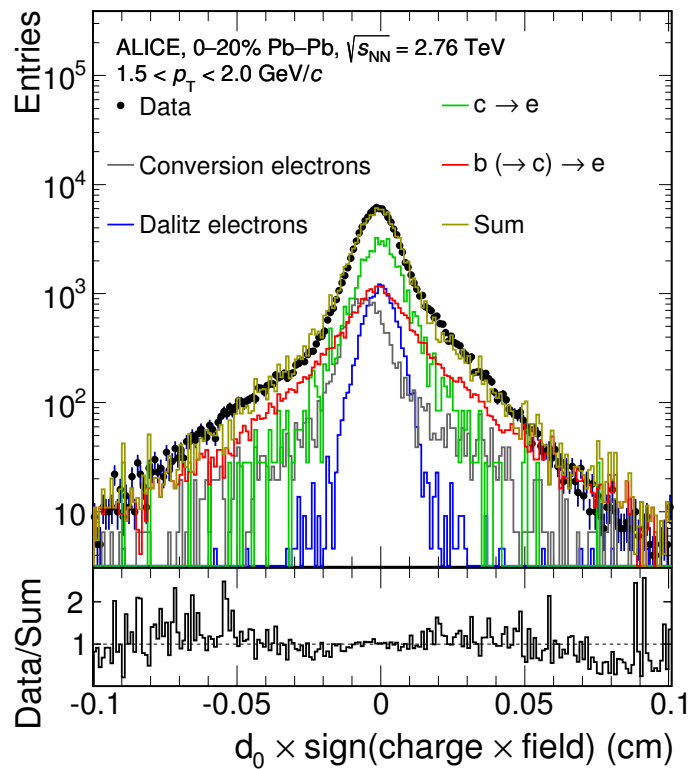
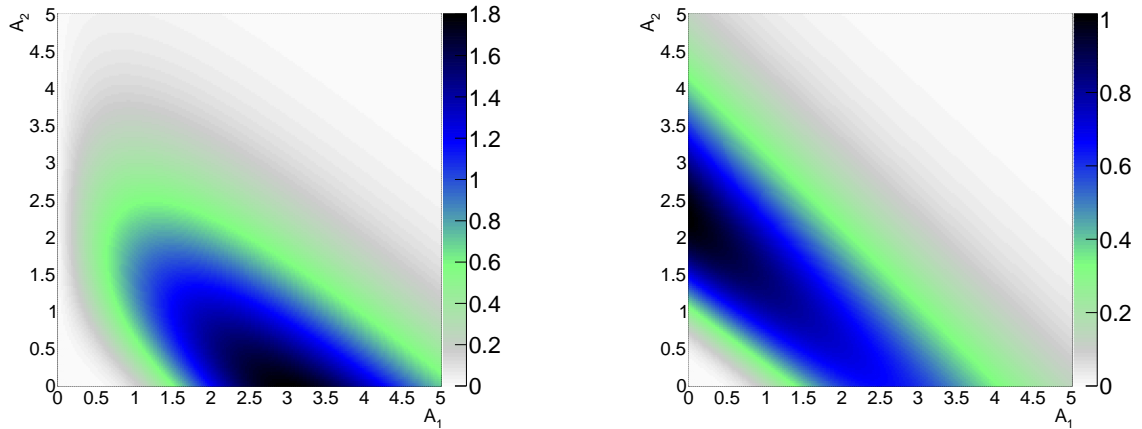


Figure 7.8: Example of the fit in a single p_{T} -bin. The sum given here is not f_i , which is the weighted sum of the A_{ji} (which would be very close to the data) but the weighted sum of the a_{ji} . In this way, the statistical fluctuations in the templates and the data can be compared. (publication in preparation [46])



$$d = 5$$

$$a_1 = 1 \quad p_1 = 1.0$$

$$a_2 = 0 \quad p_2 = 1.2$$

$$d = 5$$

$$a_1 = 0 \quad p_1 = 1.0$$

$$a_2 = 0 \quad p_2 = 1.2$$

Figure 7.9: Likelihood distributions for an example impact parameter bin with two sources.

For each new step in the maximization with respect to the p_j , this iteration is started from the previous values for the A_{ji} . After about 5 iterations, the values do not change significantly any more. For safety, the results shown in this work were created using 10 iterations.

An example of the resulting fit is shown in figure 7.8.

7.2.2 Bins without counts from Monte Carlo simulations

If a template has no entries within one bin, meaning $a_{ji} = 0$, equation 7.7 leads to

$$\frac{d_i}{f_i} - 1 = \frac{1}{p_j} . \quad (7.11)$$

If several templates have zero entries in the bin, this has to be true for all these p_j , leading to inconsistencies [98]. Figure 7.9 shows the reason for this: The maximum of the likelihood is at the edge of the allowed parameter space ($A_{ji} \geq 0$) and the derivatives are not necessarily zero there. If there are not counts a_{ji} in any of the templates of this impact parameter bin, the maximum appears at the point where all A_{ji} are zero except for one (figure 7.9, right). This is the one with the largest associated amplitude parameter p_j . The reason for this is that in this case, a smaller expectation value A_{ji} is necessary to make an expected measurement f_i that is consistent with the finite data counts d_i .

The resulting likelihood distribution (and thus also the probability distribution) typically shows a wide region of points with high values. The parameters are strongly anticorrelated as there is not much information to favor one electron source over the other. As a result, the maximum likelihood (and thus maximum of the probability distribution) is not representative of the full distribution, which was the condition for using it in the first place. Using the maximum without further input would introduce a bias into the measurement.

Instead, the approach in this work is to make use of prior information about the probability distributions. To approach this, it is useful to consider, what information is not contained in the Monte Carlo templates. From the physical processes leading to the distributions (as explained in section 7.1), they should have a single peak around zero and decrease towards larger and smaller values of the impact parameter (excluding the case of the conversion electrons). However, the probability distribution of formula 7.5 does not contain this information. Any permutation of the order of the impact parameter bins would lead to the exact same result. Additionally, this means that adjacent impact parameter bins do not 'talk to each other', meaning that there is no requirement for local smoothness. Smoothness of the true distribution can be expected at least on the scale of the impact parameter resolution. On the other hand, the ad hoc inclusion of a smoothness requirement usually biases the distributions, making them wider. For that reason, a more cautious approach is chosen in this work.

If the case of impact parameter bins with no counts from some of the Monte Carlo templates occurs, it will usually appear in the tails of the distribution where A_{ji} is of order one or smaller. From the knowledge of the different widths of the distributions, this means that the counts there should mostly come from beauty-hadron decay electrons because the impact parameter distribution is wider than the others. Due to the fact that the signal-enhanced Monte Carlo sample is used to obtain the Monte Carlo template for the beauty case, it has large statistics. As a result, one can expect $p_{\text{beauty}} \ll p_{\text{Dalitz}}, p_{\text{Conversion}}$. While the prior knowledge suggests, that the counts should come from beauty (or perhaps charm), the maximum of the likelihood will be at $A_{\text{beauty},i} = 0$ with all counts associated with the Dalitz or conversion electrons. This can be understood by considering the case without data: If only the templates are available as information, the likelihood has its maximum at $p_j A_{ji} = 0$, but the width scales with p_j . As a result, the larger p_j is, the larger is the compatibility with a nonzero value. Since this is the case for the conversion and Dalitz electron templates, these contributions are favored by the likelihood without including the knowledge that the nonzero counts probably come from the beauty-hadron decay electrons. To include the prior

knowledge, the point is chosen differently: For each impact parameter bin, if a Monte Carlo template contains $a_{ji} = 0$ counts, then $A_{ji} = 0$ is assumed, except for the case of beauty electrons. For bins without entries in any of the Monte Carlo templates, this means that

$$A_{\text{beauty},i} = \frac{d_i}{1 + p_{\text{beauty}}} . \quad (7.12)$$

This approach significantly reduces the bias of the estimator. However, it is possible that entries appear in the bins that originate from another source. As a result, some bias may remain. Due to the fact, that this approach is still very similar to the pure maximum likelihood approach, the resulting point in the space of the A_{ji} and p_j will simply be referred to as the maximum likelihood in the following.

7.2.3 Uncertainty estimation and bias correction

As mentioned previously, the posterior probability distribution is obtained by marginalization of equation 7.5. The expectation values are approximated by its mode and width. The estimate for the mode comes from the likelihood as discussed in the previous sections. It should be corrected for any remaining biases. The approach given in this section yields both an approximation for the width as well as for the bias correction.

The statistical uncertainty of a parameter measurement is closely connected to the fluctuation of the measured value if the experiment was repeated several times. If the width of the distribution of the measurement does not vary quickly with the parameter within its uncertainty, then it is a useful approximation. This is true in particular if the distribution is close to Gaussian. Stated differently, if the experiment is repeated several times, the variation of the parameter approximates the uncertainty of a single estimate. A comparison of the average parameter estimate to the true value of the parameter yields the bias of the measurement. Of course, this comparison cannot be done directly, as the true value of the parameter is unknown, but it can be approximated.

For given true values of the p_j and A_{ji} it is simple to virtually repeat the experiment many times by simply sampling the A_{ji} and f_i distributions according to the statistics in the measured data and in the Monte Carlo templates. With the true values of the p_j and A_{ji} unknown, they have to be approximated. The A_{ji} can be approximated by the templates, a_{ji} . The p_j can be approximated by using the measured values, the results of the maximum likelihood approach. This yields a good estimate of the true values as long as the true uncertainties are not too large. In the following this procedure will be referred to as the **toy model** approach.

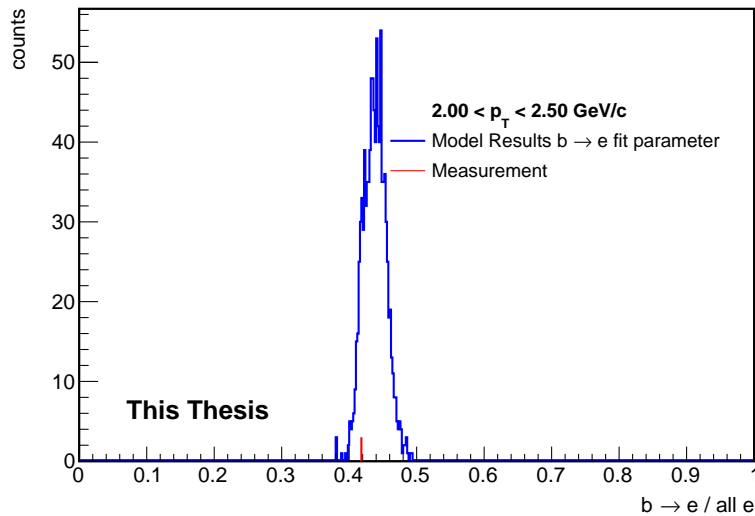


Figure 7.10: Distribution of the measurement of p_{beauty} in toy model measurements with 2000 trials in blue. The red line signifies the true input value of the models, which is taken from the measurement. The parameter is normalized such that it shows the resulting ratio of the measured electrons from beauty-hadron decays to all electrons.

The approximations of the A_{ji} by the a_{ji} of the original templates are particularly good for impact parameter bins, with large statistics because of the \sqrt{N} dependence of the distribution widths. To improve how representative the bins with few entries are, two possibilities come to mind: It is possible to choose a larger p_T -range of the Monte Carlo simulations to create the templates. Alternatively, some smoothing can decrease the fluctuations. Both improve the uncertainty estimate while at the same time possibly introducing a slight bias in the uncertainty estimation. Comparison of several such approaches showed, that the uncertainty estimates are not very dependent on the exact choice. In the end, a p_T -range of $p_{t,\text{lower}} < p_T < 20 \text{ GeV}/c$ was chosen, where $p_{t,\text{lower}}$ is the lower edge of the p_T -range that is being measured in the signal extraction. Additionally, some slight smoothing was applied.

Figure 7.10 shows the resulting distribution for one p_T -bin. The width of the distribution is not very large, giving some credence to the assumption that the toy model is representative with respect to the uncertainty. The width of the distribution was interpreted as the statistical uncertainty of the procedure. The difference between the input value of the toy model and the mean of the distribution was interpreted as the bias of the maximum likelihood estimator defined previously. The measured value for the number of beauty-hadron decay electrons was calculated after scaling p_{beauty} with this

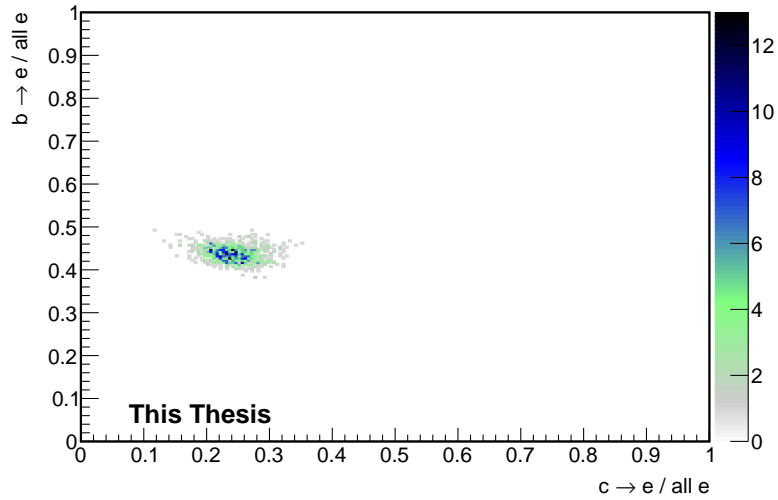


Figure 7.11: Distribution of toy model measurements with 2000 trials in the p_T -range $2 - 2.5 \text{ GeV}/c$.

correction, which corrects for the bias. The estimate of the bias itself is also associated with an uncertainty about which little is known, except that it should be smaller than the correction itself. In the absence of an estimate beyond that, the size of the correction was used as an estimate for its uncertainty.

The accuracy of this estimate mostly depends on the change of the distribution with the true value of the parameter. As the estimate is the *rms* of the distribution, its accuracy should be $O(\text{rms}^2)$. It is important to note however, that while the width for p_{beauty} is small, this does not in itself ensure that the estimate is accurate, as there are other free parameters, which might have wider distributions. It is possible, to obtain similar distributions for the other parameters as well. In this way it is easy to estimate correlations between the parameters (as shown in figure 7.11) or arbitrary functions of the parameters, such as $p_{\text{beauty}}/p_{\text{charm}}$.

It is useful to consider the fluctuations in the measured result: If the measured p_{beauty} is lower than the true value, then in the toy model the contribution of the beauty-hadron decay electrons is lower, making them more difficult to measure. This will typically increase the estimated (relative) uncertainty. On the other hand, if the measured value is higher, then the toy model will underestimate the uncertainty slightly. As discussed above, this effect should be small. However, a similar consideration applies to the background: If the measured background is lower than the true background, then the uncertainty of p_{beauty} will be underestimated and vice versa. This effect mostly concerns

the electrons from charm-hadron decays as they are most similar in width for the higher p_T measurements. As shown in figure 7.11, the uncertainty on this background – shown in the horizontal axis – is much higher. This is due to the fact, that the electrons from charm-hadron decays have a distribution width between that of the Dalitz and conversion electrons and the beauty-hadron decay electrons.

The approach of this analysis is to make sure that the uncertainty of the p_{beauty} is not underestimated. This is the case if the contribution from charm is strongly underestimated, which can happen if the uncertainty on the charm yield is large. Such a case can be identified by making use of the fact that if the charm contribution is underestimated, then its uncertainty will be particularly large. To study this effect, another toy model was used for such cases. For this, the charm contribution was artificially increased. This change should typically increase the estimated relative uncertainty of p_{beauty} . The steps of this additional check can thus be summarized as:

1. Analysis of the toy model using the measured values as input.
2. If the quadratic sum of the bias and the *rms* of the charm yield is larger than 0.5 (relative to measured point), additional steps are applied.
3. If the (previously performed) measurement of the ratio of the electrons from charm and beauty hadrons α is larger than 0.5, this value is used, otherwise $\alpha = 0.5$.
4. Modification of the toy model, by increasing the charm contribution until the ratio is equal to the α .
5. Comparison of the *rms* of the original and the additional estimate. The larger value is used for the uncertainties.

This additional estimation only affects the *rms* calculation. This value will be referred to as the the **statistical uncertainty** of the fit procedure. It is important to mention, that it would not be zero even for infinitely large statistics in the data, because it also contains the statistical fluctuations in the Monte Carlo templates. The name is used, because the uncertainties are independent for fits in different p_T -bins before the p_T -unfolding is considered.

It is worth noting that the uncertainty estimation procedure described above is not limited to this particular maximum likelihood estimator, but can also be applied to other estimators. For example, a reasonable result can also be achieved with the χ^2 -based method described in [91].

7.3 Monte Carlo description and associated uncertainties

The signal extraction makes use of the description of the signal and background impact parameter distributions in the Monte Carlo simulations. As a result, its accuracy depends significantly on the accuracy of the representation of the associated effects in the Monte Carlo simulations. This is particularly important for the impact parameter analysis because the signal and all backgrounds have their peak approximately at the same position (compared to e.g. a signal extraction from an invariant mass distribution). Going to higher and higher degrees of accuracy, at some point the description of the simulations will not be perfect. It is of fundamental importance for the analysis to identify all ways in which the simulation may deviate. This can either be a bias in the simulation, which should be corrected, or it can be an uncertainty in some of its parameters. Any such uncertainty should be evaluated and propagated to the final result. If there were a direct comparison of the Monte Carlo templates to data, they would not be needed for the signal extraction, since the templates could just be taken from data. This means, that all evaluations must be indirect. In the following, the different effects will be discussed separately, starting from effects affecting mostly the light meson contributions and proceeding to those affecting mostly the ones from heavy flavors.

7.3.1 Impact parameter resolution

As discussed in section 7.1, the impact parameter distribution for the Dalitz electrons is almost completely determined by the detector resolution. The slim peaks of the distributions for the conversion electrons and electrons from charm-hadron decays mean that these distributions are also affected strongly by the resolution. To gain a first insight into the representation of the impact parameter resolution in the Monte Carlo simulations, it is useful to consider the tracking uncertainties given by the tracking algorithm. Figure 7.12 shows the estimate for the impact parameter resolution given by the tracking algorithm [73] in data and the Monte Carlo simulation for charged particles. The resolution of the impact parameter results from a convolution of the track position resolution and that of the primary vertex. The result shows a difference in expected resolution of about 10% between the data and the Monte Carlo simulations for charged tracks.

The impact parameter resolution differs slightly between charged hadrons and electrons. Electrons typically have a larger energy deposit in the detectors due to the higher

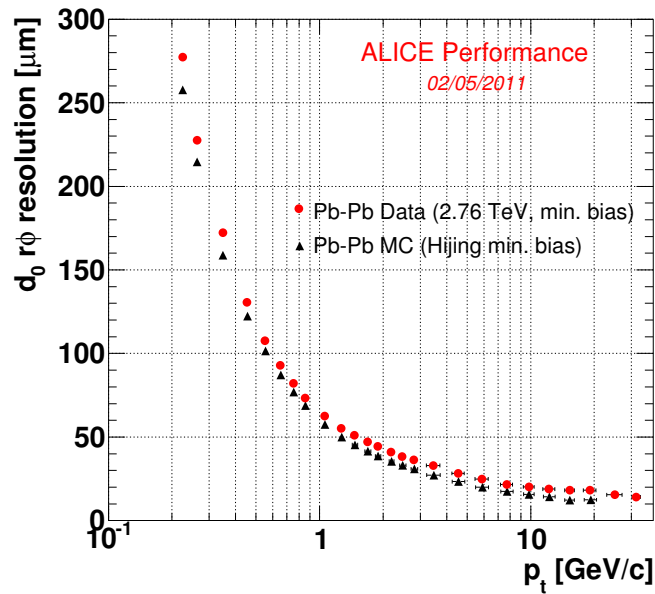


Figure 7.12: Comparison of the impact parameter resolution based on the tracking parameters in data and Monte Carlo simulations. The tracks were required to have a signal in both SPD layers. No centrality selection was applied.

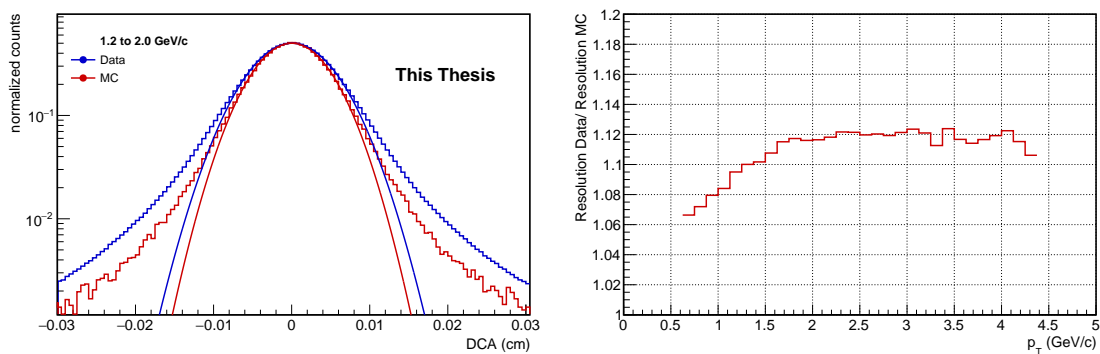


Figure 7.13: *Left*: One p_T -bin of the estimate of the resolution in Monte Carlo simulations and data using a Gaussian model of the peak. *Right*: p_T -dependence of the ratio of the two resolutions.

$\beta\gamma$. They are also affected by Bremsstrahlung, which can affect the resolution. However, the geometric effects, which mostly define the impact parameter resolution, should be the same for both. As it is not possible to obtain a high-statistics sample of pure electrons from the primary vertex (as discussed in chapter 6), the difference in impact parameter resolution must be inferred from charged hadrons. These were selected using the TPC with a requirement of $-8 < n_{\sigma,e}^{\text{TPC}} < -3$, yielding mostly charged pions and kaons.

The impact parameter distributions in data and in the Monte Carlo simulations are shown on the left side of figure 7.13. Apart from a large number of tracks originating from the primary vertex, there is also a significant contribution from secondary tracks. This is apparent from the wide tails of the distributions. The ratio of primary and secondary tracks is not reproduced in the Monte Carlo simulations. The full distribution thus has two contributions: A slim, approximately Gaussian peak with a large number of entries from the primary particles and a wide distribution with much fewer entries from particles that do not originate from the primary vertex. To assess the difference in the width of the distributions, only the former contribution is of interest. This width can be assessed by restricting the analysis to the peak of the distribution, where the contribution of primary particles dominates. A fit of a Gaussian distribution to the peak yields an estimate for the resolution. The fit range was chosen as $(-rms, rms)$, where rms is the root mean square of the full distribution.

The right side of figure 7.13 shows the ratio of the resulting resolution estimates. They are different by about 10% at the low edge of the measured p_T -range (at 1.3 GeV/c) to about 12% for larger transverse momenta. This is consistent with the expectation from figure 7.12. For the correction of this effect, a difference of 10% was assumed with the case of 12% being used to estimate the uncertainty of the correction. If the lower resolution is due to additional fluctuations in the measurement, then it is reasonable to assume that these are approximately Gaussian. This assumption is also very close to the possibility that some effects cause a scaling of the original distribution, because this is approximately Gaussian as well. It is simple to include these additional fluctuations in the Monte Carlo simulations, by adding a Gaussian distributed random value to the reconstructed impact parameter in the Monte Carlo simulations. The approach is based on the assumption that the relative difference of the resolution in data and Monte Carlo simulations is the same for electrons and charged hadrons.

For each particle in a Monte Carlo simulation, the resolution σ_{MC} is estimated from the tracking algorithm as drawn in figure 7.12. A random number is sampled from a

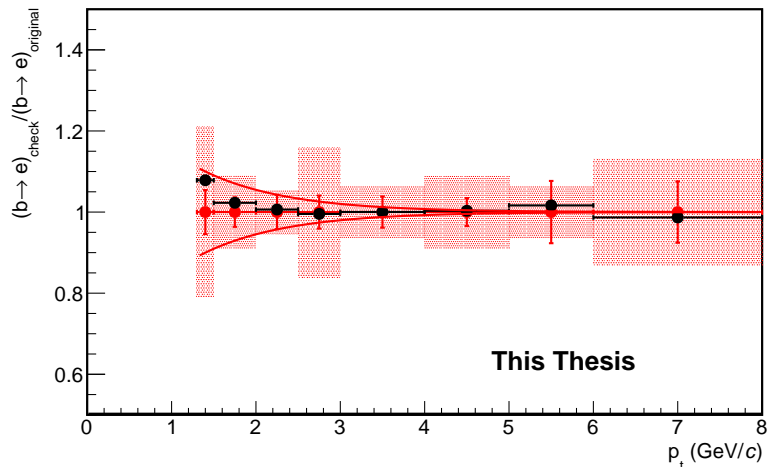


Figure 7.14: Change of the beauty-hadron decay electron spectrum going from an impact parameter resolution correction of 10% to one of 12%. The spectra are divided by the central points of the unmodified measurement. For comparison, the original measurement is also drawn with the statistical and systematic uncertainties. No separate uncertainties are drawn for the result of the check, because they can be expected to be highly correlated. Thus, the effect is significant even though it is smaller than the uncertainties as apparent also by the systematic deviation to values larger than unity.

Gaussian distribution with width σ_{Gauss} , where σ_{Gauss} is defined by

$$\sigma_{\text{MC}}^2 + \sigma_{\text{Gauss}}^2 = ((1 + 10\%)\sigma_{\text{MC}})^2. \quad (7.13)$$

This number is then added to the value of the impact parameter. The resulting resolution is then 10% larger than before.

There is a very interesting additional property of this approach. The Gaussian width is typically larger than the impact parameter bin width by some margin. If, for a single impact parameter correction, the Gaussian were sampled twice, the two corrected values would typically end up in different impact parameter bins. As a result, the distributions within the bins would still be approximately Poisson distributed, but the statistics in the impact parameter template would be doubled. To avoid biases, this approach is not used, but the idea is included indirectly as will be discussed later.

As mentioned before, the uncertainty of the impact parameter resolution correction is estimated by comparing the case of a correction by 10% with the one with 12%. This difference represents the uncertainty in the strength of the correction. Effects due to the uncertainty in the exact form of the resolution correction are most likely smaller. Figure

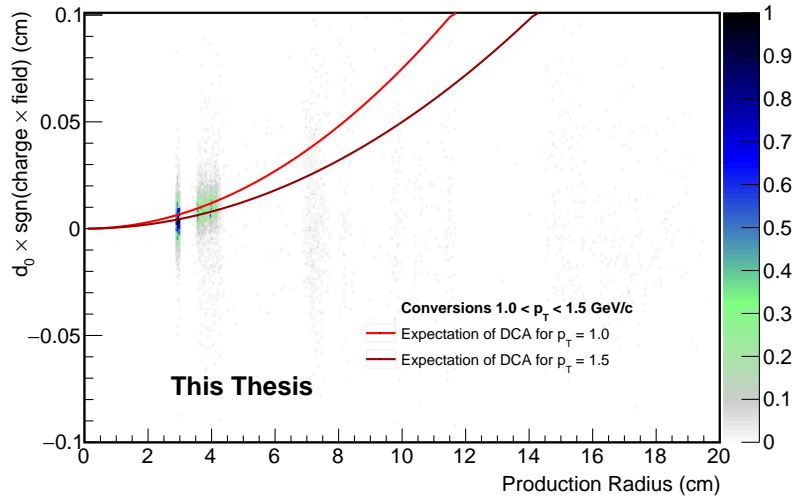


Figure 7.15: Impact parameter distribution of conversion electrons as a function of p_T . The lines give the expected average impact parameter at the p_T of the upper and lower edge of the p_T -bin.

7.14 shows the ratio of the resulting measurement. For all of the comparisons of this chapter, it is difficult to precisely estimate the amount of correlation between the two distributions being compared, making it difficult to understand the significance of the deviations. To maximize the accuracy of the estimate, the two cases were chosen to be as correlated as possible. For the case of the resolution correction, this means that for each track the same random number was used for both cases and scaled accordingly.

The deviations shown in figure 7.14 show similar deviations between adjacent points, pointing to a systematic effect. One exception is the p_T -bin of 5 – 6 GeV/ c , which is interpreted as a statistical fluctuation. The deviation is larger for lower p_T . This is reasonable, given that the distributions are influenced more by the resolution at low p_T (where the resolution is worse) and that the influence of the Dalitz electrons decreases towards higher p_T . The difference can be included within

$$\pm 0.1 * \exp(-p_T(\text{cm}) + 1.4) . \quad (7.14)$$

This was chosen to represent the uncertainty of the impact parameter resolution correction.

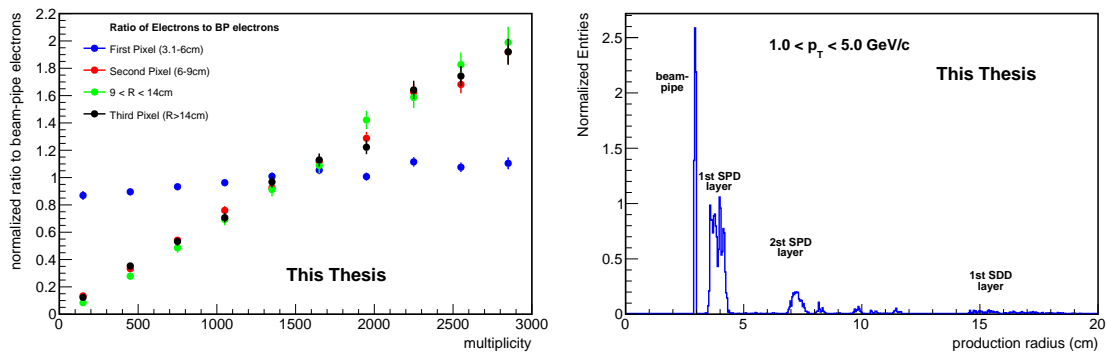


Figure 7.16: *Left*: Ratio of electrons from photon conversions produced within different radial ranges to those produced in the beam-pipe for different multiplicities. To show that the shape of the ratios is similar, the distributions were normalized individually before taking the ratio. The similarity in the shape of the ratios shows the applicability of the uncertainty estimation described in the text. The contribution from the innermost layer of the SPD contains contributions from both reconstructed photon conversions and mismatched conversion electrons and thus shows a different shape in the ratio. The distribution of the production radii (*right*) is reproduced here for convenience. The multiplicity was estimated by the number of particles in the central barrel fulfilling basic tracking requirements.

7.3.2 Mismatched conversion electrons

Figure 7.4 shows the distribution of the production radii of conversion electrons that fulfill the track selection criteria. As previously pointed out, there is some contribution with a production vertex outside the innermost layer of the ITS even though a signal is required there. Figure 7.15 shows the impact parameter distributions of conversion electrons. It is interesting to note that the conversion electrons outside the innermost layer of the ITS (at around 4.5 cm) do not show the R^2 dependence of the impact parameter to the production radius. The reason for this is that the contribution comes from a random association of the electrons with the signal of other particles in the inner layers of the ITS. This leads to a very wide distribution that is nevertheless fairly symmetric around zero. These particles will be referred to as **mismatched conversion electrons** in the following. It is important to ensure that the effect is correctly reproduced in the Monte Carlo simulations because the wide distribution competes with the contribution from beauty hadron decay electrons, particularly in the lower p_T range.

The relative amount of the mismatched conversion electrons compared to the total

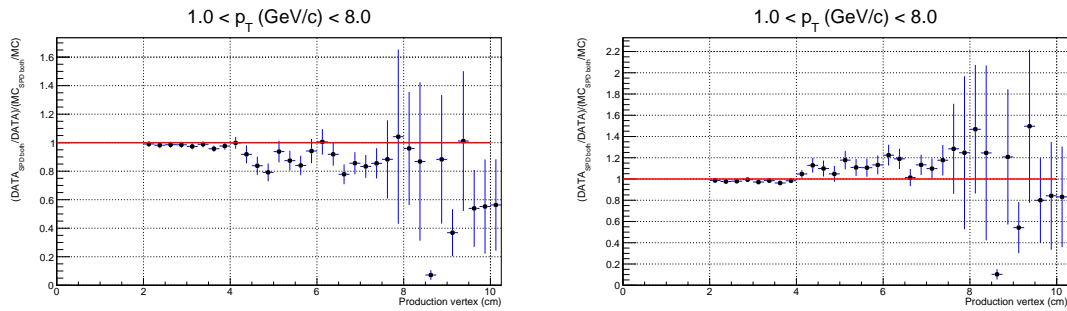


Figure 7.17: Double ratio of amount of V0 pions produced at a certain production radius with and without the requirement of hits in the two innermost layers of the ITS in data and Monte Carlo simulations. *Left*: For a centrality of 0-20% in data and 0-20% in Monte Carlo simulations. *Right*: For a centrality of 0-20% in data and 0-60% in Monte Carlo simulations. (Plots from [100])

number of conversion electrons depends on the particle multiplicity. The more signals there are in the inner layers of the ITS, the larger the possibility for a mismatch. Within the usual multiplicities of the Pb–Pb collisions, the effect is close to proportional as shown in figure 7.16. The number of conversion electrons produced in the first pixel (blue markers) does not show this proportionality because it has contribution from conversion electrons that are mismatched and such that are not. It is not possible to separate the contributions based on the production radius alone. The sum of the two effects creates a linear dependence instead of a proportionality. It is not feasible to estimate the effect using the V0 electrons. The reason for this is that the resolution of the production radius is low due to the small opening angle of the electron-positron pair [95]. In addition, the V0 electrons contain contributions not just from hadrons but also from Dalitz electrons, which would have to be disentangled.

As a first step, it is interesting to know whether the contribution is over- or underestimated by the Monte Carlo simulations. This can be examined indirectly, making use of the V0 pions instead. The same effect can happen here. The advantage is that the production radius can be measured more accurately. Figure 7.17 (left) shows the comparison of the mismatched conversion in data and the simulations. As for the conversion electrons, the particles produced within the active area and the beam pipe should create tracks associated with their signals, while those outside only survive the track requirements by random misassociation. One difference of the kaons compared to the photons is that the distribution of their decay vertices depends on their p_T -spectrum. Thus, it is not possible to compare the radial distributions of the V0 pion production radii directly. Instead, the efficiency of the requirement of signals in the innermost two layers of the

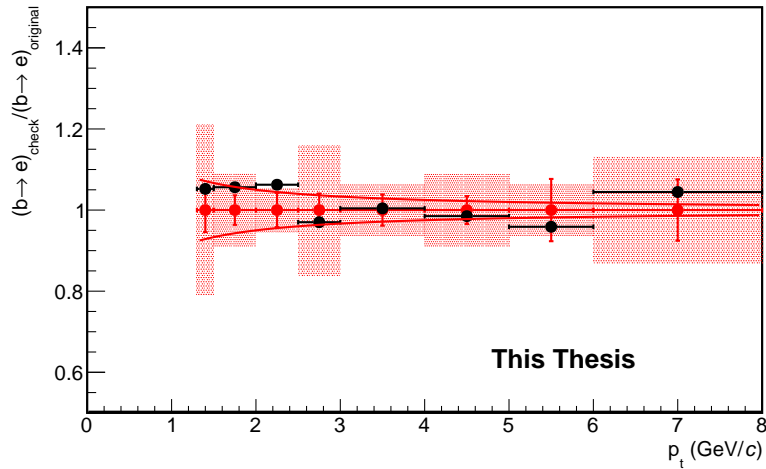


Figure 7.18: Change of the beauty-hadron decay electron spectrum using a conversion electron template with a larger centrality range.

ITS is compared. As shown in figure 7.17 (left), there are more misassociations in the simulations compared to data.

This suggests that the Monte Carlo simulations in the centrality 0-20% overestimate the amount of mismatched conversion electrons. Given the multiplicity dependence of the effect, it is useful to compare to a sample with a lower average multiplicity as well. The right plot in figure 7.17 shows the comparison with a larger centrality range of 0-60% in the Monte Carlo simulations. In this case, the amount of mismatched V0 pions and thus also mismatched conversion electrons is underestimated instead. Thus, the two plots represent extreme cases. Comparing the signal extraction with a conversion electron template of either case gives an estimate of the uncertainty of the representation of the effect. This is possible only with the knowledge, that the contributions to the mismatched conversion electrons from the different production radii all behave similarly with the multiplicity as shown in figure 7.16. In fact the effect is close to proportional to the multiplicity. Figure 7.18 shows the change in the extracted beauty-hadron decay electron spectrum. The change is of the order of

$$\pm 0.1/p_T(\text{cm}) , \quad (7.15)$$

which was used to represent the systematic uncertainty associated with the representation of the mismatched conversion electrons.

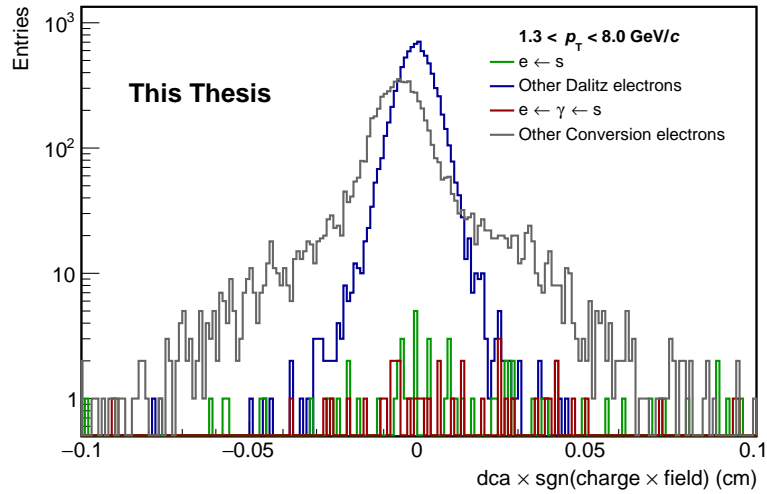


Figure 7.19: Impact parameter distribution of the contributions from strangeness to the Dalitz and conversion electron templates in Monte Carlo simulations.

7.3.3 Strangeness

The so-called Dalitz electrons also contain contributions from the decay of particles containing strange quarks (mainly kaons) as discussed in section 7.1. These have a very wide distribution of the impact parameter due to the long lifetime of the strange hadrons. A similar effect also appears for conversion electrons from photons that come from the decay of strange particles. Figure 7.19 shows the different contributions in the Monte Carlo simulations. While the total contribution is very small in the fit range (-0.1 to 0.1 cm), the distributions are very wide. The influence of this contribution is closely connected to the ratio of strange mesons to light mesons. The representation of this ratio in the Monte Carlo simulations can be estimated by comparing to the ratio of charged particles.

Figure 7.20 shows the ratios of light hadrons. At low p_T , the ratio of charged kaons and charged pions shows approximately linear growth to a value of 0.5 at $p_T = 2$ GeV/ c . The corresponding ratio in the Monte Carlo simulations (figure 7.21) is about a factor of 2 lower at low transverse momentum. To estimate the uncertainty of the measurement due to this effect, the result of the signal is compared with the result after increasing the contribution of strange particles to the Dalitz and conversion electron templates by a factor of 2.

It is not easily possible to vary the amount of electrons from strange hadrons in the Dalitz and conversion electron templates because a weighting procedure would re-

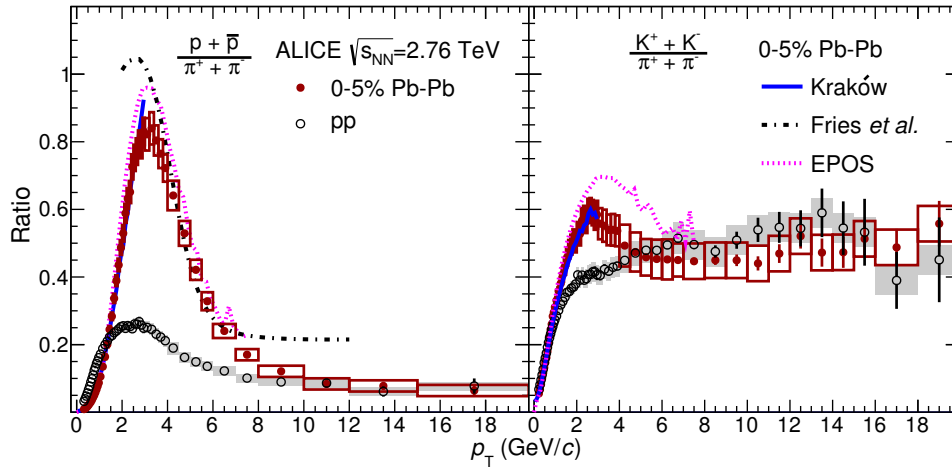


Figure 7.20: Charged particle ratios in Pb–Pb collisions (figure taken from [35]).

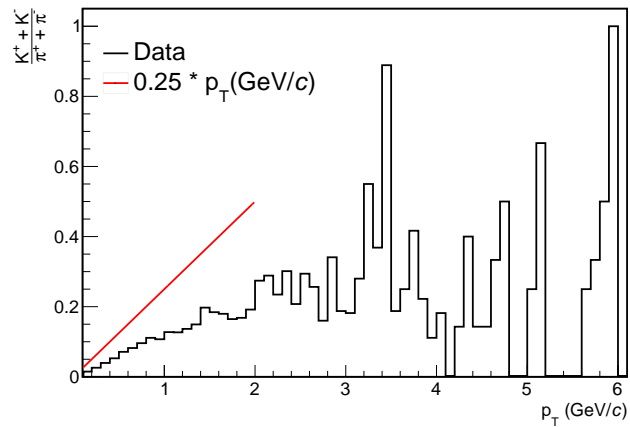


Figure 7.21: Ratio of charged kaons and pions in Monte Carlo simulations.

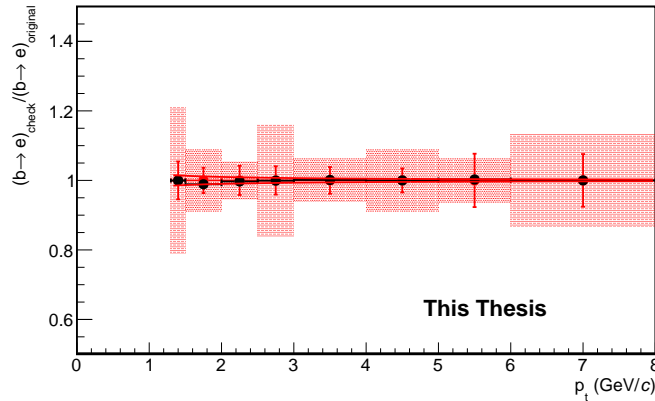


Figure 7.22: Change of the extracted beauty-hadron decay electron spectrum when doubling the influence of electrons from the decays of strange hadrons in the Dalitz and conversion electron templates.

sult in a likelihood that is not Poissonian anymore. This problem can be solved formally by introducing separate templates for the contributions from strangeness and the other contributions. The additional two templates do however increase the dimensionality of the maximization problem (as discussed in section 7.2). The condition $p_{\text{Dalitz,noStrangeness}} = p_{\text{Dalitz,Strangeness}}$ and $p_{\text{Conversion,noStrangeness}} = p_{\text{Conversion,Strangeness}}$ should be equivalent to using the original distributions. However, there are 400 additional free parameters in the A_{ji} s. The results from this approach are the same as with the lower dimensionality, although the maximization is computationally much more expensive. It is now easy to estimate the dependence on the ratio of the electrons from the decays of strange particles by requiring $p_{\text{Dalitz,Strangeness}} = 2 \cdot p_{\text{Dalitz,noStrangeness}}$ and $p_{\text{Conversion,Strangeness}} = 2 \cdot p_{\text{Conversion,noStrangeness}}$. The resulting change in the measured spectrum of electrons from beauty-hadron decays is shown in figure 7.22. The very small effect is estimated with the function

$$\pm 0.02/p_T(\text{cm}) . \quad (7.16)$$

This was used to represent the uncertainty of the contributions from strangeness to the Monte Carlo templates.

7.3.4 Hadron contamination

The significant hadron contamination (as discussed in chapter 6.3) has a surprisingly small effect on the measurement. To understand this, it is useful to consider the impact

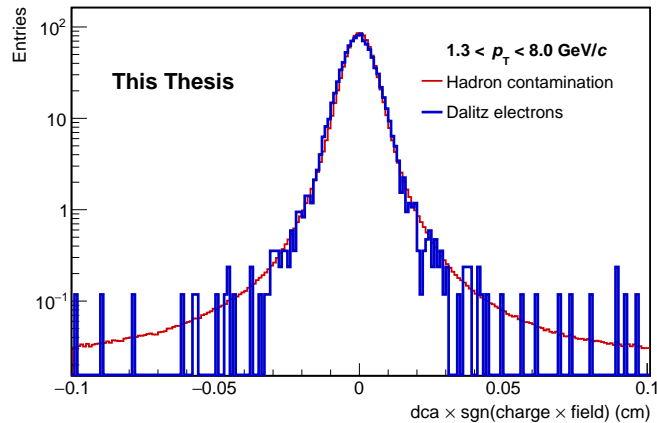


Figure 7.23: Comparison of the impact parameter distribution of the Dalitz electrons in Monte Carlo simulations and charged pions in data.

parameter distribution of the contaminating hadrons, which mostly consist of pions. Due to their abundance, such a template can be obtained from data. It is selected with the TPC signal requirement $-5 < n_{\sigma,e}^{\text{TPC}} < -3$. Due to the fact that the template comes from data, no resolution correction needs to be applied.

Figure 7.23 shows a comparison of the impact parameter distribution of Dalitz electrons from Monte Carlo simulations and of the charged pions in data. The two distributions are very similar because in both cases most particles originate close to the primary vertex. This means that the difference in the shapes is mostly due to the different resolutions of electrons and hadrons. As a result, the signal extraction procedure should include much of the hadron contamination in the measured Dalitz electrons.

In the lower p_T -ranges, the contribution of the Dalitz electrons to the inclusive electron sample can be expected to be relatively large. Going to higher transverse momenta, the electron contribution is mostly due to heavy flavor decays. As a result, the hadron contamination can be expected to be dominating compared to the Dalitz electrons. To estimate the uncertainty due to the unknown hadron contamination, it is again useful to compare the two extreme cases: Using a Dalitz electron template and using the hadron impact parameter template instead in the signal extraction. As the difference between the two results is small, it is reasonable to assume that all intermediate cases of the template should also give a result in between. Figure 7.24 shows the change in the measurement. The difference is interpolated using the function

$$\pm 0.1/p_T(\text{cm}) . \quad (7.17)$$

For the central values, the Dalitz electron template was used for the lower p_T -bins. For

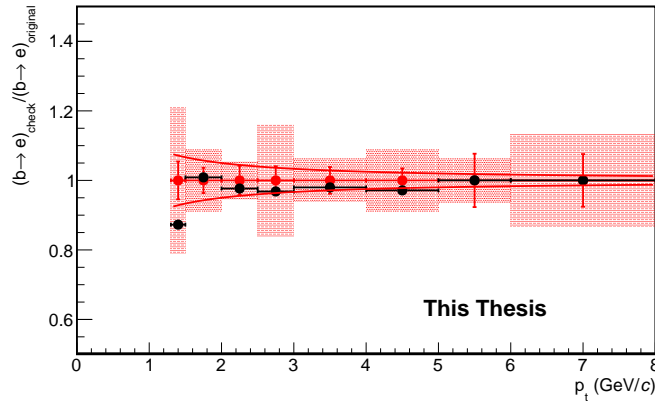


Figure 7.24: Change of the extracted spectrum of beauty-hadron decay electrons by replacing the Dalitz electron impact parameter template with the one for charged pions.

$p_T > 5 \text{ GeV}/c$, the template for charged hadrons was used instead. As the contamination should dominate there and the statistics for the Dalitz electrons are very low, it was assumed that the associated uncertainty should be below the function given above.

7.3.5 Momentum distribution of the heavy-flavor hadrons

The beauty-hadron decay electrons of a given p_T -bin can originate from beauty hadrons in a large transverse momentum range, as shown in figure 5.1 (right). Their average production radius depends on the $\beta\gamma$ of the beauty hadrons. In turn, this also influences the impact parameter distribution of the electrons. Qualitatively, the impact parameter distribution is wider if the beauty hadron spectrum falls more slowly with p_T and narrower if it drops more quickly. This means, that the impact parameter distribution for the beauty-hadron decay electrons depends on the spectrum of the beauty hadrons, which is not known before the measurement. A similar reasoning also applies to the electrons from charm-hadron decays. The treatment of the correction and the estimate of the systematic uncertainties differs slightly due to the availability of the D meson measurements [69].

Charm hadrons The approach to the case of the charm hadrons is to make use of the information of the D meson measurements. Their absolute yield is not relevant for this effect because of the free amplitude parameters of the fit procedure. The measurement of the D^0 -mesons has the largest p_T range in the measurement [69]. For this reason, it was used for the comparison. Figure 7.25 (left) shows a comparison of the measured

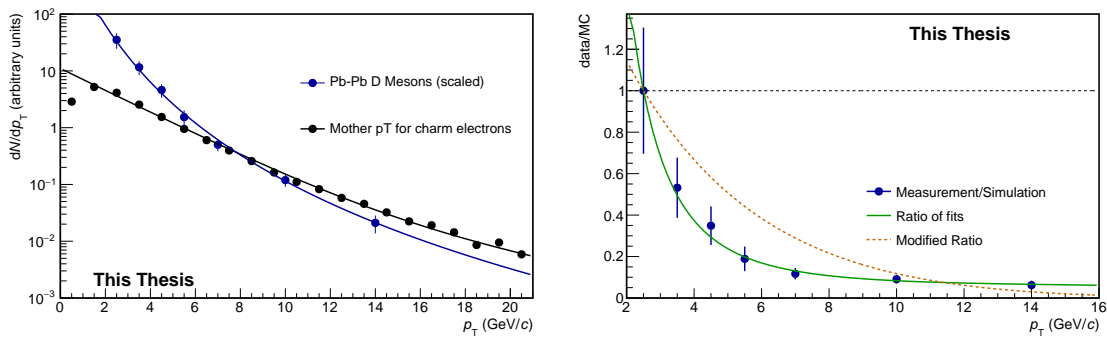


Figure 7.25: *Left*: p_T -spectra of the measured D^0 -mesons [69] and the mother particles of charm-hadron decay electrons in Monte Carlo simulations. *Right*: Ratio of the measurement and the simulations with ratio of the fits. The modified correction function for the uncertainty estimation is also given.

D^0 -meson spectrum and the p_T -distribution of the mother particles of the charm-hadron decay electrons. The distributions differ strongly between the PYTHIA simulation with a Perugia-0 tune and the measurement. The D^0 meson p_T -spectrum was interpolated by a shifted power law:

$$\frac{d\sigma}{dp_T} \sim (p_T + \alpha)^\beta, \quad (7.18)$$

while the distribution from Monte Carlo simulations was interpolated by the sum of two exponential functions as shown in figure 7.25 (left). The ratio (on the right) of the two gives the appropriate correction factors. It is interpolated well by the ratio of the two fit functions. The necessary correction is fairly large. For this reason, it is particularly important to investigate the assumptions made with this approach. Is it reasonable to compare only to the D^0 -measurement and how problematic is the extrapolation to transverse momenta below 2 GeV/c?

The question of how representative the D^0 -measurement is can be split into two parts. One is the possibly different yield of the different charm-hadron species between the simulations and the measurement. This is the lowest order effect, given that the absolute yield of charm hadrons does not play a role. It will be discussed separately in the next subsection (7.3.6). There is a smaller influence from the shape of the spectrum of the different mesons. However, these shapes do seem very similar [68] for central Pb–Pb collisions. Accordingly, the effect can be expected to be negligible compared to the uncertainties of the estimate of the correction. The effect of the extrapolation to low transverse momentum can be investigated by varying the extrapolation within reasonable limits. It turns out, that even a strong change, such as setting the ratio to

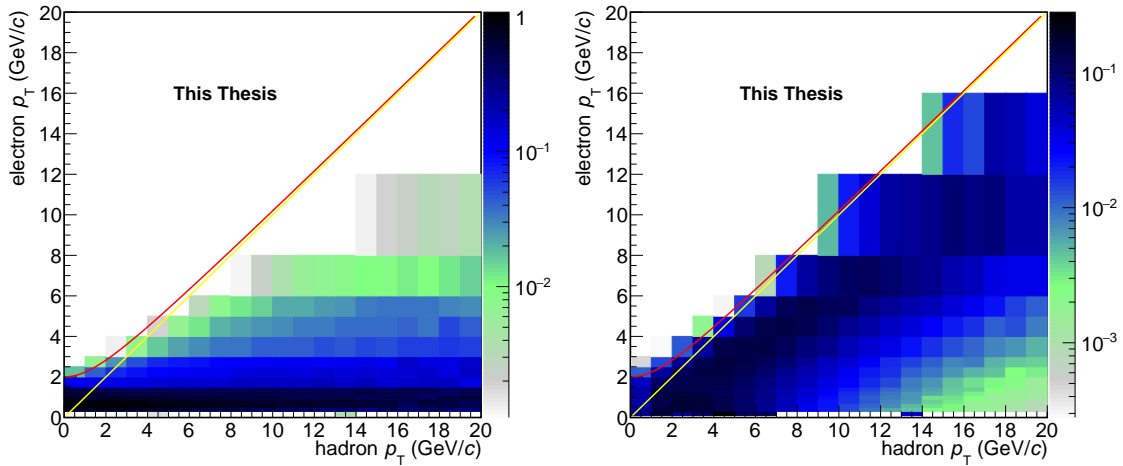


Figure 7.26: p_T -distributions of charm hadrons and the daughter electrons in Monte Carlo Simulations. *Left*: For a given hadron p_T . *Right*: For a given electron p_T . The red line shows the electron p_T assuming it receives all energy of a $2 \text{ GeV}/c^2$ mother particle. The yellow line is the diagonal.

zero below $2 \text{ GeV}/c$ affects the measured points less than the effect of the uncertainty of the slope due to the uncertainties of the D^0 -measurement. The reason for this is that the charm hadrons usually have a larger momentum than the electrons, meaning that the variation affects only a small part of the contribution. Additionally, the impact parameter distribution does not change very rapidly with the transverse momentum.

A weighting procedure for the charm hadron decay electrons would make the underlying probability distribution non-Poissonian. To circumvent this, a statistical correction was chosen. Charm-hadron decay electrons were removed statistically with a probability depending on the transverse momentum of the mother particle. The quick drop of the ratio means, that such a correction would decrease the statistics significantly. To improve upon this, it is useful to remember that there is a freedom in the normalization of the ratio – any multiple can also be used. Figure 7.26 (right) shows that almost all mother particles have transverse momenta larger than their daughters. This suggests correcting with a different rule for each p_T -bin. With $r(p_T)$ being the ratio function, a constant α is chosen such that $\alpha r(p_T) = 1$ at the transverse momentum of the lower edge of the electron p_T -bin. Each electron is rejected with the probability $1 - \alpha r(p_T)$. If this is lower than zero, the particle is always accepted. This procedure results in a correction of the charm-hadron p_T -distribution, while keeping the Poisson statistics intact and without decreasing the sample size too much.

The main source of uncertainty for this correction is in the measurement uncertainties of the D mesons. The measurement contains statistical uncertainties, which are uncorrelated from one p_T -bin to the next and systematic uncertainties, which may be correlated to some unknown degree. As the main effect comes from the slope, the largest effect would come from those points within the uncertainties that change the (local) slope the most. The effect can be expected to be the largest at low transverse momenta. Thus, the following extreme case was used for comparison: In the first p_T -bin, statistical and systematic uncertainties of the measurement were added and subtracted from the central point. The second measured bin was left untouched and in the third, the uncertainties were added. Then, an exponential function was fitted, considering only these three points. The result gives an estimate of the strongest deviation at low momenta that is still compatible with the uncertainties of the D meson measurement. This variation of the correction is also shown in figure 7.25 as the red dashed line. The effect was determined together with the corresponding effect for the beauty hadrons and will be discussed there.

Beauty hadrons It is not possible to use the same approach in the corresponding case for the beauty hadrons. The measurement of beauty-hadron decay electrons has the purpose of providing information about the beauty hadron and the beauty quark momentum distributions. Thus, this information is not available prior to the measurement. Instead, the approach is to estimate how sensitive the estimated yield of the beauty-hadron decay electrons is to a reasonable range of possible beauty-hadron p_T -distributions. As for the charm-hadron case, the correction has a free scale parameter due to the free amplitude parameter of the signal extraction. An additional advantage is the fact that the representation of the beauty hadrons by PYTHIA with the Perugia-0 tune is much better than that of the charm hadrons. For the charm case, there is already a large difference to the proton-proton collision measurement [101]. In the case of the beauty hadrons, the measurement of beauty-hadron decay electrons in p-Pb collisions [46] agrees well with the corresponding enhanced Monte Carlo simulations. Different from the previous case, this means that the effect is mostly due to the influence of the medium and the necessary correction is thus smaller. The influence of the medium is to slow down particles faster than the medium and to accelerate those at lower velocities.

The correction factor is thus proportional to the R_{AA} . A generic expectation is that it decreases from low to intermediate p_T . The effect on the impact parameter distribution does not depend on the scale and also depends little on the small scale structure. The main influence is due to the change in the slope. For that reason, the

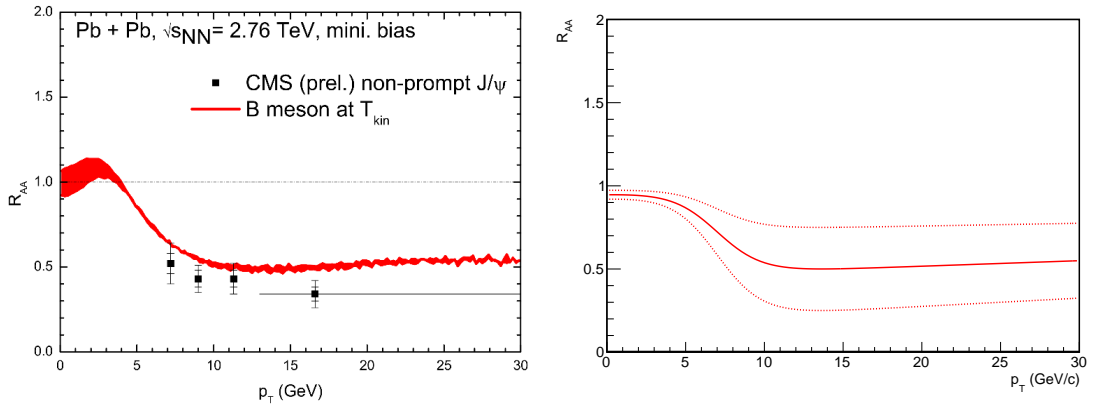


Figure 7.27: *Left*: TAMU model prediction for the B meson R_{AA} . *Right*: Interpolation used for the correction with the variations used for the uncertainty calculation.

approach is, to use a model of the R_{AA} to determine the impact parameter distribution for the central values of the fit and generously vary the slope to estimate the uncertainty due to the effect of the p_T -distribution of the beauty-hadrons. For the central value, the result of a theoretical calculation was considered. The TAMU model [66] was chosen for this purpose, as its behaviour is fairly typical when compared to other predictions (this is discussed in chapter 9). The result shows values close to one at low transverse momenta and falls off quickly between 5 and 10 GeV/c. At large transverse momenta, the R_{AA} rises slowly. The function

$$0.5 / (1. + \exp((p_T[\text{GeV}/c] - 7.) \cdot 0.7)) + 0.5 + (p_T[\text{GeV}/c] - 15.) / 300 \quad (7.19)$$

was used to describe its general shape and to define the central points of the correction as shown in figure 7.27 as the central red line. The statistical correction was done in a similar way as for the charm case, excluding the step of separating the correction for each p_T -bin. Figure 5.1 shows that the assumption of the hadron p_T being larger than the electron p_T is not as good at low transverse momentum due to the larger mass of the hadrons.

In both cases, the variation checked, changed the p_T -distribution towards a smaller slope. Both variations individually change the resulting beauty-hadron decay electron yield towards smaller values. Due to the comparatively large statistics of the beauty-hadron decay electrons in the enhanced Monte Carlo sample, the opposite as also attempted for the beauty case as shown in figure 7.27 (right). This resulted in a similar but opposite effect. As the effect is dominated by the uncertainty of the beauty hadron p_T -distribution, both variations were combined to give the variation shown in figure 7.28. The largest effect appears at low transverse momentum as expected from the variation.

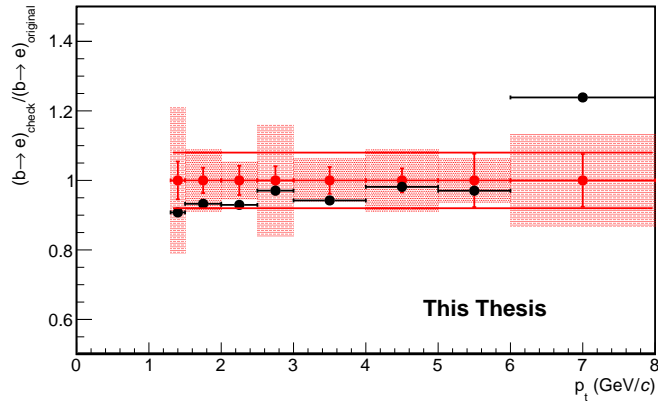


Figure 7.28: Change of the extracted spectrum of beauty-hadron decay electrons by changing the correction for the beauty and charm hadron p_T -distributions.

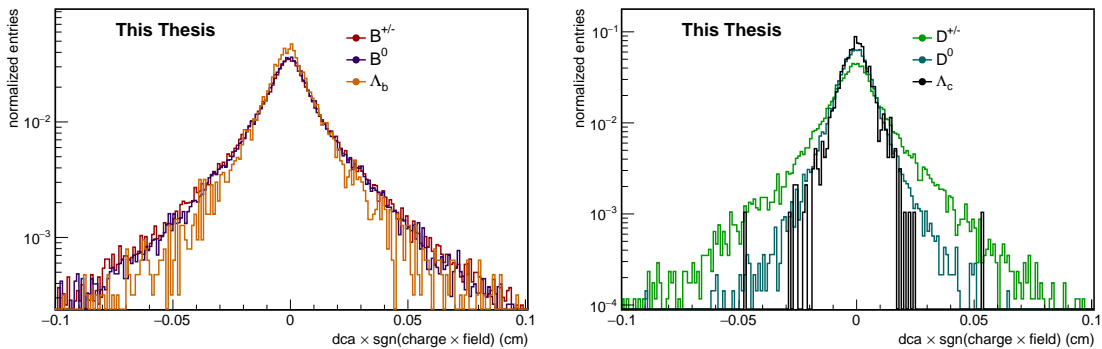


Figure 7.29: Comparison of the impact parameter distributions of electrons from different hadron species in the enhanced Monte Carlo simulations in the p_T -interval $1.3 - 8 \text{ GeV}/c$. *Left*: for the case of beauty hadrons. *Right*: for the case of charm hadrons.

Given the abrupt change, the deviation of the highest p_T -bin is most likely due to statistical fluctuations. As visible in figure 7.27, at high transverse momentum the two cases have the same slope but different statistics. Considering that the position of the sudden drop in the R_{AA} (in the TAMU model between 5 and $10 \text{ GeV}/c$) is not known, it is prudent to expect that an effect of similar size might also appear at slightly larger transverse momenta. For this reason, a constant uncertainty of the largest deviation was assumed. This uncertainty was taken to be 8% .

7.3.6 Baryon ratio

Thus far, the charm hadrons and beauty hadrons have been treated as a single contribution each. Actually, several different species of hadrons contribute in both cases, with their exact relative abundances not perfectly known. The uncertainty in the relative abundances translates into an uncertainty of the impact parameter distributions of the decay electrons if their impact parameter distributions are different. Figure 7.29 shows the impact parameter distributions for heavy-flavor decay electrons from different species of beauty and charm hadrons. The distributions for the beauty-hadron decay electrons appear fairly similar to each other. Those for the charm hadron decay electrons differ more strongly. This is unsurprising, given the larger variance of the decay lengths in the charm case as shown in table 5.1.

The space of possible ratios is large. To gain a general understanding of the effects of the hadron species ratios, different variations are compared. Similar as in the case of the hadron p_T -distribution in the previous section, the effect does not depend on the absolute yield of the hadrons, but only on their relative contributions, due to the free amplitude parameters of the fit. To estimate the magnitude of the difference in hadron species ratios, the ratios in the templates were compared to the expectations from the thermal model [42] as calculated in [102]. The differences are particularly large for the Λ_c and Λ_b baryons, which are higher than PYTHIA by factor of about 2.5 and 2 respectively. The differences for the mesons are of the order of a few 10%.

Considering the impact parameter distributions given in figure 7.29, no large effect can be expected from a change in the ratio of the B^0 and B^\pm because their distributions are very similar. The effect of a change in the ratio of the Λ_b can be interpreted by considering the different ranges of the impact parameter in the signal extraction. The main information about the beauty contributions comes from the tails of the distribution, where there is little background. Closer to the peak, the beauty-hadron decay electrons contribute less than the more strongly peaked background distributions. If the template contained a larger contribution from the Λ_b , this contribution would be hidden behind the background to some extent. As a result, the fit in the tails would give the same result, but integrating over the distribution to obtain the total yield would result in a larger value. For the Λ_c , the same principle applies. However, in that case there is little influence on the measured yield for the beauty-hadron decay electrons. The D^0 s are an intermediate case. In practice it turns out, that the distribution is already fairly similar to the distribution of the Dalitz electrons and the effect of a variation even of a factor 1.5 is small compared to the influence of the baryon ratios.

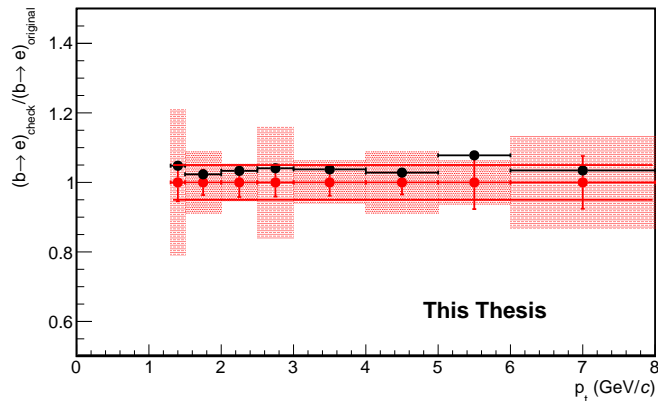


Figure 7.30: Change of the extracted spectrum of beauty-hadron decay electrons after increasing the baryon ratio by a factor of 3.

The estimation of the influence of the effect was done in a similar manner as the analysis of the strangeness ratio described above: The template for the beauty-hadron decay electrons was split into a contribution from e.g. the Λ_b and the rest. Then, the signal extraction was performed with the additional template and the condition $p_{\Lambda_b} = \alpha p_{\text{other beauty}}$. The same was also done for charm. Given, the large uncertainties of the baryon ratio, the uncertainty due to this effect was estimated by comparing to an increase of the baryon ratio by a factor of 3 for both the charm and the beauty case. The result is shown in figure 7.30. The effect is of the order of 5%. Decreasing the ratio even to zero has a smaller effect.

The different systematic uncertainties related to the measurement and their effects on the measurement are summarized in table 7.1. They are assumed to be mostly uncorrelated and thus summed in quadrature.

7.4 Averaging procedure for the fluctuations of the resolution correction

The approach to the resolution correction described in section 7.3.1 introduced additional information to the impact parameter distributions: The full distributions are the convolution of the distributions in the Monte Carlos simulations and a correction function that was assumed to be Gaussian. For the finite number of entries in the templates, this was applied by adding a random number sampled from a Gaussian of appropriate width as described in section 7.3.1. The fact, that the full distribution comes from a

Effect	Uncertainty at $p_T = 1.3 \text{ GeV}/c$	Uncertainty at $p_T = 8 \text{ GeV}/c$
Resolution correction	11%	0.01%
Mismatched conversion electrons	8%	1%
Strangeness	2%	0.3%
Hadron contamination	8%	1%
Mother particle p_T -distribution	8%	8%
Baryon ratio	5%	5%

Table 7.1: Uncertainties of different effects propagated to the measurement. In the analysis, the interpolation functions are always evaluated at the p_T -bin center.

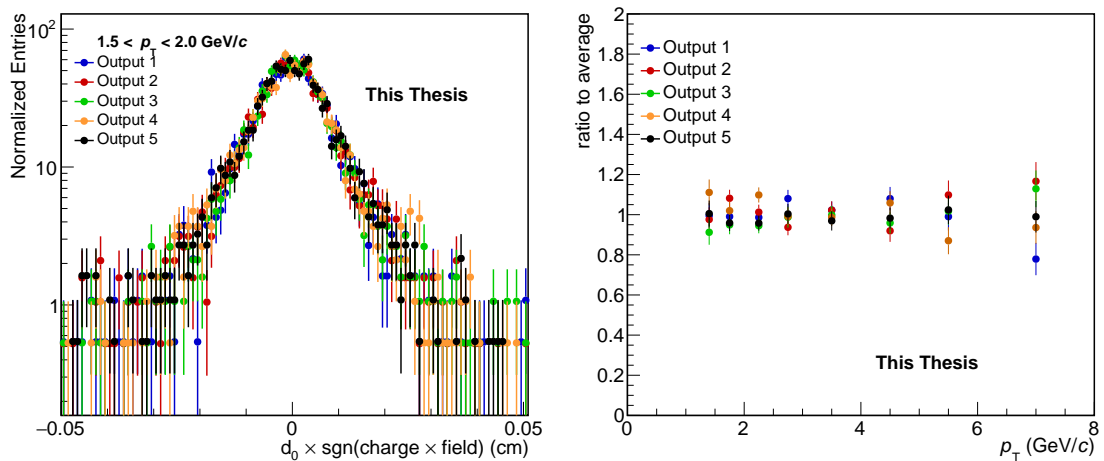


Figure 7.31: *Left*: Impact parameter templates for electrons from charm-hadron decays with different seeds for the random-number generator of the impact parameter correction. *Right*: Ratio of the resulting extracted p_T -distributions of the electrons from beauty-hadron decays.

convolution means that it has to be smooth at least on that scale. This knowledge can be used to decrease the effect of the statistical fluctuations in the impact parameter templates. One approach would be to sample the Gaussian several times, which increases the entries in the corrected template. Due to the fact that two samples can still fall into the same bin and due to the resulting correlations between the bins, this would make the resulting likelihood much more complex and possibly introduce an additional bias. Instead, creating several templates independently does not. Figure 7.31 (left) shows the resulting distributions for electrons from charm-hadron decays for this approach.

To average over the fluctuations, 5 separate sets of templates were created for electrons from charm- and beauty-hadron decays. The signal extraction was performed using each pair separately. The results show some fluctuations but can also be expected to be correlated to some unknown extent. The average of the different estimates has a decreased statistical uncertainty. Within the framework of the uncertainty estimation the exact size of the decrease of the statistical uncertainty is not known. In addition, the different estimates can contain a different contribution of the systematic effects. In all cases, the average shown in figure 7.31 (right) gives a better estimate of the true value. For the final result, the average was used for the central points while the uncertainties were taken from one individual contribution.

Chapter 8

Unfolding

Most of the uncertainties and statistical fluctuations discussed so far, concern the estimation of the contents of a particular p_T -bin. In addition, the measured value of the transverse momentum itself also has an uncertainty. A particle with a reconstructed momentum near the edge of one bin might have a true momentum in the adjacent bin. A similar effect occurs also for the pseudorapidity measurement. Due to the good resolution of the polar angle and the fairly flat distribution at the edge of the considered range $|\eta| = 0.8$, the number of particles migrating into and out of the measured η -range approximately cancel out. The same cannot be expected for the transverse momentum because of the steeply falling p_T -distribution.

Alternatively, the task might be formulated this way: Given the distribution in the measured transverse momentum ($p_{T,\text{measured}}$), what is the distribution in the true transverse momentum ($p_{T,\text{true}}$)? This is called an unfolding of the p_T -distribution. The two quantities are connected via the response function $R(p_{T,\text{measured}}|p_{T,\text{true}})$, which is the probability density function for measuring a certain $p_{T,\text{measured}}$ given $p_{T,\text{true}}$. It defines the resolution of the p_T -reconstruction. Typically, the measured value is smeared out around the true value by the response. This has two important consequences: Firstly, the finite resolution of the momentum reconstruction by the detectors is associated with a loss of information about the true distribution. Thus, when the effect is corrected for, the uncertainties of the distribution should increase. Secondly, it should be problematic to view the unfolded distribution at scales smaller than the resolution. To simplify the approach used in this analysis, the discussion is separated into two parts. In the first part, the unfolding problem will be discussed for an idealized example to clarify the basic approach. The second part serves to explain the particular case of the measurement of beauty-hadron decay electrons and a measurement in a finite p_T -range.

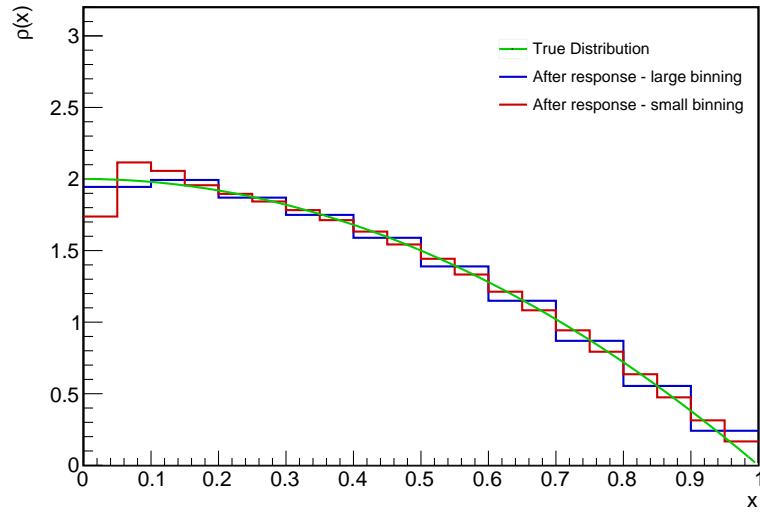


Figure 8.1: Example of distribution, which is binned and then folded

8.1 Solution for an idealized problem

An example for the distribution of a measured value can be found in figure 8.1. The green line shows the true distribution of some variable x that is being measured and which can have values between zero and one. With a finite resolution of the measurement, the distribution of the measured value will be different from the true one. Two examples are plotted as the blue and red lines, which correspond to cases of different binnings.

The response function for electrons from beauty-hadron decays can be approximated using detector simulations. Figure 8.2 shows the responses used in the example of figure 8.1 with two choices of the binning. The measured x -distribution (or p_T -distribution) ρ_{measured} is connected to the true distribution by a convolution:

$$\rho_{\text{measured}}(x_{\text{measured}}) = \int_0^{\infty} R(x_{\text{measured}}|x_{\text{true}})\rho_{\text{true}}(x_{\text{true}})dx_{\text{true}} \quad (8.1)$$

The unfolding problem is the problem of inverting this equation.

For a practical application, three additional complications arise: Firstly, the distribution $\rho(x_{\text{measured}})$ is not actually known, as the measurement is performed using finite-width x -bins. This can be taken into account by using the same binning also for the response, which transforms it into the response matrix. The response matrix is a good approximation of the response, if the bin widths are sufficiently small to have the mean value represent the function values in this range. As a result, eq. 8.1 is transformed into the matrix equation [103]:

$$\vec{x}_{\text{measured}} = \hat{R} \vec{x}_{\text{true}} , \quad (8.2)$$

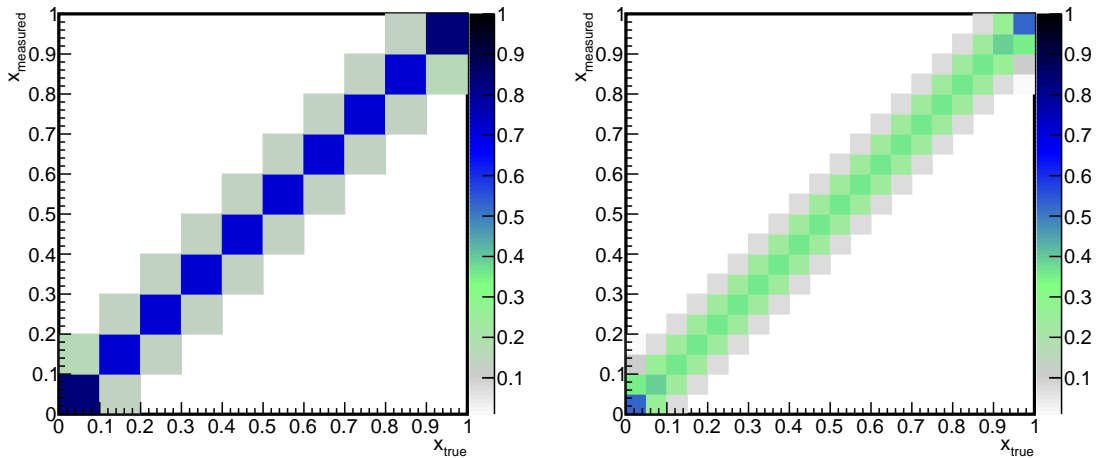


Figure 8.2: Example response matrices. The underlying distribution is a Gaussian with a width of 0.055 - slightly larger than the binning of the smaller case.

where $\vec{x}_{\text{measured}}$ and \vec{x}_{true} are vectors of the bin contents x_i of the distributions while \hat{R} is the response matrix. It is not necessary to use the same binning for the measured and true distribution. However, if the number of bins is different, the inversion of the process is not as straightforward. In this form, the matrix has a slight dependence on the slope of the distributions in the simulations used to estimate the response matrix, which will decrease with smaller binning. For the beauty-hadron decay electron analysis, the measured p_T -range is finite, giving information only about part of the probability distribution. This will be discussed in the next section. Additionally, the measured distribution will have statistical fluctuations and systematic uncertainties, which affect the unfolding procedure and which also have to be propagated.

Using Bayes' theorem, the posterior probability for the binned problem is:

$$P(\vec{x}_{\text{true}}|\vec{x}_{\text{measured}}) = \frac{P(\vec{x}_{\text{measured}}|\vec{x}_{\text{true}})P(\vec{x}_{\text{true}})}{P(\vec{x}_{\text{measured}})}, \quad (8.3)$$

where the likelihood $P(\vec{x}_{\text{measured}}|\vec{x}_{\text{true}})$ follows from equation 8.2. Assuming a flat prior and Gaussian uncertainties, the unfolded uncertainties will again be Gaussian and the central points can be obtained by inverting the response matrix:

$$\vec{x}_{\text{true}} = \hat{R}^{-1} \vec{x}_{\text{measured}}. \quad (8.4)$$

The uncertainties can be obtained by propagating the covariance matrix through the inverse response matrix [103]:

$$(\sigma_{\text{true}})_{i,j} = \sum_k \sum_l (R^{-1})_{i,k} (R^{-1})_{j,l} (\sigma_{\text{measured}})_{k,l}, \quad (8.5)$$

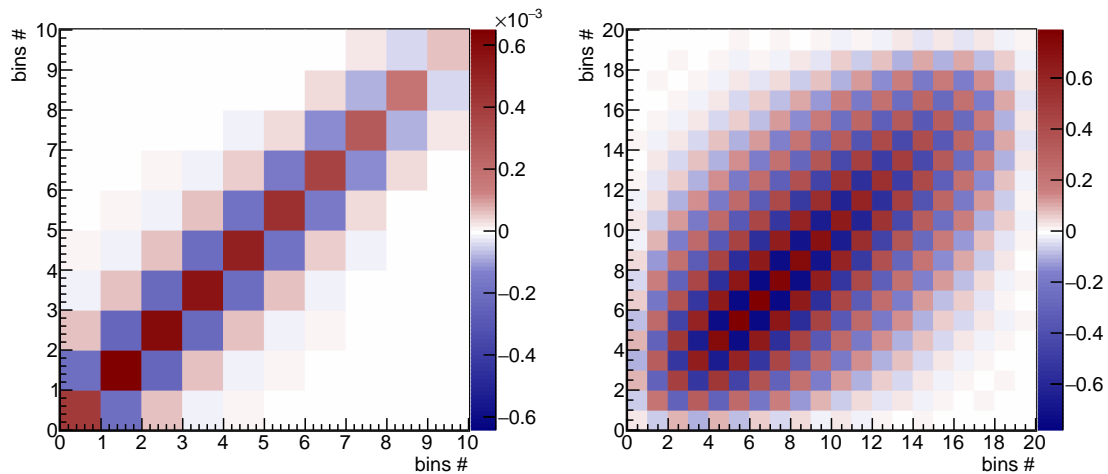


Figure 8.3: Example covariance matrices. The bins smaller than the resolution lead to entries three orders of magnitude larger with large anticorrelations.

where the indices represent the bin number considered and σ the covariance matrices of the measurement and after propagation of the uncertainty.

Figure 8.3 shows the resulting covariance matrices for the two example cases as a function of the bin number. In one case, the bin width was chosen slightly smaller than the resolution of about 0.055, in the other case it is larger. The negative values in the bins next to the diagonal are a result of the smearing: The counts measured in a bin can also originate in an adjacent bin of the true x (or even further away), but the sum is fixed. This causes an anticorrelation in adjacent bins. The effect becomes very large as soon as the bin width decreases to a size similar to the resolution. Comparing the two binnings shows this effect clearly: The case of a binning even slightly smaller than the resolution gives uncertainties three orders of magnitude larger than a binning twice as big.

The resulting unfolded distributions for the example are shown in figure 8.4. The uncertainty for each point is the associated diagonal element of the covariance matrix. The large fluctuations are not the result of any mathematical error but in fact the central values represent the maximum of the posterior (Gaussian) distribution or the minimum-variance unbiased estimator (MVUE) in a frequentist prescription [103]. If the whole covariance matrix is considered, no information is lost in going to the smaller binning. The unfolding procedure can be reversed, by multiplying with the response again, reproducing the original measurement and a fully diagonal covariance matrix. In fact, the smaller binning contains slightly more information.

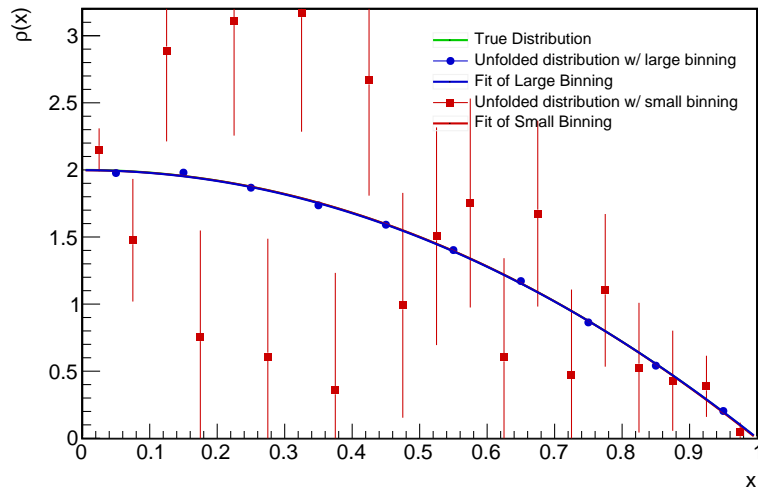


Figure 8.4: Unfolded results from the two binnings with fits. A change from a binning larger than the resolution to one slightly smaller changes the uncertainties for individual points significantly. A comparison to a model taking into account the correlations however still yields the same result. As a result, all fits lie on top of each other.

This information is recovered when comparing to models. A fit of a second-order polynomial to the unfolded distribution, taking into account the full covariance matrix, yields the same result for both cases. The procedure is described in more detail in the appendix B.4. In this case, the true distribution is easily recovered as shown in figure 8.4. However, the result also means that models which differ on the scale of the p_T -resolution cannot easily be distinguished using this measurement. This is true for any binning.

For practical reasons however, it is very useful to consider this effect when choosing a binning: Firstly, many comparisons to theory are done by eye, comparing the models to the size of the statistical and systematic uncertainties. In this case, the large uncertainties make the case using the smaller bins seem like a much worse measurement. Secondly, it is usually assumed that statistical uncertainties are uncorrelated between p_T -bins, which is still approximately true if the binning is sufficiently larger than the resolution.

If additional knowledge about the true distribution of the measured variable is available, it can be incorporated into the prior. In this case, the central points for the unfolding are not the result of a matrix inversion. It is useful to note that for a flat prior the matrix inversion is equivalent to a maximization of the posterior probability (The covariance then follows from the Hessian matrix). Assuming Gaussian measurement uncertainties, this is also called χ^2 -unfolding. If the prior is a (multidimensional) Gaussian,

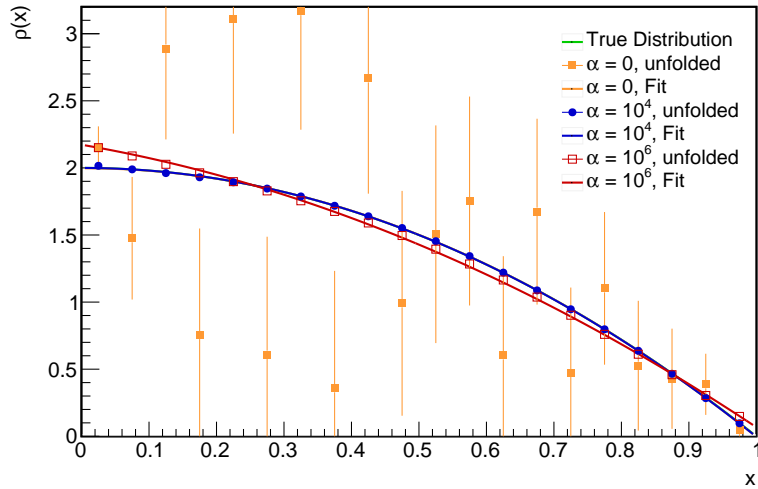


Figure 8.5: Unfolding using Tikhonov regularization. For $\alpha = 0$ (orange), the result is the same as for the matrix inversion. For larger values, the anticorrelations decrease while a bias is introduced. For this smooth example, the bias only becomes apparent at large values of α . All other cases lie on top of each other relative to the line width.

the posterior is as well, so this approach still works (because the χ^2 is proportional to the log-likelihood). For physical distributions, prior information can contain knowledge about the smoothness of the distribution. In most practical applications there is only the abstract notion that the resulting distribution ought to be smooth, but if there were a physical constraint on the difference of two adjacent bins, the resulting prior would be

$$-2\log(P(\vec{x}_{\text{true}})) = \frac{1}{\sigma_{\text{smoothness}}^2} \sum_{i=1}^{n_{\text{bins}}-1} ((x_{\text{true}})_i - (x_{\text{true}})_{i+1})^2, \quad (8.6)$$

written here as the expression of the additive constant of the χ^2 function. If there were prior knowledge about the smoothness of the slope instead, the term would be

$$-2\log(P(\vec{x}_{\text{true}})) = \frac{1}{\sigma_{\text{smoothness}}^2} \sum_{i=1}^{n_{\text{bins}}-2} ((x_{\text{true}})_i - 2(x_{\text{true}})_{i+1} + (x_{\text{true}})_{i+2})^2. \quad (8.7)$$

The assumption of such a term is called *Tikhonov Regularization* ([104] as cited by [103]). The width of the prior is then a free parameter. For brevity, it is often written as $\alpha = 1/\sigma_{\text{smoothness}}^2$, the *regularization parameter*. This approach can also be motivated by searching for points in the parameter space, where the result is smoothest while not decreasing the likelihood too much [103].

Fundamentally, a regularization procedure is a form of smoothing of the resulting distribution. The addition of prior terms that are not quantitatively based on actual,

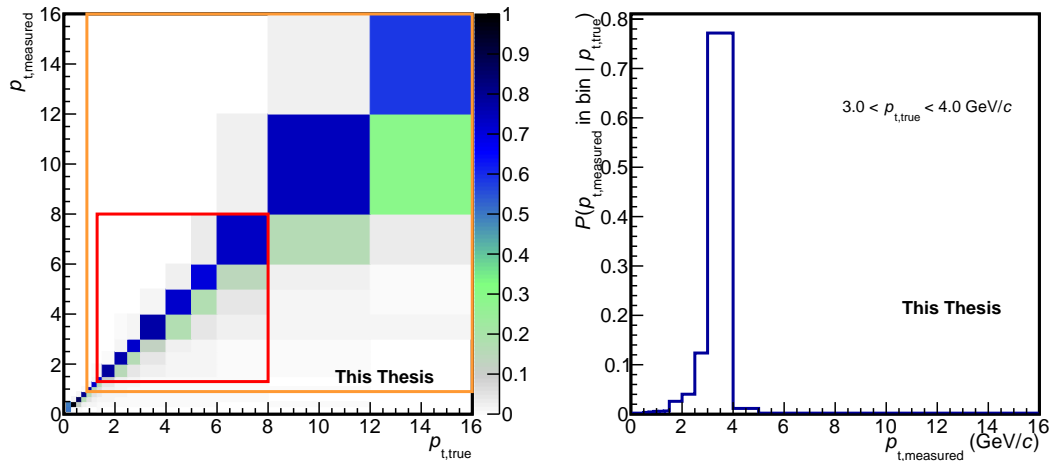


Figure 8.6: Response matrix of the electron p_T (left) together with a the probability distribution of the measured p_T for a fixed true p_T (right). The red box shows the part of the diagram corresponding to the bins of the result, while the orange box signifies the bins considered for the unfolding procedure.

available information will introduce a bias. Other regularization procedures exist [105–107] but have the same drawback. Figure 8.5 shows the effect of applying additional terms. For large values of α in the second-order Tikhonov regularization of equation 8.7 the function tends towards a straight line locally. The bias will thus be larger if the true distribution has more small-scale features. As the true distribution is not generally known, it is also very difficult to estimate the bias due to the regularization. Thus, regularization should be avoided when comparing to models.

8.2 Application to the analysis

For the binning chosen for this analysis, the bin width is much larger than the resolution of the transverse momentum. The response matrix in figure 8.6 shows that the off-diagonal elements are small. This means that there are no problems from the effects described previously. The response matrix was estimated from the signal-enhanced Monte Carlo simulations. The large statistics mean that the statistical uncertainty on the response is small. There are two main reasons for the asymmetric shape of the response matrix: Due to the falling electron spectrum, more electrons are at the lower edge of a bin than at the upper edge. That is why it is more likely for electrons to be measured in the next lower bin than in the next higher one in p_T . Additionally, electrons are affected

by bremsstrahlung: Due to interactions with the detector material they may lose a significant fraction of their energy. In this case they are measured at a lower transverse momentum than they had at the moment of their production.

Another difference of the unfolding in the analysis compared to the example is the finite p_T -range of the measurement. As discussed in the previous chapters ([link](#)) the signal extraction is done only for the p_T -range 1.3 – 8 GeV/c. The example shows, that the unfolded result is also connected to the non-measured bins via the off-diagonal elements of the response matrix. In summary: unfolding the measured bins requires knowledge about the bins where no measurement was performed.

This problem is alleviated somewhat by the fact that the response is dominated by the diagonal elements. As a result, the unfolded value in a bin depends mostly on the measured value, slightly on the values in the adjacent bins and very little on the bins further away. Nevertheless, it would be problematic to just assume zero entries in all non-measured bins. Instead, the bins should be filled with the best guess for the value and the uncertainty of this guess should be propagated to the final unfolded result. An assumption of this kind was made for the two next lower and higher bins at the edges of the measured range. For the immediately adjacent bins, the signal extraction was done in the same way as it is done for the bins in the measured range. This gives reasonable estimates for the central points. The uncertainty estimation might not be accurate (which is why the bins are not part of the measurement range) but the error of the uncertainty becomes very small when it is propagated to the measurement range. For the bins adjacent to these, an assumption is made, while bins further out are not considered. The response matrix for the unfolding only contains these (12) bins.

This is important when considering the normalization of the response. In the definition of equation 8.1, the response is a probability distribution and should thus have an integral of unity. It is however possible to include the case that a particle is not reconstructed at all. In that case, e.g. the reconstruction efficiency can be contained in the response. For this analysis, the track selection efficiencies are handled separately. Nevertheless, the case for the measured value to fall outside the measured range should be included. This means, that in the response matrix the measured bins for one $p_{T,true}$ -bin have a sum smaller than unity.

Figure 8.7 shows the covariance matrix (and correlation matrix) resulting from the matrix inversion. The correlations between adjacent bins are very small, making an interpretation as independent statistical uncertainties reasonable. Thus the correlations of the resulting statistical uncertainties will be not be considered further.

While it is simple to propagate the statistical uncertainties through the unfolding

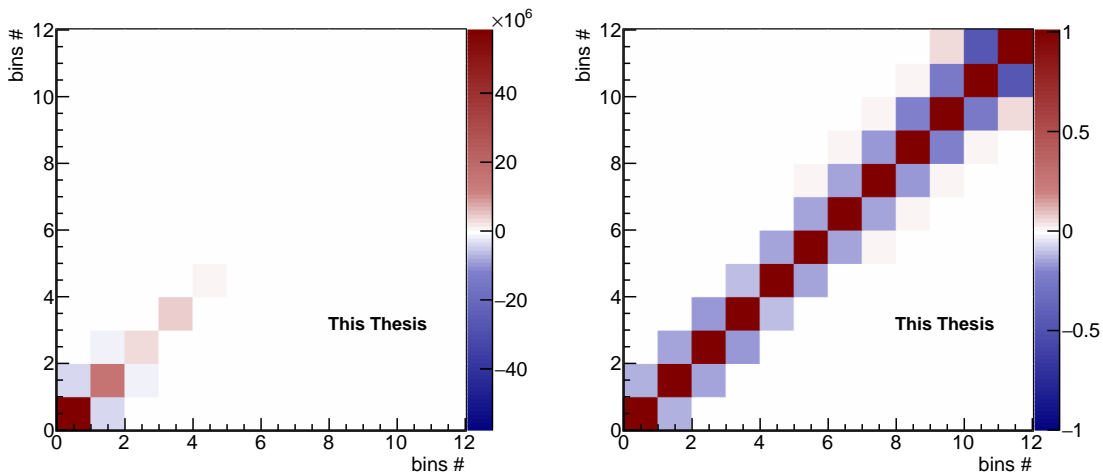


Figure 8.7: Covariance matrix for the analysis for all bins considered in the unfolding. The entries vary over several orders of magnitude. For a clearer picture of the correlations, the correlation matrix has been plotted as well. The off-diagonal elements are small.

process, this is not the case for the systematic uncertainties. The reason is that their (initial) correlation matrix is not known. To simplify this problem, the following approximation is made: The most important elements in the response matrix apart from the diagonal elements are the ones just next to them. This corresponds to the reasonable intuition that the measured p_T will usually still be close to the true value. As a result, only correlations of adjacent bins are important. The effect giving rise to systematic uncertainties typically vary smoothly with p_T . This means that the systematics should be strongly correlated between adjacent p_T -bins, with the relative uncertainty being similar. If all relative uncertainties were correlated and of the same size, then this could be expressed as an uncertainty on a constant prefactor of the data vector, which propagates trivially through all calculations. Any deviation from this case will be primarily propagated by the diagonal elements. Thus, it is a reasonable approximation to assume that the relative systematic uncertainties before and after the unfolding are the same.

Figure 8.8 shows the change of the central values and the uncertainties before and after the unfolding. While the central values increase by about 15%, the uncertainties increase by about twice this amount. This difference represents the loss of information due to the uncertainty of the transverse momentum measurement. The unfolding algorithm itself does not introduce a bias and thus does not give a contribution to the systematic uncertainty. The assumptions about the adjacent bins however do have an uncertainty. The most important contribution comes from the uncertainty of the bins

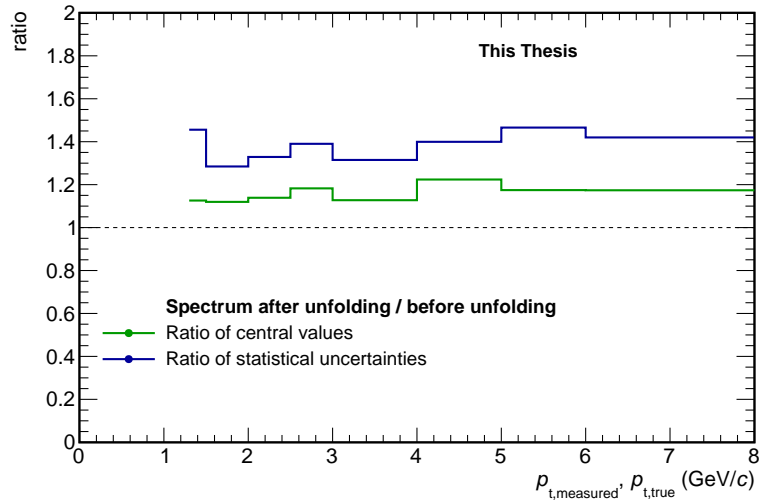


Figure 8.8: Ratio of the p_T distributions before and after unfolding as well as the ratio of the uncertainties.

that are directly adjacent to the measurement range, contributing a few percent. However, for these the uncertainties are taken into account automatically via the unfolding. This means that part of the statistical uncertainty in the first and last bin of the measurement range comes from the statistical uncertainty of the signal extraction in these adjacent bins. Given that this is actually the result of statistical fluctuations, the contribution is not separated further. In these bins, the determination of the systematic uncertainty is not very accurate, due to e.g. the proton contamination at low p_T , which is not treated explicitly. However, the this uncertainty of the uncertainty does not have a large influence when propagated to the measurement range due to the small off-diagonal elements of the response matrix. The bins adjacent to this (two bins away from the measurement range) have an even larger uncertainty, as there is no measurement at all. To get a general impression of the influence of these bins, the assumed values were varied significantly: Given that the p_T -density will typically fall over the measured range the cases were compared, where the density stays the same and where it falls by a factor of four from one bin to the next. The results show that this changes the unfolded result in the adjacent bins by the order of 10% but has no significant influence to the measured range.

This means that by the unfolding procedure described in this chapter, all contributions to the uncertainty due to the transverse momentum resolution are automatically incorporated in the statistical uncertainties associated with the result.

Chapter 9

Results

After the p_T -unfolding procedure and the correction with the track selection efficiency, the result is divided by a factor of 2 to obtain the average of electrons and positrons from heavy-flavor hadron decays. The resulting p_T -differential yield is shown in figure 9.1. The resulting uncertainties are dominated by the systematic effects. To quantify the final state effects, it is useful to compare to the case of proton-proton collisions at the same center of mass energy and calculate the R_{AA} (given by eq. 3.2). The following section will give a brief overview of the approach used to estimate the proton-proton reference. The details may be found in [5].

9.1 The pp reference

The proton-proton reference for this analysis comes from [5]. It was obtained with a similar method as the one discussed in this work. The basic idea is to combine an estimate of the background electrons with the requirement of a minimum impact parameter. Measurements exist both for $\sqrt{s} = 7$ TeV [5] and for $\sqrt{s} = 2.76$ TeV [6]. These cover the whole p_T -range. As shown in figure 7.1, it is possible to estimate the non-heavy flavor electron background from separate measurements by ALICE. This background can be subtracted from the total measured electron yield to obtain the contribution from the heavy-flavor decays. Using measurements of the charm hadrons [101, 108], it is possible to also obtain an estimate of the charm contribution to the electrons. Subtracting this as well yields the blue points shown in figure 9.2 (left). These have large uncertainties, particularly at low transverse momentum. By requiring a minimum impact parameter for the electron candidates, the contribution from beauty-hadron decay electrons is increased relative to the other electron sources. The p_T -distribution of the electrons after applying this requirement is shown in figure 9.2 (right) together with the

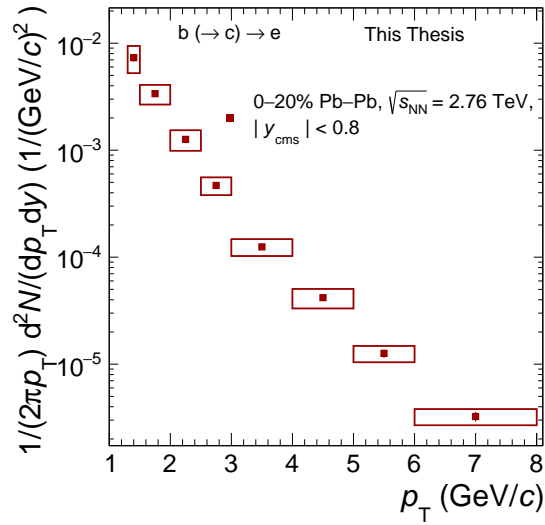


Figure 9.1: Invariant yield of electrons from beauty-hadron decays in Pb-Pb collisions with the centrality class 0 – 20%.

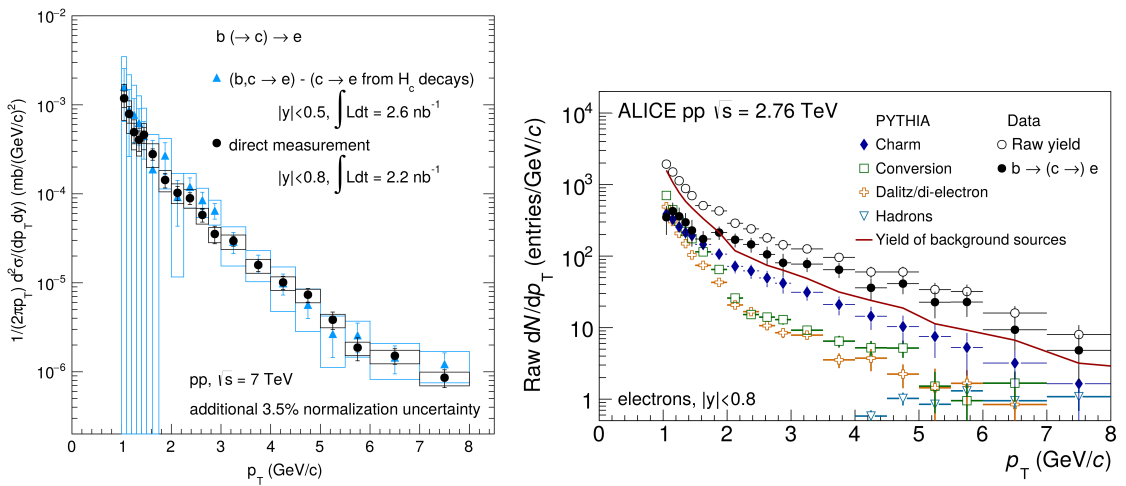


Figure 9.2: Analysis method for the pp reference. After subtracting the estimated background, only the contribution from electrons from beauty-hadron decays remains, but with large uncertainties. By requiring a minimum impact parameter, the background decreases (*right*), leading to a measurement with smaller uncertainties (*left*). (publication in preparation [45])

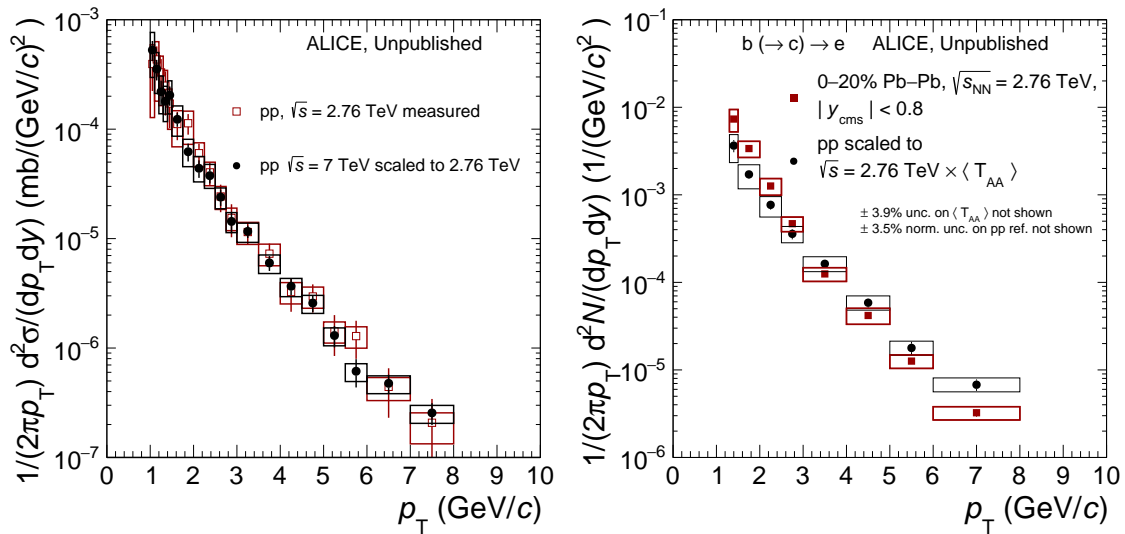


Figure 9.3: *Left:* Comparison of measurements at $\sqrt{s_{NN}} = 2.76$ TeV and 7 TeV scaled by FONLL. *Left:* Comparison of scaled and rebinned result to Pb–Pb measurement. (publication in preparation [46])

estimates for the background electrons. Subtraction of the remaining background and correction for the efficiency yields a measurement with significantly smaller uncertainties as shown by the black markers in 9.2 (left). As for the Pb–Pb analysis presented in this work, the information about the impact parameter distributions was obtained based on the Monte Carlo simulations, which require a correction. By weighting the electrons from the different sources according to the p_T of the mother particle, both the corrections for the selection efficiency and the information about the strength of the different sources were applied in one step.

The measurements in pp and $Pb-Pb$ can be compared by scaling the cross-sections according to theoretical predictions of their center-of-mass energy dependence. Figure 9.3 (left) shows a comparison at $\sqrt{s_{NN}} = 2.76$ TeV. The scaling was done using FONLL pQCD calculations [109–111]. The results are consistent within uncertainties. Both the systematic and statistical uncertainties are lower for the measurement at 7 TeV even considering the additional uncertainties from the scaling. These were estimated using variations of the renormalization and factorization scales as well as the beauty-quark mass. A large correlation in the systematic uncertainties at both energies can be expected. Thus, there is no advantage in combining the results as the uncertainties would have to be added linearly. Thus, the scaled result at 7 TeV was chosen as the reference for the R_{AA} calculation. A comparison of the pp reference scaled with the average nuclear overlap (discussed in section 2.2.1) is shown in figure 9.3 (right). Already in

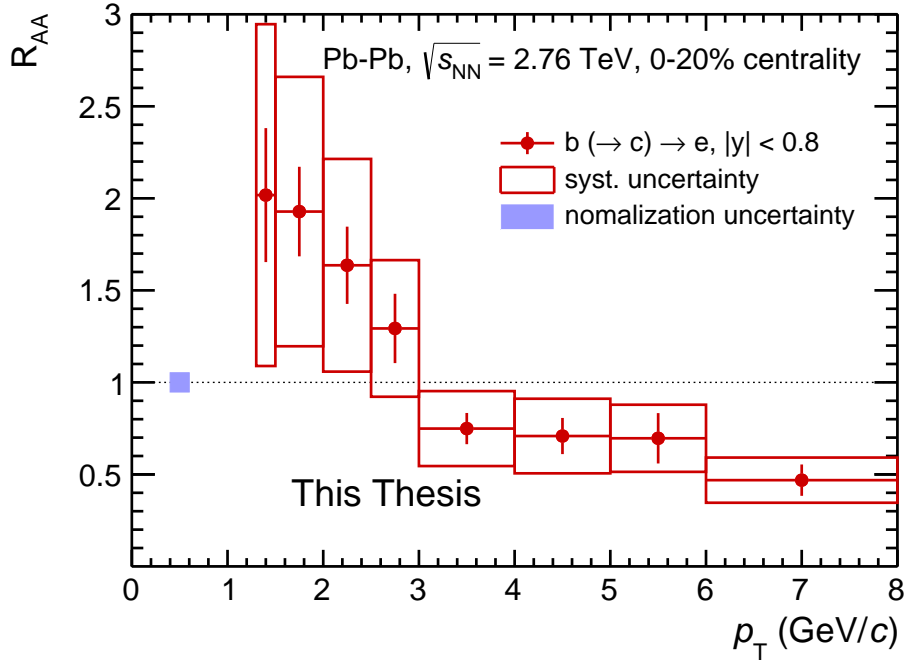


Figure 9.4: Nuclear modification factor of beauty-hadron decay electrons in Pb–Pb collisions with 0 – 20% centrality.

this plot some difference between the distributions is visible although both have sizable uncertainties.

9.2 The nuclear modification factor

The R_{AA} is the ratio of the distributions in figure 9.3 (right). The form

$$R_{AA} = \frac{dN_{AA}/dp_T}{\langle T_{AA} \rangle d\sigma_{pp}/dp_T}, \quad (9.1)$$

was already motivated in chapter 3. For the combined uncertainties, a linear uncertainty propagation was used. This assumes that the relative uncertainties for the $1/(d\sigma_{pp}/dp_T)$ term are approximately the same as for $d\sigma_{pp}/dp_T$ itself. As a result, the statistical uncertainties - which are known to be independent - are added in quadrature. The correlation is not known exactly for the systematic uncertainties. As described in the previous chapter, the pp reference was measured with a method that is also based on the impact parameter. As a result, some uncertainties should appear in a similar way in both analyses, which causes some degree of correlation between the resulting systematic uncertainties. On the other hand, some properties of the description of the simulations

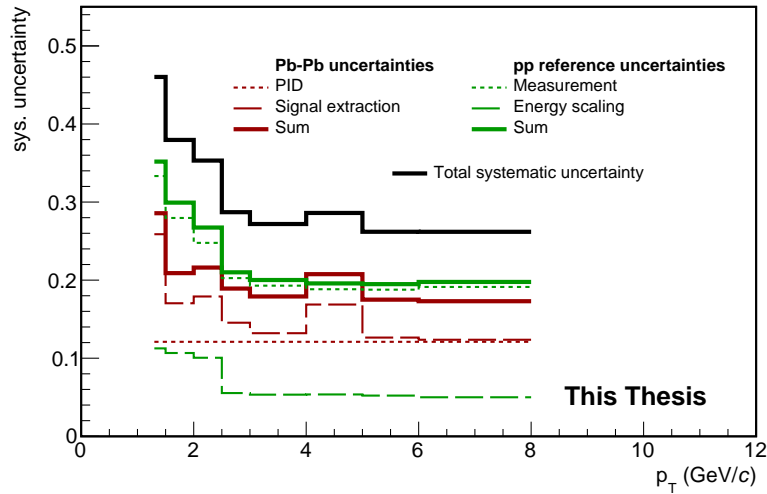


Figure 9.5: Contributions to the systematic uncertainties of the nuclear modification factor. These were summed in quadrature.

might change from pp to Pb–Pb and the methods are not the same. As a result, the exact strength of the correlation is not known. In general, there are three limiting cases: The samples can be (fully) correlated, (fully) anticorrelated or uncorrelated. If they are correlated, the systematics cancel out in the ratio, if they are anticorrelated, they should be added linearly and if they are uncorrelated, the correct procedure is to take the quadratic sum like for the statistical uncertainties. From the reasoning above, the reasonable expectation is a positive correlation: The systematic uncertainties are partially correlated with an unknown positive correlation coefficient. The correct procedure for the propagation is thus between subtraction and a quadratic sum. In the absence of further knowledge, the choice was to use the quadratic sum, which represents the worst-case of no correlation.

Figure 9.5 shows the different contributions to the systematic uncertainties of the nuclear modification factor. In particular at low transverse momenta the main contribution comes from the pp reference. Both the PID and the signal extraction uncertainties contribute significantly to the Pb–Pb portion of the systematics over the whole p_T -range of the measurement. Apart from the leftmost p_T -bin, the systematic uncertainty stays fairly constant at a value of about 20%. This means that a significant improvement of the R_{AA} measurement requires an improved pp measurement.

Figure 9.4 shows the resulting nuclear modification factor. The central values show a decreasing trend with p_T . The uncertainties are typically of the order of 30% and can be

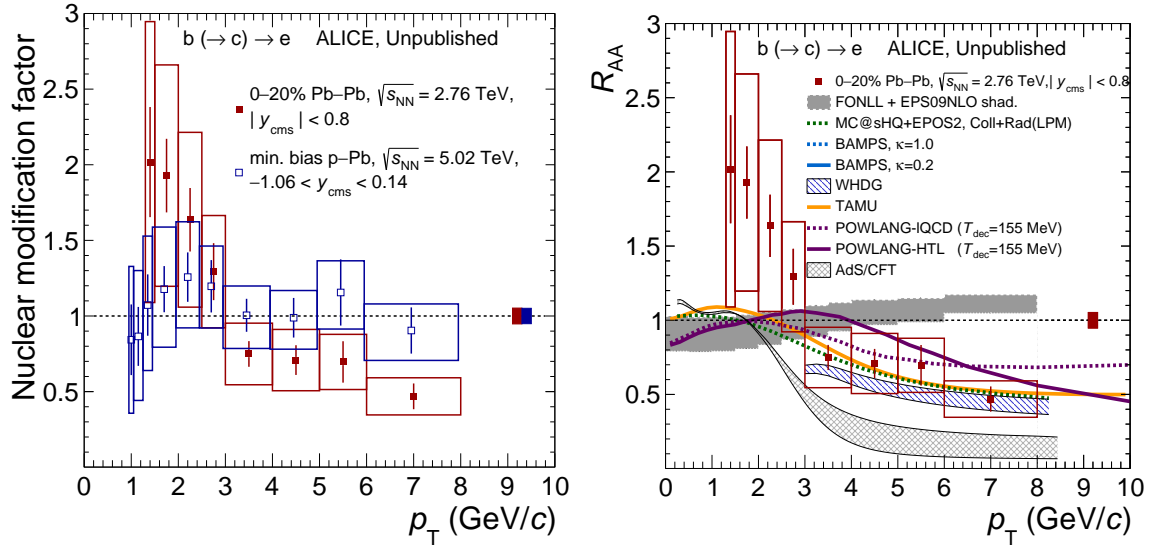


Figure 9.6: Comparison of the nuclear modification factor with the p–Pb result and with theory calculations. (publication in preparation [46])

assumed to be correlated between adjacent p_T -bins. The rightmost bin shows the most significant deviation from unity with about 3.5σ . To assess the effect of the medium, it is useful to compare to the result from p–Pb collisions, which was discussed in chapter 3 (figure 3.3, right). This comparison is shown in figure 9.6 (left). While the p–Pb result is compatible with unity over the whole measurement range, the Pb–Pb result shows a clear trend. The R_{pA} result can give some information about effects that are specific to nuclei but do not require the creation of a QGP. A modification due to the nPDFs would give a different effect in a Pb–Pb collision than in a p–Pb collision, with the effect being about twice as large when both participating nuclei are affected. Nevertheless, the p–Pb result gives further credence to the nPDF calculations, which do not predict a large effect in Pb–Pb due to the initial state. This can be seen in the right plot of figure 9.6. The calculation based on FONLL+EPS09 yields a slightly rising expected R_{AA} , which is the opposite trend of the data. All of this gives further credence to the interpretation that the deviation of the R_{AA} from unity is due to a medium modification.

Several of the theoretical calculations arrive at similar predictions for the R_{AA} , as shown in figure 9.6 (right). These agree well with the data but also with each other. One exception is the prediction of the AdS/CFT-inspired model, which predicts a stronger suppression. Due to the migration in phase-space of the quarks towards lower energies, the R_{AA} rises for all models when going towards lower p_T . Around the lower edge of the measurement, most models show a peak due to the acceleration of low-energy beauty quarks by the expanding medium. The peaks are much closer to unity than the central

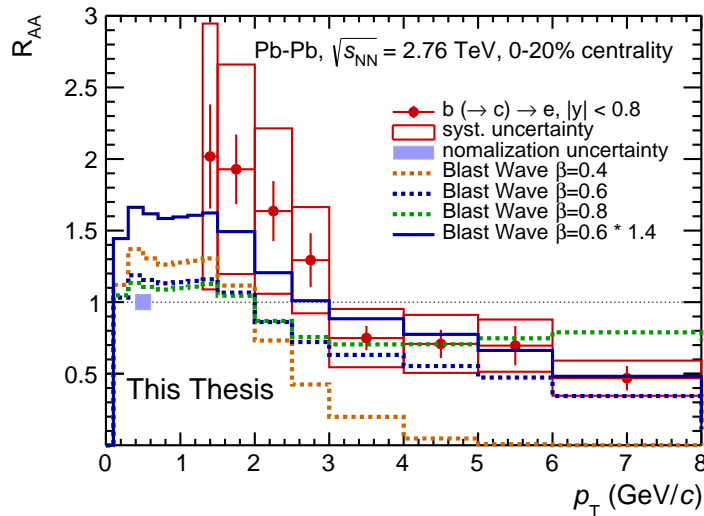


Figure 9.7: Comparison of the measured nuclear modification factor with a blast wave model using different mean transverse velocities β .

points of the measurements but consistent within uncertainties. The rise towards low p_T will be discussed in a bit more detail in the next section. The pQCD based MC@sHQ[64], BAMPS[61, 112], and WHDG[113–115] models as well as the non-perturbative transport model TAMU tend towards the lower edge of the measurement while the POWLANG model result - in particular the calculation based on hard thermal loop resummation - tends towards the upper edge of the uncertainties.

9.3 Comparison to a blast wave model

To gain some intuitive understanding of the result it is useful to compare it to a phenomenological model. The blast wave approach [116] assumes full thermalization of the medium and in particular a thermal distribution of the resulting hadrons. In this picture, all beauty hadron move at the velocity of the local medium at freeze-out. The medium at freeze-out is represented by a 3-dimensional hypersurface. Assuming that the energy distribution within the system of each volume element is given by a Boltzmann-distribution with one common (freeze-out) temperature, the resulting energy distribution can be obtained by boosting all particles to the lab-frame and integrating over the hypersurface. Only radial flow is included in the model. As a result, the transverse velocity profile of the hypersurface is assumed to be dependent only on the radius. The dependence is described by a power law. The model thus has four free parameters: The exponent for

the velocity profile, the mean transverse velocity, the temperature of the medium and the mass of the particle.

The relevant particles for the model are the beauty hadrons. To connect their kinematics to the decay electrons, the Monte Carlo simulations described in section 4.6 were used. For simplicity, the "pp reference" for the calculation of the R_{AA} was simply the output of the enhanced Monte Carlo sample, which is similar to the pp and p-Pb beauty-hadron decay electron measurements. To derive the p_T -distribution of the electrons from that of the beauty hadrons, the correlation shown in figure 5.1 was applied. This gives a slight bias for very low p_T electrons, because only electrons with the basic TPC and ITS signals were considered. However, these do not contribute greatly to the total yield. For the comparison, total beauty conservation was assumed, meaning the pp and Pb-Pb estimate were scaled to have the same normalization. As the model setup, the temperature parameter was set to $kT = 160$ MeV, the particle mass to m_{B_0} and the exponent for the velocity profile to one. The result is particularly sensitive to the mean transverse velocity. Figure 9.7 thus shows the resulting R_{AA} for three different choices of this parameter (β). The theoretical considerations described in chapter 3 suggest that, while low momentum beauty quarks may thermalize, those with very large initial momenta might not. This suggests that the blast-wave model does not apply at very large momenta. The results of the calculation show that the beauty quarks relevant for this measurement might indeed be thermalized, although the description of the hydrodynamics in the blast-wave model is quite crude. The best description is given by the model with $\beta = 0.6$, which is consistent with blast-wave fits of low-mass hadrons [117].

The blast-wave result can also yield some insight into the rise of the measured R_{AA} at low p_T . The additional particles can either come from larger transverse momenta when they lose energy or from lower transverse momenta when they are accelerated by the expanding medium. The largest peak results from the slowest expansion. The shape of the peak does not vary much with the model parameters. In all cases the peak reaches at most values of 1.3 – 1.4 in the R_{AA} . The reason for this becomes apparent from the correlation of the hadron and electron p_T shown in figure 5.1 (left): Hadrons of almost all p_T have a large probability of producing a low p_T -electron (0.5 – 1.5 GeV/c). This means that it is difficult to find a beauty hadron R_{AA} , which causes an excess of electrons e.g. in the range 1.3 – 2 GeV/c but not below. As a result, an R_{AA} of 1.5 or even 2 is not consistent with beauty conservation within the measured (effective) pseudorapidity range. If this condition is loosened, the model with $\beta = 0.6$ describes the data very well assuming an increase in the total yield by a factor of 1.4.

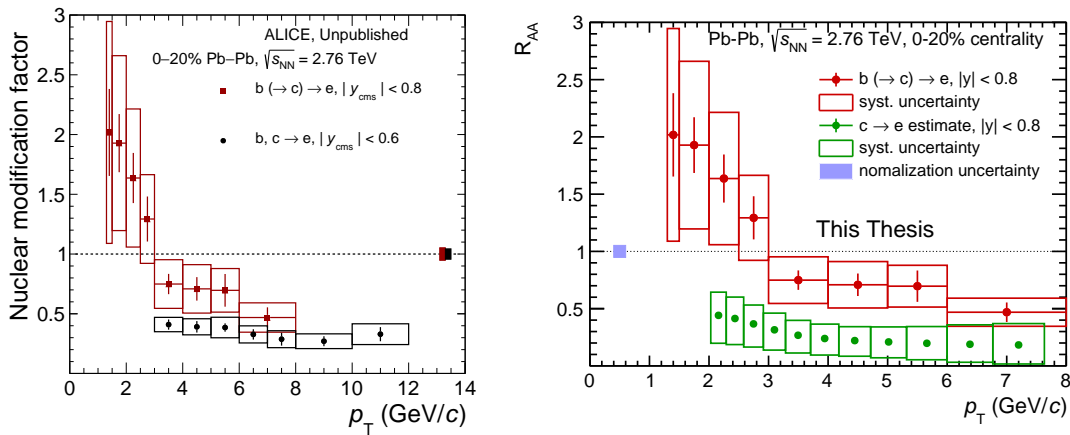


Figure 9.8: *Left*: Comparison to a measurement of the combined heavy-flavor decay electron measurement [118] (publication in preparation). *Right*: Comparison to an estimate of the charm electron R_{AA} based on the D^0 measurement [69, 119].

9.4 Comparison to the charm case

From the measurement of the nuclear modification factor of D mesons [69] it is possible to extract an estimate for the R_{AA} of charm electrons by applying the correlation of the mother particle transverse momentum with that of the daughter electron similar to the approach used for the blast wave calculation [119]. Here, this was done using electrons from D^0 decays. In a similar manner, the result can be compared to the combined electrons from beauty and charm sources [118]. The results are shown in figure 9.8. Both show lower values of the R_{AA} than the beauty-hadron decay electrons. The interpretation is not as straightforward as for the beauty case, because the different charm hadron species differ more strongly in the branching ratios to electrons than the beauty hadrons meaning that e.g. charm conservation does not imply conservation of the electrons from charm hadron decays. It is important to also consider the dependence of the R_{AA} on the slope of the spectrum as well as the quark energy loss. Due to the generally stronger slope of the p_T -distribution of electrons from charm-hadron decays, a slightly lower R_{AA} would be expected even for the same migration in the phase space of the electrons. Nevertheless, the results show some indication of a dependence of the R_{AA} on the (heavy) quark flavor. A more quantitative understanding can be achieved via the comparison to theoretical calculations as discussed previously.

Chapter 10

Summary and Outlook

In this work, the first measurement of the beauty production in central Pb–Pb collisions at low p_T and at mid-rapidity was presented. The measurement was done via the decay electrons of the resulting beauty-hadrons using template fits of the impact parameter distribution. Both the finite statistics of the data and the Monte Carlo simulations are considered in this approach. A clear difference is visible in the comparison of the appropriately scaled proton-proton measurement to the Pb–Pb result, which points clearly to an in-medium modification of the beauty-quark momentum distribution, given that no such effect is seen in p–Pb. Due to the fact that the measurement is based on templates of the impact parameter distributions from Monte Carlo simulations, the reproduction of several key features by the simulations was assessed.

Both the uncertainties associated with the simulations and with the particle identification contribute to the sizeable uncertainties in both the pp and the Pb–Pb measurement. Improving these uncertainties would yield additional separation power with respect to the different theoretical calculations.

The particle identification can profit significantly from the addition of the Transition Radiation Detector. The advantage is twofold: Slight additional reduction of the deuterons and protons should be sufficient to decrease the reliance on the TOF, which gives the largest uncertainty due to the representation in the detector simulations. In addition, a stronger separation of electrons from pions - a main purpose of the TRD - allows for weaker TPC PID selection criteria, which in turn decreases the associated uncertainty. The completion of the TRD in 2015 [120] results in full azimuthal acceptance of this detector making this a viable option for further study in particular for the new larger center-of-mass energy of $\sqrt{s_{NN}} = 5.02$ TeV [121].

The uncertainties of the signal extraction can broadly be separated into uncertainties due to the Monte Carlo simulations and uncertainties intrinsic to the maximum likelihood

(or posterior) method. For the latter, improvements come both from including more prior information and from extraction more information from the posterior probability distribution. An important piece of prior information is the knowledge that the templates should be smooth at some scale. This cannot be easily included by smoothing the templates because of the resulting biases of the fits. However, it is part of the prior knowledge, that the distributions (except for the electrons from photon conversions) should have a single peak and then fall off towards the tails of the distribution. This monotonous behavior can easily be included in a prior, which does however become non-differentiable. Markov Chain Monte Carlo methods allow for the use of such priors, also eliminating the need for the bias correction. Studies [96] have shown that these methods can be applied using a larger impact parameter bin width (which decreases the dimensionality of the problem). Further optimization of the proposal functions may lead to reasonably quick convergence even for larger dimensionalities.

The uncertainty of the measurement can also be decreased by using templates based on higher statistics. In practice, large effective statistics could be achieved for the templates by separating the production of the electrons (the event generator and decayer) from the detector response. This factorization can be achieved for heavy-flavour hadron decay electrons because the detector response is almost completely independent of the production mechanism. The templates would then in practice result from a convolution of the distributions of the true impact parameter with the detector response. This approach is more difficult for the Dalitz and conversion electrons. The true impact parameter distribution of the Dalitz electrons approaches a δ -distribution relative to the resolution. For the conversion electrons, the mismatched conversion electrons have a different detector response compared to the rest. With sufficient statistics in the templates, the fluctuations can be neglected (or approximated in a χ^2 approach [91]), leading to a likelihood with only four unknown parameters. In such a case, it is possible to also consider the p_T -distribution of the beauty-hadrons as a set of unknown parameters of the fit procedure. The template distribution for the electrons from beauty-hadron decays now depends on the p_T -distribution of the hadrons. As a result, all p_T -bins are connected, because the likelihood does not factorize anymore. To analyze the resulting common posterior distribution, Markov chain Monte Carlo methods can once more be useful. This is the approach of the measurement by the PHENIX collaboration [72] discussed in section 3.6. In principle, this approach results in an immediate measurement of the beauty hadron p_T -distribution. A difficulty is the wide distribution of the p_T of the daughter electrons for a given hadron p_T , as shown in figure 5.1. From the examples given in chapter 8, it is clear that the uncertainties of the electron measurement lead

to even larger uncertainties in the p_T -distribution of the beauty hadrons, which in turn lead to uncertainties in the impact parameter distributions. Thus, such an approach has to rely on some degree of regularization (chapter 8) in order to give reasonable results. This addition of ad-hoc penalty terms to the likelihood/posterior distribution leads to systematic uncertainties that are difficult to estimate.

The method used to measure the pp reference in ALICE [5, 45] is based on the subtraction of the background electron sources estimated from other measurements, the so-called cocktail. This information could also be applied as a prior in the method presented here, which still allows for a calculation by maximizing the posterior. This would in effect combine the information used in both methods. Given that the uncertainty a low p_T is largely due to the uncertainty in the reference (shown in figure 9.5), both the measurement of the R_{AA} and R_{pA} can profit from an improved reference.

The analysis method for beauty-hadron decay electrons introduced in this work makes use of the full impact parameter distribution for the separation of the electron sources. The estimates of the different contributions to the uncertainty are largely data-driven, which produces reliable estimates. As a result, the method can easily also be applied to different data sets. These include not only the recently measured data in Pb–Pb collisions at $\sqrt{s_{NN}} = 5.02$ TeV, but also the more peripheral collisions at 2.76 TeV.

A particularly interesting measurement is also the v_2 of electrons from beauty-hadron decays. The elliptic flow v_2 was introduced in section 2.2.3 as a coefficient of the Fourier-decomposition of the azimuthal angular distribution of the particles. In the case of a statistical separation as in the analysis presented here, this coefficient can be estimated by comparing the yields within an azimuthal angle of $\pi/4$ of the event plane ('in-plane') and outside of this ('out-of-plane') (e.g. [122]). Within the calculation, the yields appear as ratios. As a result, it profits greatly from the expected strong correlation of the uncertainties, which cancel out in the ratio. For this reason, the estimation of this correlation is highly beneficial. It can be achieved by comparing the ratio plots (e.g. figure 7.14) for both cases as well as the toy model results (figure 7.10). The complementary information from the v_2 yields an additional understanding of the interaction of beauty quarks with the hot and dense medium.

The rise of the R_{AA} going from the value of 0.4-0.5 at the high p_T edge of the measurement range towards lower p_T gives an insight into the interactions of the beauty quarks with the medium. In this range both radiative and elastic processes may contribute. The shape of the R_{AA} points towards a strong interaction with the medium, being qualitatively compatible with a blast-wave fit assuming full thermalization. Using the methods developed in this work based on the use of template fits of the impact

parameter distribution this can be further quantified both by applying the method to additional data samples and by making use of the fact that the approach can make use of any additional prior information and is thus easily generalizable. This suggests, that the measurement of beauty-hadron decay electrons will remain an important approach to the measurement of beauty in heavy-ion collisions at least until direct reconstruction of the hadronic decays of beauty hadrons will become possible [87] at low p_T and at mid-rapidity after the proposed upgrade of the ALICE experiment for the LHC Run 3.

Appendix A

Abbreviations and terms

This addendum serves as an overview of the abbreviations and terms introduced in the text. Here, a short explanation is given, together with the page number, where the term was first introduced in this text for reference.

BAMPS (page 27). The Boltzmann approach to MultiParton Scatterings, a pQCD-based model for the heavy-quark energy loss and the surrounding medium.

beauty-hadron decay electrons (page 39). Electrons from the decays of hadrons with beauty valence quarks (usually B mesons).

conversion electrons (page 68). Electrons produced in the conversion of photons in the detector material ($\gamma \rightarrow e^+e^-$).

Dalitz electrons (page 71). Electrons that are neither conversion electrons nor come from heavy flavor hadron decays. These mostly originate from the decays of light mesons.

impact parameter (page 43) Distance of closest approach of the reconstructed track to the reconstructed interaction vertex in the transverse plane. Can be positive or negative depending on whether the interaction vertex is inside or outside of the circle of the projected track.

ITS (page 33). Inner Tracking System. 6 layers of silicon-based detectors near the interaction point.

MC@sHQ (page 27). pQCD-based model of the heavy-quark energy loss.

minimum bias Monte Carlo sample (page 37). Monte Carlo simulations meant to reproduce typical collisions.

mismatched conversion electrons (page 87). Conversion electrons produced outside the active area of the first layer of the ITS, randomly associated with signals of other particles to still pass the selection criteria.

Monte Carlo simulations (page 37). Set of simulated events, combining particle production, decays and detector interactions.

PID cluster (page 34). Integrated charge corresponding to one row in the radial segmentation of the TPC suitable for use in the particle identification.

POWLANG (page 27). Model of the heavy-quark energy loss using lattice QCD calculations as input.

proxy sample (page 49). A sample of particles with similar properties as the one of interest with regard to a specific comparison.

p_T -bin (page 41). Subrange of the measurement p_T -range that is considered separately in the analysis.

signal-enhanced Monte Carlo sample (page 37). Monte Carlo simulations with added signals to increase the statistics for heavy-flavor decay electrons.

statistical uncertainty (page 81). The uncertainty of the signal extraction due to statistical fluctuations in both the data and the Monte Carlo templates.

TAMU (page 27). Model of the heavy-quark energy loss using lattice QCD potentials as input.

template (page 71). The distribution of the impact parameter of electrons from a particular source as taken from a Monte Carlo simulation.

TOF (page 36). Time-Of-Flight detector. Provides PID information based on the arrival time of particles.

toy model (page 78). The virtual repetition of the experiment to analyze the statistical uncertainty and bias of the parameter estimate.

TPC (page 34). Time Projection Chamber. Large cylindrical gas detector used for tracking and PID.

Tracking cluster (page 34). Integrated charge corresponding to one row in the radial segmentation of the TPC suitable for tracking.

TRD (page 35). Transition Radiation Detector. 6 detector layers based on a combination of energy loss in the gas and the production of transition radiation.

V0 detectors (page 32). Two scintillator arrays used e.g. in the determination of the centrality.

V0 electrons (page 50). A sample of electrons selected by searching for decay electrons from photon conversions.

V0 pions (page 50). A sample of charged pions selected by searching for the decays of K_S^0 .

WHDG (page 27). pQCD-based model of the heavy-quark energy loss.

Appendix B

Calculations

B.1 A simple model for the effect of the truncated mean

This model was originally derived in [91]. Here, a slightly quicker derivation is presented. The model aims at a description of the truncated mean used for the calculation of the ALICE TPC signal. However, it can be applied more generally to truncated means of detector signals with similar properties. One assumption of the model is that there is a fixed number of clusters, each with the same underlying probability distribution for the signal.

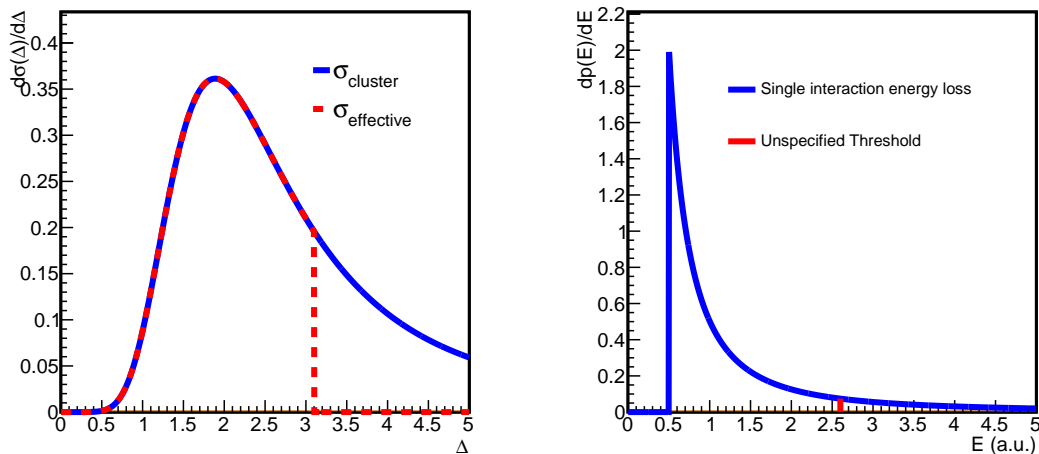


Figure B.1: Explanatory sketches for the truncated mean model. *Left:* Energy loss and effective energy loss distribution for the track length associated to one cluster. *Right:* Energy loss distribution of a single interaction of the charged particle with the gas.

For the calculation, Δ represents the energy loss, $\sigma_{cluster}(\Delta)$ represents the probability distribution of the energy loss within one cluster. Without the truncated mean, the total energy loss is the sum of the signal in the individual clusters and its probability distribution is given by a convolution of all clusters:

$$\sigma_{tot} = \sigma_{cluster} \otimes \sigma_{cluster} \dots \quad (B.1)$$

For the truncated mean, the sum only includes the lowest 60% of signals. For a large number of clusters this means that only signals in the lowest 60% of the pdf are included. This means, that the truncated signal is equal to a convolution of an effective pdf which is zero for energy loss values above some threshold. The comparison of the true and effective energy loss distribution is sketched in figure B.1. This means, that e.g. the truncated mean of 100 clusters is approximated by the 60-fold convolution of the effective energy loss distribution. This can be written as the 60-fold convolution of the associated Landau-distributions and a correction factor. A convolution of Landau distributions yields again a Landau. For this reason, it is useful to write the result as the product of this Landau and a correction function:

$$S_{TPC} = L(\Delta)f(\Delta) , \quad (B.2)$$

where L is the Landau distribution and f is the correction, which can be large. It is useful to interpret the correction factor with regards to the convolutions: For each value of the total energy loss Δ , there is a contribution from each cluster. The correction factor is the ratio of the combinations that only contain contributions below the cut-off to all possible combinations. To approximate this factor, it is useful to remember the origin of the Landau-distribution, which is based on the Rutherford-cross section [80] of the individual interactions of the charged particle with the detector gas. The energy loss distribution is sketched in figure B.1 (right). Most of the individual interactions deposit only a small amount of energy while some deposit a lot. The model assumption is that these large energy deposits from a single interactions can push the energy loss in the cluster that contains them over the cut off. In a further simplification, this can be stated thusly: Each individual interaction with a large energy loss has a fixed and independent probability of creating a cluster above the threshold. Due to the fact that these interaction are rare, their number is Poisson-distributed. For a probability of $q = (1 - p)$ for one such interaction to create a cluster above the threshold and $\hat{\lambda} = \hat{\lambda}(\Delta)$ the mean number of such interactions along the entire track, the correction function can

be written as

$$f(\Delta) = \sum_{n=0}^{\infty} \frac{\hat{\lambda}^n \exp(-\hat{\lambda})}{n!} p^n = \exp(-q\hat{\lambda}) . \quad (\text{B.3})$$

A Taylor expansion of $\hat{\lambda}$ to first order in Δ yields a constant term that does not contribute and a linear term, which can be combined with the constant q , resulting in

$$f(\Delta) \sim \exp(-\lambda\Delta) , \quad (\text{B.4})$$

with a positive fit variable λ .

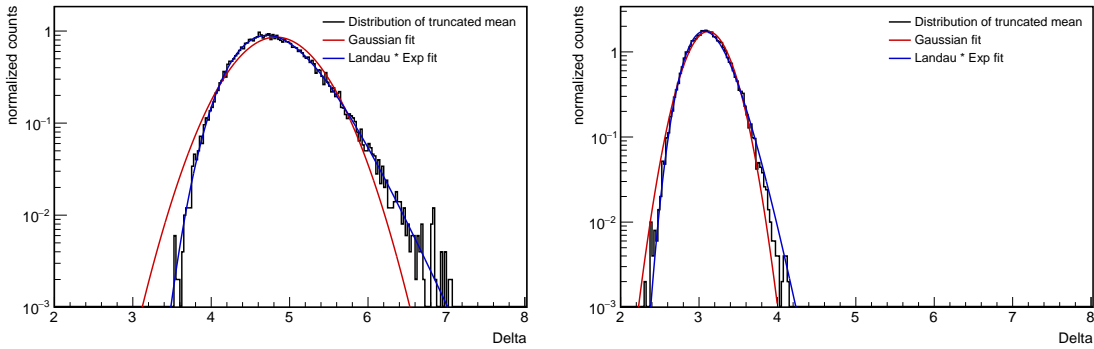


Figure B.2: The truncated mean model for a truncated mean of Landau distributions with 10% (*Left*) and 40% (*Right*) of the original 100 clusters removed.

To assess the accuracy of the model, it can be directly compared to a truncated mean of Landau distributed clusters. Figure B.2 shows the results using 100 clusters. The result shows that the model works better for weaker truncations, while for a stronger truncation the peak is well reproduced but the tail overestimated.

B.2 Geometrical factor for electrons from photon conversions

The cylindrical geometry of the detector means that the material budget of particles from the interaction vertex to a certain distance from the beam-pipe depends on the polar angle (or the pseudorapidity). Particles emitted at larger $|\eta|$ experience a larger material budget. The track length of a particle with some η will compare to the length of a particle perpendicular to the beam-pipe as $|p|$ does to p_T . To connect this to the pseudorapidity, it is useful to consider

$$\frac{p_L}{|p|} = \tanh(\eta) , \quad (\text{B.5})$$

from which follows

$$\frac{|p|}{p_T} = \frac{1}{\sqrt{1 - \left(\frac{p_L}{|p|}\right)^2}} = \frac{1}{\sqrt{1 - \tanh^2(\eta)}} = \cosh(\eta), \quad (\text{B.6})$$

which is the required geometric factor. If the η distribution of photons and light particles is equal, then the η distribution of the electrons from photon conversion is modified by this factor.

B.3 Radial dependence of the mean impact parameter for electrons from photon conversions

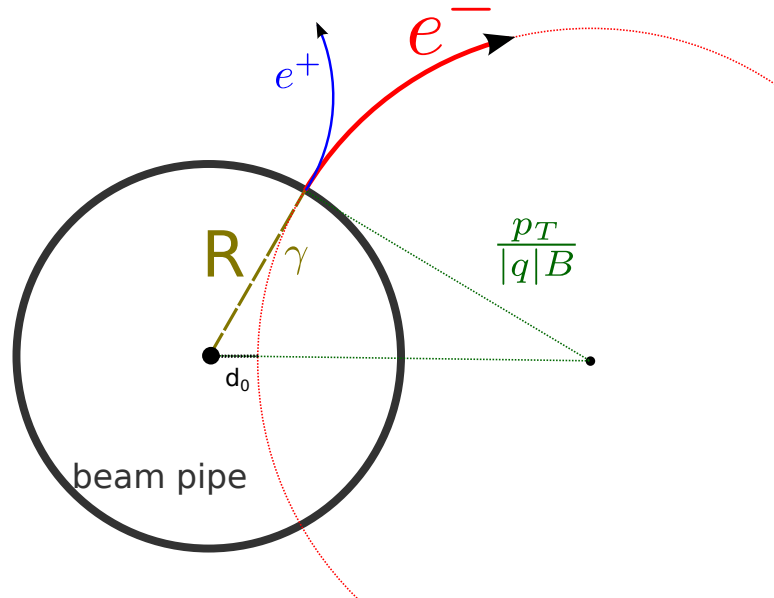


Figure B.3: Sketch of the production of conversion electrons in the detector material. This is the same figure as 7.3, repeated for convenience.

The electrons resulting from photon conversions in the detector material initially have a momentum vector almost parallel to the momentum of the photon. The average opening angle is of the order of $m_e c^2 / E_e$ [95]. This fraction is so small for the energies considered in this work, that it will be neglected. Figure B.3 shows a sketch of the

process. In transverse plane, the shape of the tracks of charged particles is a circle with radius

$$r = \frac{p_T}{|q|B}, \quad (\text{B.7})$$

where q is the charge of the particle and B is the magnetic field. As sketched in the figure, the expected impact parameter (without resolution effects) assuming a production radius R is given by

$$\langle d_0 \rangle = \sqrt{R^2 + r^2} - r = r \left(\sqrt{1 + \frac{R^2}{r^2}} - 1 \right). \quad (\text{B.8})$$

For the energies and production radii discussed here, $R \ll r$, allowing for the approximation

$$\langle d_0 \rangle \approx \frac{R^2 |q| B}{2p_T}, \quad (\text{B.9})$$

using a Taylor expansion.

B.4 The Mahalanobis distance

For a Gaussian probability distribution of a measured parameter x , the probability density for its true value being μ is given by

$$p(\mu) = \frac{1}{\sqrt{2\pi\sigma^2}} e^{-\frac{1}{2}(x-\mu)(\sigma^{-2})(x-\mu)}, \quad (\text{B.10})$$

where σ^{-2} is the inverse variance. If n independent measurements are combined (e.g. measurements in different p_T -bins), the combined probability is given by the product of the individual probabilities:

$$p(\vec{\mu}) = \prod_{i=1}^n p(\mu_i | \sigma_i^{-2}, x_i), \quad (\text{B.11})$$

with x_i the measured points and σ_i^{-2} the associated inverse variance. With the definition

$$\Sigma^{-1} = \begin{pmatrix} \sigma_1^{-2} & & & \\ & \sigma_2^{-2} & & \\ & & \ddots & \\ & & & \sigma_n^{-2} \end{pmatrix} \quad (\text{B.12})$$

this can be written as

$$p(\vec{\mu}) = \frac{1}{\sqrt{(2\pi)^n |\Sigma|}} e^{-\frac{1}{2}(\vec{x}-\vec{\mu})\Sigma^{-1}(\vec{x}-\vec{\mu})}, \quad (\text{B.13})$$

with $|\Sigma|$ the determinant of Σ . Now

$$-2\log p(\vec{\mu}) = \sum_i (x_i - \mu_i)^2 / \sigma_i^2 + c , \quad (\text{B.14})$$

where c is a constant independent of μ . The first term is also known as the χ^2 measure. Its square-root is the Mahalanobis distance [123, 124]. The generalization to the case of correlated uncertainties is now straightforward. The correlated uncertainties correspond to a multivariate Gaussian distribution as in equation B.13. For a given covariance matrix Σ , the inverse Σ^{-1} defines the probability distribution representing this covariance. Then, the generalization to the χ^2 measure can be expressed as

$$D^2(\vec{\mu}, \vec{x}) = (\vec{x} - \vec{\mu})\Sigma^{-1}(\vec{x} - \vec{\mu}) , \quad (\text{B.15})$$

which is the square of the Mahalanobis distance. For a fit of data values with correlated Gaussian uncertainties, minimizing this generalized distance is equivalent to a maximum likelihood fit or the maximum of the posterior probability distribution for flat priors.

Appendix C

Additional material concerning the signal extraction

C.1 Detailed description of the fit algorithm

This section aims to describe the implementation of the algorithm in more detail. The additions concern mostly the starting values for the iterations.

The fit is implemented in the class "AliMCLogLFitter". This class needs a histogram of the data, an array of the template histograms and the number of sources considered as input. Optional input includes the fit range and the source to be considered to have contributed in bins without contributions from Monte Carlo (section 7.2.2).

The initial values for the p_j are set such, that the integral of $p_j A_{ji}$ over the impact parameter yields half the number of counts in the data histogram. The entire fitting procedure is repeated five times for different sizes of the starting steps $p_{j,\text{start}}/10 \cdot n$ for iteration n . The result with the highest likelihood is returned. For each iteration, the p_j are varied and for each proposal, the maximization w.r.t. the A_{ji} is performed using an iterative approach. The approach calls the mnseek-minimizer n times for the approach to the maximum followed by a finer approach using the Migrad algorithm. The iteration algorithm works as in the description given in the text.

Additional functions with coupled p_j may be included. This is used for the uncertainties from strangeness and the baryon ratio. They are treated like the other contributions, except that their parameters are updated for every step according to the distribution they are coupled to.

C.2 Additional figures

Here the fits from all p_T -bins are shown in the figures C.1, C.2 and C.3. The uncertainty estimation diagrams for the p_j are given in figures C.4, C.5 and C.6.

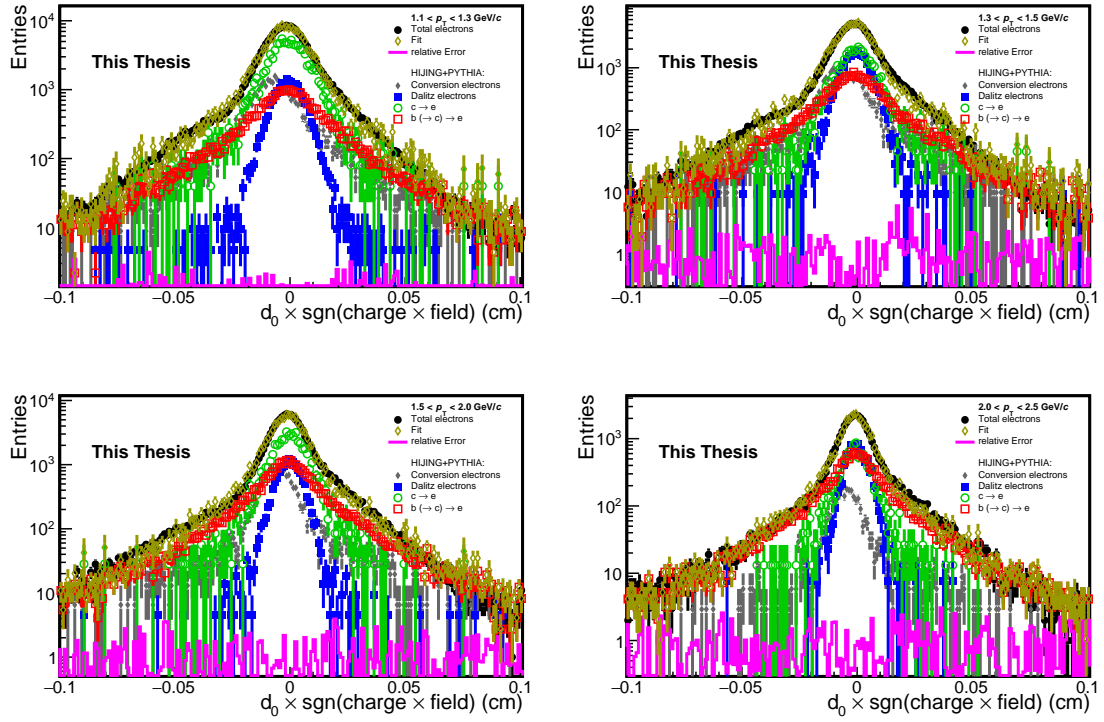


Figure C.1: Fits of the impact parameter distributions (1).

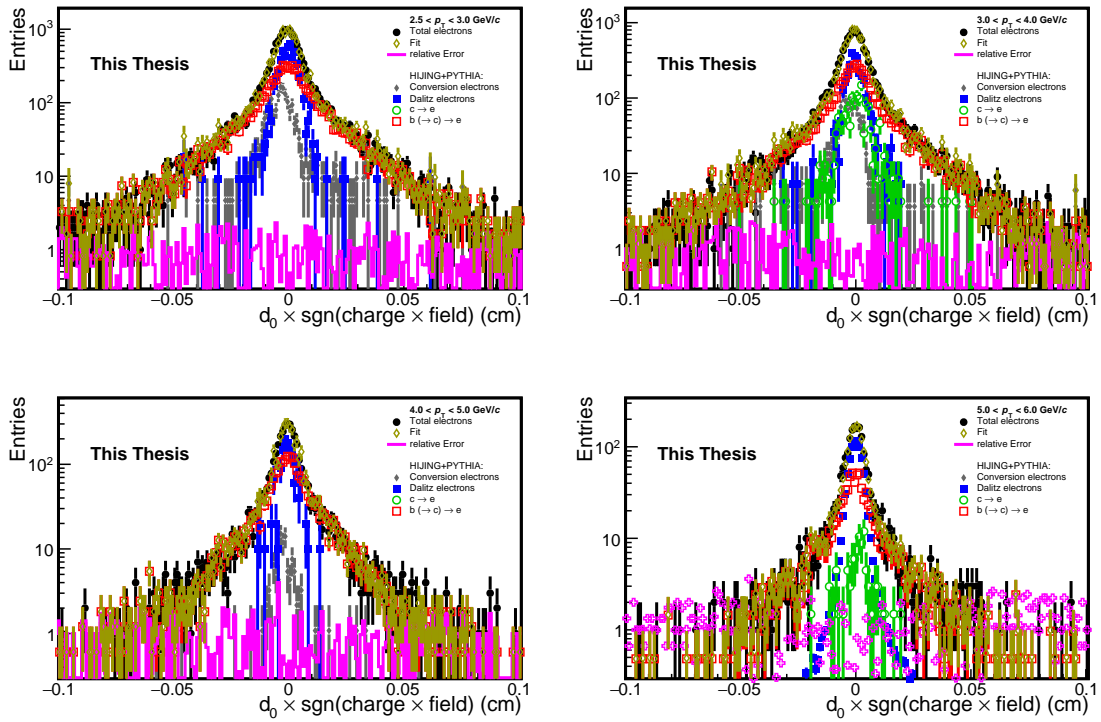


Figure C.2: Fits of the impact parameter distributions (2).

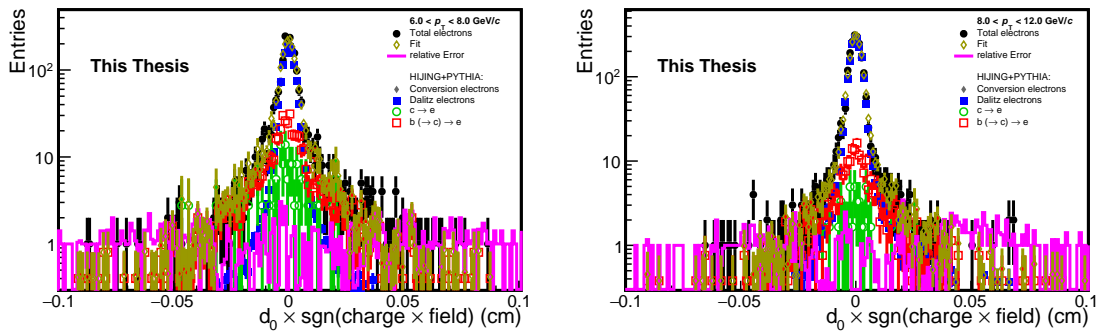


Figure C.3: Fits of the impact parameter distributions (3).

APPENDIX C. ADDITIONAL MATERIAL

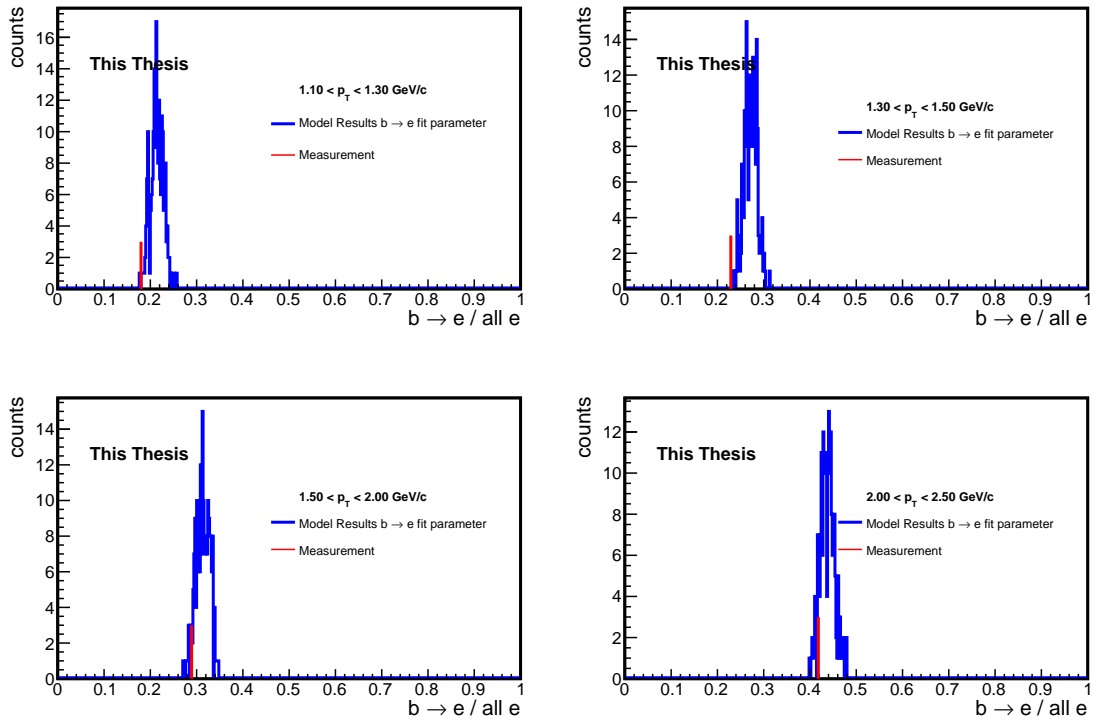


Figure C.4: Uncertainty estimation diagrams (1).

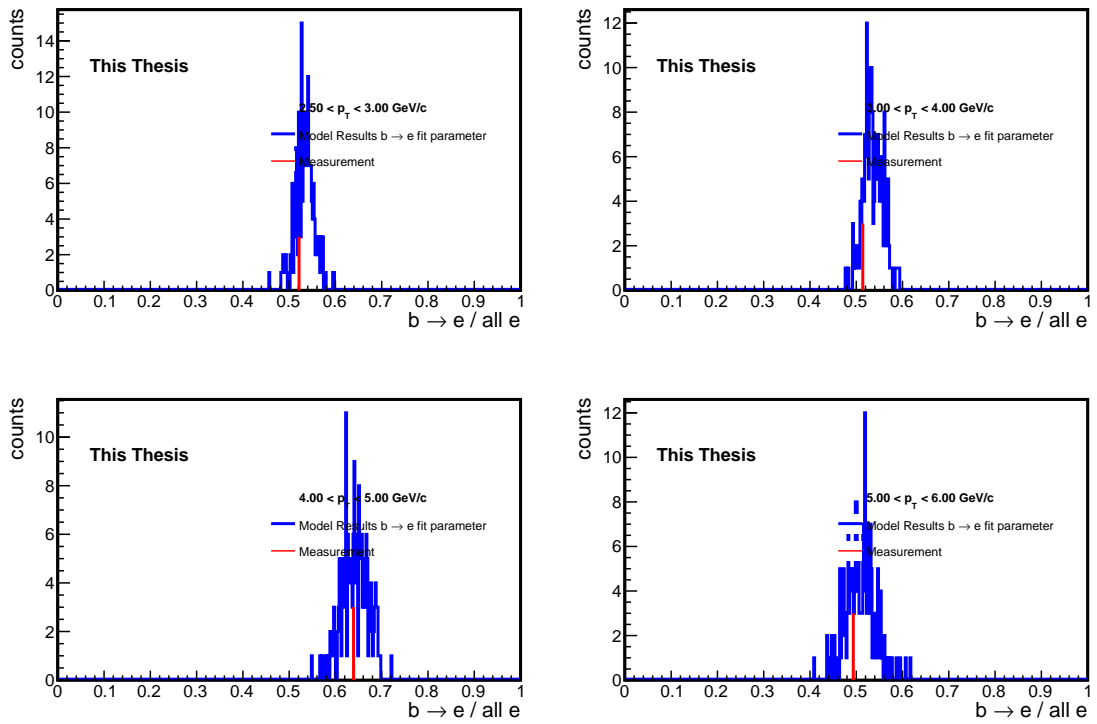


Figure C.5: Uncertainty estimation diagrams (2).

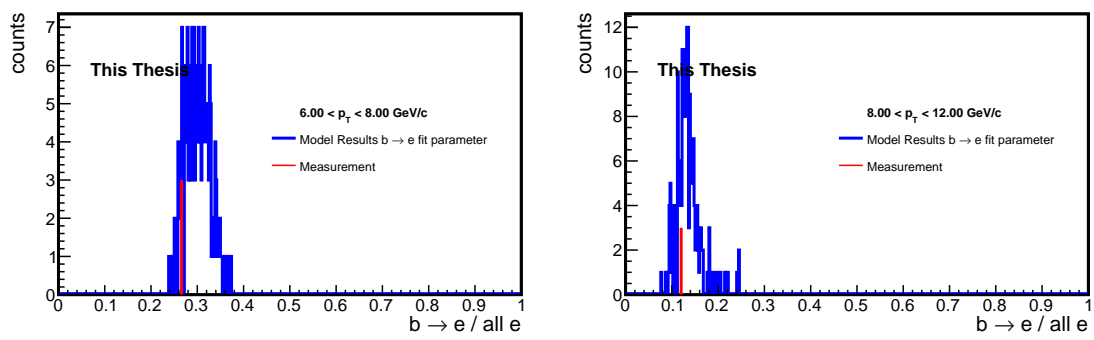


Figure C.6: Uncertainty estimation diagrams (3).

Bibliography

- [1] **NA49** Collaboration, C. Alt *et al.*, “Pion and kaon production in central Pb + Pb collisions at 20-A and 30-A-GeV: Evidence for the onset of deconfinement,” *Phys. Rev.* **C77** (2008) 024903, arXiv:0710.0118 [nucl-ex].
- [2] **NA49** Collaboration, H. Appelshauser *et al.*, “Hadronic expansion dynamics in central Pb + Pb collisions at 158-GeV per nucleon,” *Eur. Phys. J.* **C2** (1998) 661–670, arXiv:hep-ex/9711024 [hep-ex].
- [3] A. Andronic *et al.*, “Heavy-flavour and quarkonium production in the LHC era: from proton–proton to heavy-ion collisions,” *Eur. Phys. J.* **C76** no. 3, (2016) 107, arXiv:1506.03981 [nucl-ex].
- [4] F. Prino and R. Rapp, “Open Heavy Flavor in QCD Matter and in Nuclear Collisions,” arXiv:1603.00529 [nucl-ex].
- [5] **ALICE** Collaboration, B. Abelev *et al.*, “Measurement of electrons from beauty hadron decays in pp collisions at $\sqrt{s} = 7$ TeV,” *Phys. Lett.* **B721** (2013) 13–23, arXiv:1208.1902 [hep-ex].
- [6] **ALICE** Collaboration, B. B. Abelev *et al.*, “Beauty production in pp collisions at $\sqrt{s} = 2.76$ TeV measured via semi-electronic decays,” *Phys. Lett.* **B738** (2014) 97–108, arXiv:1405.4144 [nucl-ex].
- [7] H. Jeffreys, “Probability and scientific method,” *Proceedings of the Royal Society of London. Series A, Containing Papers of a Mathematical and Physical Character* **146** no. 856, (1934) 9–16.
<http://www.jstor.org/stable/2935474>.
- [8] E. T. Jaynes, *Probability theory: The logic of science*. Cambridge university press, 2003.

- [9] R. Barlow, "Systematic errors: Facts and fictions," in *Advanced Statistical Techniques in Particle Physics. Proceedings, Conference, Durham, UK, March 18-22, 2002*, pp. 134–144. 2002. arXiv:hep-ex/0207026 [hep-ex].
<http://www.ippp.dur.ac.uk/Workshops/02/statistics/proceedings/barlow.pdf>.
- [10] M. Schwartz, *Quantum Field Theory and the Standard Model*. Quantum Field Theory and the Standard Model. Cambridge University Press, 2014.
- [11] **Particle Data Group** Collaboration, K. A. Olive *et al.*, "Review of Particle Physics," *Chin. Phys.* **C38** (2014) 090001.
- [12] H. D. Politzer, "Reliable perturbative results for strong interactions?," *Phys. Rev. Lett.* **30** (Jun, 1973) 1346–1349.
- [13] D. J. Gross and F. Wilczek, "Ultraviolet behavior of non-abelian gauge theories," *Phys. Rev. Lett.* **30** (Jun, 1973) 1343–1346.
- [14] P. B. Arnold, "Quark-Gluon Plasmas and Thermalization," *Int. J. Mod. Phys.* **E16** (2007) 2555–2594, arXiv:0708.0812 [hep-ph].
- [15] P. Castorina, K. Redlich, and H. Satz, "The Phase Diagram of Hadronic Matter," *Eur. Phys. J.* **C59** (2009) 67–73, arXiv:0807.4469 [hep-ph].
- [16] E. V. Shuryak, "Theory of hadron plasma," *Sov. Phys.-JETP (Engl. Transl.);(United States)* **47** no. 2, (1978) .
- [17] H.-T. Ding, F. Karsch, and S. Mukherjee, "Thermodynamics of strong-interaction matter from Lattice QCD," *Int. J. Mod. Phys.* **E24** no. 10, (2015) 1530007, arXiv:1504.05274 [hep-lat].
- [18] M. G. Alford and K. Schwenzer, "Probing dense matter in compact star cores with radio pulsar data," *Nucl. Phys.* **A931** (2014) 740–745, arXiv:1408.3152 [nucl-th].
- [19] K. G. Wilson, "Confinement of quarks," *Phys. Rev. D* **10** (Oct, 1974) 2445–2459.
- [20] **HotQCD Collaboration** Collaboration, A. Bazavov *et al.*, "Chiral and deconfinement aspects of the qcd transition," *Phys. Rev. D* **85** (Mar, 2012) 054503.

- [21] Y. Aoki, S. Borsanyi, S. Durr, Z. Fodor, S. D. Katz, S. Krieg, and K. K. Szabo, “The QCD transition temperature: results with physical masses in the continuum limit II.,” *JHEP* **06** (2009) 088, arXiv:0903.4155 [hep-lat].
- [22] S. Borsanyi, Z. Fodor, C. Hoelbling, S. D. Katz, S. Krieg, and K. K. Szabo, “Full result for the QCD equation of state with 2+1 flavors,” *Phys. Lett.* **B730** (2014) 99–104, arXiv:1309.5258 [hep-lat].
- [23] **HotQCD Collaboration** Collaboration, A. Bazavov *et al.*, “Equation of state in $(2+1)$ -flavor qcd,” *Phys. Rev. D* **90** (Nov, 2014) 094503.
- [24] O. DeWolfe, S. S. Gubser, C. Rosen, and D. Teaney, “Heavy ions and string theory,” *Prog. Part. Nucl. Phys.* **75** (2014) 86–132, arXiv:1304.7794 [hep-th].
- [25] J. Maldacena, “The large- n limit of superconformal field theories and supergravity,” *International Journal of Theoretical Physics* **38** no. 4, (1999) 1113–1133.
- [26] J. Casalderrey-Solana, H. Liu, D. Mateos, K. Rajagopal, and U. A. Wiedemann, “Gauge/String Duality, Hot QCD and Heavy Ion Collisions,” arXiv:1101.0618 [hep-th].
- [27] M. L. Miller, K. Reygers, S. J. Sanders, and P. Steinberg, “Glauber modeling in high energy nuclear collisions,” *Ann. Rev. Nucl. Part. Sci.* **57** (2007) 205–243, arXiv:nucl-ex/0701025 [nucl-ex].
- [28] **ALICE** Collaboration, B. Abelev *et al.*, “Centrality determination of Pb-Pb collisions at $\sqrt{s_{NN}} = 2.76$ TeV with ALICE,” *Phys. Rev.* **C88** no. 4, (2013) 044909, arXiv:1301.4361 [nucl-ex].
- [29] L. Keegan, A. Kurkela, P. Romatschke, W. van der Schee, and Y. Zhu, “Weak and strong coupling equilibration in nonabelian gauge theories,” *Journal of High Energy Physics* **2016** no. 4, (2016) 1–27.
- [30] J. Berges, K. Boguslavski, S. Schlichting, and R. Venugopalan, “Universal attractor in a highly occupied non-abelian plasma,” *Phys. Rev. D* **89** (Jun, 2014) 114007.

- [31] J. Berges, K. Boguslavski, S. Schlichting, and R. Venugopalan, “Turbulent thermalization process in heavy-ion collisions at ultrarelativistic energies,” *Phys. Rev. D* **89** (Apr, 2014) 074011.
- [32] A. Kurkela and Y. Zhu, “Isotropization and hydrodynamization in weakly coupled heavy-ion collisions,” *Phys. Rev. Lett.* **115** (Oct, 2015) 182301.
- [33] J.-F. m. c. Paquet, C. Shen, G. S. Denicol, M. Luzum, B. Schenke, S. Jeon, and C. Gale, “Production of photons in relativistic heavy-ion collisions,” *Phys. Rev. C* **93** (Apr, 2016) 044906.
- [34] **ALICE** Collaboration, K. Aamodt *et al.*, “Two-pion bose–einstein correlations in central pb–pb collisions at,” *Physics Letters B* **696** no. 4, (2011) 328 – 337.
- [35] **ALICE** Collaboration, B. B. Abelev *et al.*, “Production of charged pions, kaons and protons at large transverse momenta in pp and Pb–Pb collisions at $\sqrt{s_{NN}} = 2.76$ TeV,” *Phys. Lett.* **B736** (2014) 196–207, arXiv:1401.1250 [nucl-ex].
- [36] C. Gale, S. Jeon, and B. Schenke, “Hydrodynamic Modeling of Heavy-Ion Collisions,” *Int. J. Mod. Phys.* **A28** (2013) 1340011, arXiv:1301.5893 [nucl-th].
- [37] W. Israel and J. Stewart, “Transient relativistic thermodynamics and kinetic theory,” *Annals of Physics* **118** no. 2, (1979) 341 – 372.
- [38] **ALICE** Collaboration, B. B. Abelev *et al.*, “Elliptic flow of identified hadrons in Pb-Pb collisions at $\sqrt{s_{NN}} = 2.76$ TeV,” *JHEP* **06** (2015) 190, arXiv:1405.4632 [nucl-ex].
- [39] A. M. Poskanzer and S. A. Voloshin, “Methods for analyzing anisotropic flow in relativistic nuclear collisions,” *Phys. Rev. C* **58** (Sep, 1998) 1671–1678.
- [40] P. K. Kovtun, D. T. Son, and A. O. Starinets, “Viscosity in strongly interacting quantum field theories from black hole physics,” *Phys. Rev. Lett.* **94** (Mar, 2005) 111601.
- [41] J. Stachel, A. Andronic, P. Braun-Munzinger, and K. Redlich, “Confronting lhc data with the statistical hadronization model,” *Journal of Physics: Conference Series* **509** no. 1, (2014) 012019.

- [42] P. Braun-Munzinger, K. Redlich, and J. Stachel, "Particle production in heavy ion collisions," arXiv:nucl-th/0304013 [nucl-th].
- [43] **CMS** Collaboration, S. Chatrchyan *et al.*, "Study of Z production in PbPb and pp collisions at $\sqrt{s_{NN}} = 2.76$ TeV in the dimuon and dielectron decay channels," *JHEP* **03** (2015) 022, arXiv:1410.4825 [nucl-ex].
- [44] K. J. Eskola, H. Paukkunen, and C. A. Salgado, "EPS09: A New Generation of NLO and LO Nuclear Parton Distribution Functions," *JHEP* **04** (2009) 065, arXiv:0902.4154 [hep-ph].
- [45] **ALICE** Collaboration, J. Adam *et al.*, "Corrigendum to "Measurement of electrons from beauty hadron decays in pp collisions at $\sqrt{s} = 7$ TeV" [Physics Letters B 721 (2013) 13-23] and "Beauty production in pp collisions at $\sqrt{s} = 2.76$ TeV measured via semi-electronic decays" [Physics Letters B 738 (2014) 97-108]," to be submitted.
- [46] **ALICE** Collaboration, J. Adam *et al.*, "Measurement of electrons from beauty-hadron decays in $\sqrt{s_{NN}} = 5.02$ TeV p-Pb and $\sqrt{s_{NN}} = 2.76$ TeV Pb-Pb collisions at the LHC," to be submitted.
- [47] W. Beenakker, W. L. van Neerven, R. Meng, G. A. Schuler, and J. Smith, "QCD corrections to heavy quark production in hadron hadron collisions," *Nucl. Phys.* **B351** (1991) 507–560.
- [48] Z.-B. Kang, I. Vitev, E. Wang, H. Xing, and C. Zhang, "Multiple scattering effects on heavy meson production in p+A collisions at backward rapidity," *Phys. Lett.* **B740** (2015) 23–29, arXiv:1409.2494 [hep-ph].
- [49] F.-M. Liu and S.-X. Liu, "Quark-gluon plasma formation time and direct photons from heavy ion collisions," *Phys. Rev.* **C89** no. 3, (2014) 034906, arXiv:1212.6587 [nucl-th].
- [50] C. Andrés, N. Armesto, C. A. Salgado, and Y. Zhu, "Modelling jet quenching with quenching weights," *Journal of Physics: Conference Series* **612** no. 1, (2015) 012001.
- [51] N. Armesto, M. Cacciari, T. Hirano, J. L. Nagle, and C. A. Salgado, "Constraint fitting of experimental data with a jet quenching model embedded in a hydrodynamical bulk medium," *J. Phys.* **G37** (2010) 025104, arXiv:0907.0667 [hep-ph].

- [52] J. J. Friess, S. S. Gubser, G. Michalogiorgakis, and S. S. Pufu, "Stress tensor of a quark moving through $\mathcal{N} = 4$ thermal plasma," *Phys. Rev. D* **75** (May, 2007) 106003.
- [53] M. Djordjevic and M. Djordjevic, "Generalization of radiative jet energy loss to non-zero magnetic mass," *Phys. Lett.* **B709** (2012) 229–233, arXiv:1105.4359 [nucl-th].
- [54] M. Djordjevic, "Theoretical formalism of radiative jet energy loss in a finite size dynamical QCD medium," *Phys. Rev.* **C80** (2009) 064909, arXiv:0903.4591 [nucl-th].
- [55] M. Djordjevic, "Collisional energy loss in a finite size QCD matter," *Phys. Rev.* **C74** (2006) 064907, arXiv:nucl-th/0603066 [nucl-th].
- [56] A. Andronic *et al.*, "Heavy-flavour and quarkonium production in the LHC era: from proton–proton to heavy-ion collisions," *Eur. Phys. J.* **C76** no. 3, (2016) 107, arXiv:1506.03981 [nucl-ex].
- [57] W. M. Alberico, A. Beraudo, A. De Pace, A. Molinari, M. Monteno, M. Nardi, and F. Prino, "Heavy-flavour spectra in high energy nucleus-nucleus collisions," *Eur. Phys. J.* **C71** (2011) 1666, arXiv:1101.6008 [hep-ph].
- [58] Y. L. Dokshitzer and D. E. Kharzeev, "Heavy quark colorimetry of QCD matter," *Phys. Lett.* **B519** (2001) 199–206, arXiv:hep-ph/0106202 [hep-ph].
- [59] L. D. Landau and I. Pomeranchuk, "Limits of applicability of the theory of bremsstrahlung electrons and pair production at high-energies," *Dokl. Akad. Nauk Ser. Fiz.* **92** (1953) 535–536.
- [60] A. B. Migdal, "Bremsstrahlung and pair production in condensed media at high energies," *Phys. Rev.* **103** (Sep, 1956) 1811–1820.
- [61] J. Uphoff, O. Fochler, Z. Xu, and C. Greiner, "Elastic and radiative heavy quark interactions in ultra-relativistic heavy-ion collisions," *J. Phys.* **G42** no. 11, (2015) 115106, arXiv:1408.2964 [hep-ph].
- [62] C. Peterson, D. Schlatter, I. Schmitt, and P. M. Zerwas, "Scaling violations in inclusive e^+e^- annihilation spectra," *Phys. Rev. D* **27** (Jan, 1983) 105–111.

- [63] J. Uphoff, O. Fochler, Z. Xu, and C. Greiner, “Elliptic Flow and Energy Loss of Heavy Quarks in Ultra-Relativistic heavy Ion Collisions,” *Phys. Rev.* **C84** (2011) 024908, arXiv:1104.2295 [hep-ph].
- [64] M. Nahrgang, J. Aichelin, P. B. Gossiaux, and K. Werner, “Influence of hadronic bound states above T_c on heavy-quark observables in Pb + Pb collisions at the CERN Large Hadron Collider,” *Phys. Rev.* **C89** no. 1, (2014) 014905, arXiv:1305.6544 [hep-ph].
- [65] W. A. Horowitz, “Heavy Quark Production and Energy Loss,” *Nucl. Phys.* **A904-905** (2013) 186c–193c, arXiv:1210.8330 [nucl-th].
- [66] M. He, R. J. Fries, and R. Rapp, “Heavy Flavor at the Large Hadron Collider in a Strong Coupling Approach,” *Phys. Lett.* **B735** (2014) 445–450, arXiv:1401.3817 [nucl-th].
- [67] W. M. Alberico, A. Beraudo, A. De Pace, A. Molinari, M. Monteno, M. Nardi, F. Prino, and M. Sitta, “Heavy flavors in AA collisions: production, transport and final spectra,” *Eur. Phys. J.* **C73** (2013) 2481, arXiv:1305.7421 [hep-ph].
- [68] **ALICE** Collaboration, J. Adam *et al.*, “Transverse momentum dependence of D-meson production in Pb-Pb collisions at $\sqrt{s_{NN}} = 2.76$ TeV,” *JHEP* **03** (2016) 081, arXiv:1509.06888 [nucl-ex].
- [69] **ALICE** Collaboration, B. Abelev *et al.*, “Suppression of high transverse momentum D mesons in central Pb-Pb collisions at $\sqrt{s_{NN}} = 2.76$ TeV,” *JHEP* **09** (2012) 112, arXiv:1203.2160 [nucl-ex].
- [70] **ALICE** Collaboration, J. Adam *et al.*, “Inclusive, prompt and non-prompt J/ψ production at mid-rapidity in Pb-Pb collisions at $\sqrt{s_{NN}} = 2.76$ TeV,” *JHEP* **07** (2015) 051, arXiv:1504.07151 [nucl-ex].
- [71] **CMS** Collaboration, S. Chatrchyan *et al.*, “Evidence of b-Jet Quenching in PbPb Collisions at $\sqrt{s_{NN}} = 2.76$ TeV,” *Phys. Rev. Lett.* **113** no. 13, (2014) 132301, arXiv:1312.4198 [nucl-ex]. [Erratum: *Phys. Rev. Lett.* 115, no. 2, 029903 (2015)].
- [72] A. Adare *et al.*, “Single electron yields from semileptonic charm and bottom hadron decays in Au+Au collisions at $\sqrt{s_{NN}} = 200$ GeV,” arXiv:1509.04662 [nucl-ex].

- [73] **ALICE** Collaboration, B. B. Abelev *et al.*, “Performance of the ALICE Experiment at the CERN LHC,” *Int. J. Mod. Phys. A* **29** (2014) 1430044, arXiv:1402.4476 [nucl-ex].
- [74] R. Frühwirth, “Application of kalman filtering to track and vertex fitting,” *Nuclear Instruments and Methods in Physics Research Section A: Accelerators, Spectrometers, Detectors and Associated Equipment* **262** no. 2, (1987) 444 – 450.
- [75] **ALICE** Collaboration, P. Cortese *et al.*, “ALICE technical design report on forward detectors: FMD, T0 and V0,” . CERN-LHCC-2004-025.
- [76] **ALICE** Collaboration, G. Dellacasa *et al.*, “ALICE technical design report of the inner tracking system (ITS),” .
- [77] **ALICE** Collaboration, K. Aamodt *et al.*, “The ALICE experiment at the CERN LHC,” *JINST* **3** (2008) S08002.
- [78] A. L. I. C. Experiment, “Alice tpc-technical design report, december 1999,” tech. rep., ISBN 92-9083-155-3, Geneva, Switzerland.
- [79] A. Kalweit, *Production of light flavor hadrons and anti-nuclei at the LHC*. PhD thesis, Technische Universität Darmstadt, 2012.
- [80] H. Bichsel and R. P. Saxon, “Comparison of calculational methods for straggling in thin absorbers,” *Phys. Rev. A* **11** (Apr, 1975) 1286–1296.
- [81] H. Bichsel, “A method to improve tracking and particle identification in TPCs and silicon detectors,” *Nuclear Instruments and Methods in Physics Research Section A: Accelerators, Spectrometers, Detectors and Associated Equipment* **562** no. 1, (2006) 154 – 197.
- [82] **ALICE** Collaboration, P. Cortese *et al.*, “ALICE: Addendum to the technical design report of the time of flight system (TOF),” . CERN-LHCC-2002-016.
- [83] R. Brun, F. Carminati, and S. Giani, “GEANT Detector Description and Simulation Tool,” .
- [84] M. Gyulassy and X.-N. Wang, “HIJING 1.0: A Monte Carlo program for parton and particle production in high-energy hadronic and nuclear collisions,” *Comput. Phys. Commun.* **83** (1994) 307, arXiv:nucl-th/9502021 [nucl-th].

- [85] T. Sjostrand, S. Mrenna, and P. Z. Skands, "PYTHIA 6.4 Physics and Manual," *JHEP* **05** (2006) 026, arXiv:hep-ph/0603175 [hep-ph].
- [86] P. Z. Skands, "Tuning Monte Carlo Generators: The Perugia Tunes," *Phys. Rev. D* **82** (2010) 074018, arXiv:1005.3457 [hep-ph].
- [87] J. Stiller, *Full kinematic reconstruction of charged B mesons with the upgraded Inner Tracking System of the ALICE Experiment*. PhD thesis, Universität Heidelberg, 2016.
- [88] **ALICE** Collaboration, B. Abelev *et al.*, "Measurement of electrons from semileptonic heavy-flavour hadron decays in pp collisions at $\sqrt{s} = 7$ TeV," *Phys. Rev. D* **86** (2012) 112007, arXiv:1205.5423 [hep-ex].
- [89] D. Baumeier, "V0 Decays: Documentation of the C++ Program *AliESDv0KineCuts.cxx*." Bachelor thesis, Universität Münster, 2011.
- [90] **ALICE** Collaboration, B. B. Abelev *et al.*, "Transverse momentum dependence of inclusive primary charged-particle production in p-Pb collisions at $\sqrt{s_{NN}} = 5.02$ TeV," *Eur. Phys. J. C* **74** no. 9, (2014) 3054, arXiv:1405.2737 [nucl-ex].
- [91] M. Völkl, "Study of the Transverse Momentum Spectra of Semielectronic Heavy Flavor Decays in pp Collisions at $\sqrt{s} = 7$ TeV and Pb-Pb Collisions at $\sqrt{s_{NN}} = 2.76$ TeV with ALICE," Master's thesis, Universität Heidelberg, 2012.
- [92] M. Braß, "Estimating Hadron Contamination in Pb-Pb Collisions at $\sqrt{s_{NN}} = 2.76$ TeV for Low Transversal Momenta with TPC, TOF and TRD of the ALICE Experiment." Bachelor thesis, Universität Heidelberg, 2014.
- [93] "M. Braß, private communication."
- [94] **ALICE** Collaboration, J. Adam *et al.*, "Direct photon production in pb-pb collisions at," *Physics Letters B* **754** (2016) 235 – 248.
- [95] H. Bethe and W. Heitler, "On the Stopping of fast particles and on the creation of positive electrons," *Proc. Roy. Soc. Lond.* **A146** (1934) 83–112.
- [96] M. Wittner, "Study of the Applicability of Markov Chain Monte Carlo Methods to the Statistical Separation of Electron Sources via the Impact Parameter for ALICE." Bachelor thesis, Universität Heidelberg, 2014.

- [97] Bardenet, Rémi, "Monte carlo methods," *EPJ Web of Conferences* **55** (2013) 02002.
- [98] R. Barlow and C. Beeston, "Fitting using finite monte carlo samples," *Comp. Phys. Comm.* **77** no. 2, (1993) 219.
- [99] F. James and M. Winkler, "Minuit user's guide," June, 2004.
<http://seal.web.cern.ch/seal/documents/minuit/mnusersguide.pdf>.
- [100] M. Kim, "private communication,".
- [101] **ALICE** Collaboration, B. Abelev *et al.*, "Measurement of charm production at central rapidity in proton-proton collisions at $\sqrt{s} = 7$ TeV," *JHEP* **01** (2012) 128, arXiv:1111.1553 [hep-ex].
- [102] Y. Oh, C. M. Ko, S. H. Lee, and S. Yasui, "Ratios of heavy baryons to heavy mesons in relativistic nucleus-nucleus collisions," *Phys. Rev. C* **79** (Apr, 2009) 044905.
- [103] G. Cowan, *Statistical data analysis*. Oxford science publications. Clarendon Press, Oxford, Repr. ed., 2004.
- [104] A. Tikhonov, "On the solution of improperly posed problems and the method of regularization," *Soviet Mathematics* **4** (1963) 1035–1038.
- [105] A. Kondor, "Method of convergent weights — an iterative procedure for solving fredholm's integral equations of the first kind," *Nuclear Instruments and Methods in Physics Research* **216** no. 1, (1983) 177 – 181.
- [106] H. Mülthei and B. Schorr, "On an iterative method for the unfolding of spectra," *Nuclear Instruments and Methods in Physics Research Section A: Accelerators, Spectrometers, Detectors and Associated Equipment* **257** no. 2, (1987) 371 – 377.
- [107] A. Hocker and V. Kartvelishvili, "SVD approach to data unfolding," *Nucl. Instrum. Meth.* **A372** (1996) 469–481, arXiv:hep-ph/9509307 [hep-ph].
- [108] **ALICE** Collaboration, B. Abelev *et al.*, "Measurement of charm production at central rapidity in proton-proton collisions at $\sqrt{s} = 2.76$ TeV," *JHEP* **07** (2012) 191, arXiv:1205.4007 [hep-ex].

- [109] M. Cacciari, M. Greco, and P. Nason, “The $P(T)$ spectrum in heavy flavor hadroproduction,” *JHEP* **05** (1998) 007, arXiv:hep-ph/9803400 [hep-ph].
- [110] M. Cacciari, S. Frixione, and P. Nason, “The $p(T)$ spectrum in heavy flavor photoproduction,” *JHEP* **03** (2001) 006, arXiv:hep-ph/0102134 [hep-ph].
- [111] M. Cacciari, S. Frixione, N. Houdeau, M. L. Mangano, P. Nason, and G. Ridolfi, “Theoretical predictions for charm and bottom production at the LHC,” *JHEP* **10** (2012) 137, arXiv:1205.6344 [hep-ph].
- [112] J. Uphoff, F. Senzel, O. Fochler, C. Wesp, Z. Xu, and C. Greiner, “Elliptic flow and nuclear modification factor in ultrarelativistic heavy-ion collisions within a partonic transport model,” *Phys. Rev. Lett.* **114** no. 11, (2015) 112301, arXiv:1401.1364 [hep-ph].
- [113] W. A. Horowitz and M. Gyulassy, “The Surprising Transparency of the sQGP at LHC,” *Nucl. Phys.* **A872** (2011) 265–285, arXiv:1104.4958 [hep-ph].
- [114] S. Wicks, W. Horowitz, M. Djordjevic, and M. Gyulassy, “Elastic, inelastic, and path length fluctuations in jet tomography,” *Nucl. Phys.* **A784** (2007) 426–442, arXiv:nucl-th/0512076 [nucl-th].
- [115] W. A. Horowitz, “Fluctuating heavy quark energy loss in a strongly coupled quark-gluon plasma,” *Phys. Rev.* **D91** no. 8, (2015) 085019, arXiv:1501.04693 [hep-ph].
- [116] E. Schnedermann, J. Sollfrank, and U. W. Heinz, “Thermal phenomenology of hadrons from 200-A/GeV S+S collisions,” *Phys. Rev.* **C48** (1993) 2462–2475, arXiv:nucl-th/9307020 [nucl-th].
- [117] **ALICE** Collaboration, B. Abelev *et al.*, “Centrality dependence of π , K, p production in Pb-Pb collisions at $\sqrt{s_{NN}} = 2.76$ TeV,” *Phys. Rev.* **C88** (2013) 044910, arXiv:1303.0737 [hep-ex].
- [118] **ALICE** Collaboration, J. Adam *et al.*, “Measurement of the production of high- p_T electrons from heavy-flavour hadron decays in Pb–Pb collisions at $\sqrt{s_{NN}} = 2.76$ TeV,” to be submitted.
- [119] M. Kweon, “private communication,”.
- [120] **ALICE** Collaboration, J. Klein, “The ALICE Transition Radiation Detector: status and perspectives for Run II,” arXiv:1601.00493 [physics.ins-det].

- [121] **ALICE** Collaboration, J. Adam *et al.*, “Centrality dependence of the charged-particle multiplicity density at midrapidity in Pb-Pb collisions at $\sqrt{s_{\text{NN}}} = 5.02$ TeV,” *Phys. Rev. Lett.* **116** no. 22, (2016) 222302, arXiv:1512.06104 [nucl-ex].
- [122] **ALICE** Collaboration, B. B. Abelev *et al.*, “Azimuthal anisotropy of D meson production in Pb-Pb collisions at $\sqrt{s_{\text{NN}}} = 2.76$ TeV,” *Phys. Rev.* **C90** no. 3, (2014) 034904, arXiv:1405.2001 [nucl-ex].
- [123] P. C. Mahalanobis, “On the generalized distance in statistics,” *Proceedings of the National Institute of Sciences (Calcutta)* **2** (1936) 49–55.
- [124] G. Bohm and G. Zech, *Introduction to statistics and data analysis for physicists*. DESY, 2010.

Acknowledgements

I would like to express my gratitude to Prof. Dr. Johanna Stachel for the supervision of this thesis and for the opportunity of working in this exciting field. I want to thank Dr. Yvonne Pachmayer who shared her insights and experience about heavy flavor electrons to make this work possible. I would like to thank Prof. Dr. MinJung Kweon and her students Minjung Kim and Soyeon Cho for the fantastic collaboration on the topics of heavy-flavor measurements.

My thanks also goes to Dr. Michael Winn, for the many fruitful discussions about physics and statistics. I want to also thank Dr. Kai Schweda, Dr. Hans Beck and Dr. Michael Knichel for proof-reading of my thesis and many interesting discussions as well as Prof. Dr. Klaus Reygers who shared his insights about photon conversions and statistics.

I also want to thank Prof. Dr. Ulrich Uwer for his work as second referee of this thesis.

It has been a privilege and a pleasure to be a part of the ALICE community and I want to give thanks to the many members who have influenced this analysis.